GEORGIA DOT RESEARCH PROJECT 18-01

Final Report

DEVELOPMENT OF GDOT ULTRA-HIGH PERFORMANCE CONCRETE FOR BRIDGE DECK CLOSURE POURS

Office of Performance-Based Management and Research
600 West Peachtree Street NW | Atlanta, GA 30308

April 2022

TECHNICAL REPORT DOCUMENTATION PAGE

1. Report No.: FHWA-GA-22-1801	2. Government Accession No.: N/A	3. Recipient's Catalog No.: N/A
4. Title and Subtitle: Development of GDOT Ultra-High Performance Concrete for Bridge Deck Closure Pours		5. Report Date: April 2022
		6. Performing Organization Code: N/A
7. Author(s): Lauren K. Stewart (PI), PhD, PE; Lawrence Kahn (co-PI), PhD, PE; Kimberly Kurtis (co-PI), PhD, PE; Giovanni Loreto, PhD		8. Performing Organization Report No.: 18-01
9. Performing Organization Name and Address: Georgia Tech Research Corporation 926 Dalney Street NW Atlanta, GA 30332-0420 Phone: (404) 385-1919 Email: lauren.stewart@ce.gatech.edu		10. Work Unit No.: N/A
		11. Contract or Grant No.: PI#0015961
12. Sponsoring Agency Name and Address: Georgia Department of Transportation (SPR) Office of Performance-based Management and Research 600 West Peachtree St. NW Atlanta, GA 30308		13. Type of Report and Period Covered: Final; Start April 2018 – End April 2022
		14. Sponsoring Agency Code: N/A

15. Supplementary Notes:
Prepared in cooperation with the US Department of Transportation, Federal Highway Administration.

16. Abstract:
The use of precast prestressed girders with composite precast deck panels along with the use of precast prestressed deck bulb-T girders provide for more economical bridges because of their ability to utilize accelerated bridge construction techniques. The use of concrete deck panels and deck bulb-T systems require the use of closure pours between the units. Ductal™, a proprietary ultra-high performance concrete (UHPC), has been shown to provide an outstanding link between deck segments for closure pours as narrow as 6-in, but Ductal is expensive. This research develops a concrete based on locally available materials (GDOT-UHPC), which has a direct tensile strength greater than 750 psi and ductility and toughness under tensile loads such that the concrete can develop the tensile yield stress of #5 (⅝-in. diameter) reinforcing bars within a 5-in. embedment length. Minimizing the width of the closure between deck and bulb-T units provides further economies by greatly simplifying formwork and eliminating shoring. Testing assured not only the short development length of reinforcement but also ultimate strength capacity of transverse and longitudinal closure pours. Further, best practices for formwork, closure design, UHPC mixing and placement, and quality assessment are considered.

17. Keywords: UHPC, accelerated construction, closure pours	18. Distribution Statement: No Restriction

19. Security Classification (of this report): Unclassified	20. Security Classification (of this page): Unclassified	21. No. of Pages: 233	22. Price: Free

Form DOT 1700.7 (8-72) Reproduction of completed page authorized.

GDOT Research Project 18-01

Final Report

DEVELOPMENT OF GDOT ULTRA-HIGH PERFORMANCE CONCRETE FOR BRIDGE DECK CLOSURE POURS

By

Lauren Stewart, PhD, PE
Associate Professor – School of Civil and Environmental Engineering

Lawrence Kahn, PhD, PE
Emeritus Professor – School of Civil and Environmental Engineering

Kimberly Kurtis, PhD
Professor – School of Civil and Environmental Engineering

Aaron Miller, Sung Yeob Lim, Griffin Fish
Graduate Research Assistants

Georgia Institute of Technology

and

Giovanni Loreto, PhD
Assistant Professor – Department of Architecture

Kennesaw State University

Georgia Tech Research Corporation

Contract with
Georgia Department of Transportation

In cooperation with
US Department of Transportation
Federal Highway Administration

April 2022

SI* (MODERN METRIC) CONVERSION FACTORS

APPROXIMATE CONVERSIONS TO SI UNITS

Symbol	When You Know	Multiply By	To Find	Symbol
		LENGTH		
in	inches	25.4	millimeters	mm
ft	feet	0.305	meters	m
yd	yards	0.914	meters	m
mi	miles	1.61	kilometers	km
		AREA		
in^2	square inches	645.2	square millimeters	mm^2
ft^2	square feet	0.093	square meters	m^2
yd^2	square yard	0.836	square meters	m^2
ac	acres	0.405	hectares	ha
mi^2	square miles	2.59	square kilometers	km^2
		VOLUME		
fl oz	fluid ounces	29.57	milliliters	mL
gal	gallons	3.785	liters	L
ft^3	cubic feet	0.028	cubic meters	m^3
yd^3	cubic yards	0.765	cubic meters	m^3
		NOTE: volumes greater than 1000 L shall be shown in m^3		
		MASS		
oz	ounces	28.35	grams	g
lb	pounds	0.454	kilograms	kg
T	short tons (2000 lb)	0.907	megagrams (or "metric ton")	Mg (or "t")
		TEMPERATURE (exact degrees)		
°F	Fahrenheit	5 (F-32)/9 or (F-32)/1.8	Celsius	°C
		ILLUMINATION		
fc	foot-candles	10.76	lux	lx
fl	foot-Lamberts	3.426	$candela/m^2$	cd/m^2
		FORCE and PRESSURE or STRESS		
lbf	poundforce	4.45	newtons	N
lbf/in^2	poundforce per square inch	6.89	kilopascals	kPa

APPROXIMATE CONVERSIONS FROM SI UNITS

Symbol	When You Know	Multiply By	To Find	Symbol
		LENGTH		
mm	millimeters	0.039	inches	in
m	meters	3.28	feet	ft
m	meters	1.09	yards	yd
km	kilometers	0.621	miles	mi
		AREA		
mm^2	square millimeters	0.0016	square inches	in^2
m^2	square meters	10.764	square feet	ft^2
m^2	square meters	1.195	square yards	yd^2
ha	hectares	2.47	acres	ac
km^2	square kilometers	0.386	square miles	mi^2
		VOLUME		
mL	milliliters	0.034	fluid ounces	fl oz
L	liters	0.264	gallons	gal
m^3	cubic meters	35.314	cubic feet	ft^3
m^3	cubic meters	1.307	cubic yards	yd^3
		MASS		
g	grams	0.035	ounces	oz
kg	kilograms	2.202	pounds	lb
Mg (or "t")	megagrams (or "metric ton")	1.103	short tons (2000 lb)	T
		TEMPERATURE (exact degrees)		
°C	Celsius	1.8C+32	Fahrenheit	°F
		ILLUMINATION		
lx	lux	0.0929	foot-candles	fc
cd/m^2	$candela/m^2$	0.2919	foot-Lamberts	fl
		FORCE and PRESSURE or STRESS		
N	newtons	0.225	poundforce	lbf
kPa	kilopascals	0.145	poundforce per square inch	lbf/in^2

*SI is the symbol for the International System of Units. Appropriate rounding should be made to comply with Section 4 of ASTM E380. (Revised March 2003)

TABLE OF CONTENTS

LIST OF FIGURES

LIST OF TABLES

EXECUTIVE SUMMARY

Ultra-high performance concrete (UHPC) is a relatively new type of concrete that has been implemented in bridge construction in many states. UHPC has improved mechanical properties such as higher compressive and tensile strengths than conventional concrete. In bridge construction, UHPC can be used as joint pour between precast structural elements such as deck panels and bulb-T girders. The usage of UHPC can significantly reduce construction time and long-term maintenance cost of bridges. However, commercially available UHPC is prohibitively expensive and, therefore, is not currently widely in bridge construction. For this reason, many studies have worked to develop a non-proprietary UHPC mix design. Often, silica fume is used as a key component in UHPC, however, it is not easily accessible in Georgia. This research focuses on developing and evaluating a non-proprietary UHPC mix design using locally available materials in the state of Georgia. Metakaolin and Type F fly ash were both considered as supplementary cementitious materials (SCMs) instead of silica fume, with metakaolin being most advantageous.

In this investigation, a UHPC mix is designed, implemented, and tested to meet baseline mechanical properties. The mix design demonstrates the required 28-day compressive strength of at least 18,000 psi. The UHPC mix then underwent testing to further investigate its feasibility in accelerated bridge construction structural applications. Precast concrete deck panels were joined together by a closure pour filled with UHPC and these panels were tested to determine UHPC joint performance. The deck panel

specimen tested in this research has demonstrated that the non-proprietary UHPC is well-suited for this application.

CHAPTER 1. INTRODUCTION

MOTIVATION

With ever-growing populations comes an increasing need for sustainable transportation infrastructure. To meet modern transportation demands, it is necessary to build new infrastructure and rehabilitate existing roads and bridges. Work must be completed efficiently to mitigate construction-induced traffic congestion, delays, and disruptions. Many states' Departments of Transportation (DOTs) have adopted accelerated bridge construction (ABC) to minimize the negative impacts of infrastructure improvement. ABC is a construction technique that can significantly reduce construction time and potentially improve service lives of bridges. ABC allows state DOTs to efficiently build and rehabilitate bridges without additional strain on already-congested highways.

The temporal advantage of ABC stems partially from use of precast structural elements. Bridge components, such as deck panels and decked bulb tee girders, can be made offsite and brought to the construction site. These structural elements are then joined together at connection regions using grout or concrete that can transfer the required shear and moment induced from traffic loads. To successfully join multiple structural elements, the connection regions require significant width and extensive reinforcement detailing. The involved processes in constructing joint connections and assembling the structural elements are often labor-intensive and expensive.

The development of ultra-high performance concrete (UHPC) has paved the way to simplify the construction processes of the aforementioned connection details. Due to its improved mechanical properties compared to conventional concrete and high performance

concrete (HPC), UHPC can reduce connection width and reinforcement detailing. However, commercially available UHPC is proprietary is expensive. The steep price of commercially available UHPC inhibits its potential for widespread use in infrastructure development and rehabilitation projects. To address this issue, Georgia Department of Transportation (GDOT) is among the many entities investigating the application of non-proprietary UHPC mix comprised of locally-available materials that is less expensive than existing proprietary mixes, specifically for use in precast deck closure pours.

RESEARCH OBJECTIVES

The objectives of this research are as follows:

1. To develop and evaluate a satisfactory non-proprietary UHPC mix that uses materials locally available from the state of Georgia and can achieve a 28-day compressive strength of at least 18,000 psi and a tensile strength of 750 psi.

2. To create a material testing protocol that demonstrates the required mechanical properties and that can be used for further evaluation of materials by contractors.

3. To develop and conduct structural experiments that validate the ability of the UHPC material to be used for precast deck panel closure pours.

4. To provide recommendations for specifications regarding the use of the non-proprietary UHPC for closure pours.

REPORT ORGANIZATION

Chapter 2 provides a literature review and discusses numerous studies of UHPC that have been conducted across different entities. General material composition of UHPC is

examined followed by UHPC mix design processes. This chapter also presents and compares mechanical properties of UHPC such as compressive strength and flexural performance. Finally, the chapter provides a summary of UHPC projects in Georgia and the availability of materials in the region.

Chapter 3 presents material studies that were conducted at the laboratory scale. The chapter describes the effects of cement type, sand, mix procedure, water-to-binder ratio, among others, on UHPC properties.

Chapter 4 gives a description of the production-scale studies that used larging batching. This chapter discusses, in detail, the effects of mixing procedure and alternative sand on UHPC properties.

Chapter 5 presents a standard protocol for mixing and mechanical testing that was used in all future experiments.

Chapter 6 delves into the specifics of the mix design as well as the mechanical properties of UHPC. Compressive strength and flexural performance of the non- proprietary UHPC are presented in this chapter.

Chapter 7 includes the structural evaluation experiments. It outlines the construction of structural test specimens, the experimental setup, as well as results.

Chapter 8 provides a cost estimate of producing the developed UHPC. It also provides a comparison to proprietary UHPC.

Chapter 9 includes the concluding remarks of the research as they relate to the research objectives. It also provides recommendations for specifications and for future work.

CHAPTER 2. LITERATURE REVIEW

UHPC is a relatively new type of concrete that is advantageous to the civil engineering industry due to its increased strength. In the United States, UHPC has been used in prestressed concrete girder bridges, precast concrete deck panels, and field-cast connections between prefabricated bridge components.[1] Compared to conventional concrete, UHPC has improved mechanical properties including higher compressive strength, higher ductility, and efficient particle packing density. The lack of coarse aggregates in the mix design and the usage of fine aggregates and cementitious materials such as fly ash and silica fume contribute to the efficient particle packing density and low porosity of UHPC. UHPC has very low water-to-cementitious materials (w/cm) ratio compared to conventional concrete. Because the w/cm is so low, workability is achieved by using high-range water reducers (HRWR) that allow the concrete mix to be easily placed without compromising strength. Due to its favorable mechanical properties and versatility, many studies have investigated optimizing the mix design of UHPC to accommodate local material availability and investigated UHPC as a vital construction material in bridge rehabilitation.[2]

MATERIAL COMPOSITION OF UHPC

Unlike conventional concrete, the material composition of UHPC does not include coarse aggregates and has a significantly lower water-to-cement ratio. Fine sand, generally between 150 and 600 µm, is used in making UHPC and is the largest constituent in the mix apart from steel fibers.[3] The next largest particle is cement, which has a typical particle size of 1 to 50 µm. Ground quartz, with a size of 10 µm, is also widely used. Silica fume, the smallest particle among the constituents, has a size of 0.1 – 0.3 µm.

Silica fume is a widely used material for UHPC due to its high reactivity and ultra-fine particle size.[4] The particle sizes of the constituents allow UHPC to have a finely graded and homogeneous matrix.[5]

Steel fibers are also a key component of the UHPC mix design. The addition of steel fibers allows UHPC to have more ductility and tensile load carrying capacity than conventional concrete. The tensile strength and dimensions of steel fibers vary depending on the manufacturer. Table 1 shows the typical material composition of UHPC.

Table 1. Typical UHPC composition.[3]

Material	Weight (lb) per cubic yard	Percent by Weight
Portland Cement	1,200	28.5
Fine Sand	1,720	40.8
Silica Fume	390	9.3
Ground Quartz	355	8.4
Superplasticizer	51.8	1.2
Accelerator	50.5	1.2
Steel Fibers	263	6.2
Water	184	4.4

Due to the low w/cm ratio in UHPC, workability is acquired using HRWR. In this study, MasterGlenium 7920®, a poly-carboxylate based admixture from Master Builders Solutions, is used.

UHPC MIX DESIGN METHOD

The early development of UHPC mixes relied upon optimized particle packing to generate material blends with low porosity and high compressive strengths.[6,7] The process of particle packing optimization increases the strength of the concrete by

minimizing the amount of void space present in the material, filling the voids instead with additional aggregate or cementitious material. There are two methods of particle packing optimization that are commonly utilized: the Compressible Particle Model (CPM) and the Modified Andersen-Andreasen Model. In addition, mixes are commonly designed in a test-matrix approach, whereby one baseline mix is continuously trialed with one mix variable at a time being adjusted.

The Compressible Particle Model

The CPM was developed by Francois de Larrard in 1999.[8] This method uses the particle size distribution of its component particles (both reactive and nonreactive) alongside their virtual packing densities to calculate a compaction index, *K*. Additionally, this model considers both the wall effect, the perterbation that walls cause to the dispersion of particles, and the loosening effect, whereby smaller particles wedge larger particles apart and decrease their packing coefficient.[8] The Compressible Particle Model has been shown to perform well for large, easily-measureable particles such as aggregates, but it is very sensitive to the particle size distributions in finer materials like cement.[9]

To calculate the packing index *K*, users of the CPM must first calculate the maximum theoretical packing density of each particle size, γ. In order to do this, the user must also know each particle's maximum possible packing density, β, the volumetric proportion of each particle size, y, and the loosening coefficient and wall coefficients, a_{ij} and b_{ji}. The equations for the model are given in Figure 1. The loosening coeffecient is calculted via the first equation, while the wall effect coefficient is calculated via the second equation. These values are then used in the third equation to calculate γ.

$$a_{ij} = \sqrt{1 - \left(1 - \frac{d_j}{d_i}\right)^{1.02}}$$

$$b_{ji} = 1 - \left(1 - \frac{d_i}{d_j}\right)^{1.5}$$

$$\gamma_i = \frac{\beta_i}{1 - \sum_{j=1}^{i-1}\left[1 - \beta_i + b_{ij}\beta_i\left(1 - \frac{1}{\beta_j}\right)\right]y_j - \sum_{j=i+1}^{n}\left[1 - \frac{a_{ij}\beta_i}{\beta_j}\right]y_j}$$

Figure 1. Equation. Theoretical packing density.

Upon solving for γ_i, the value *K* can be found as the sum of all of the partial packing densities, as shown in Figure 2. In this equation, Φ is the actual packing density of the whole concrete mixture. For a self-consolidating concrete, de Larrard recommends that *K* = 4.[8]

$$K = \sum_{i=1}^{n} K_i = \sum_{i=1}^{n} \frac{y_i/\beta_i}{1/\Phi - 1/\gamma_i}$$

Figure 2. Equation. Packing index, K.

The CPM assumes that all particles are spherical in shape, that wall interactions only occur against smooth, flat walls, and that the intrusion of fibers can be ignored due to their relatively short length.[8]The maximum packing density, β, is determined using a variety of experimental methods to find the maximum measured packing density, then back-calculating the virtual packing density using a correction factor.[8,10] Some of these experimental methods can be overly-harsh towards soft grains like limestone (a common filler material in UHPC) because they crush the grains into a finer powder, providing

inaccurate results.[11] In his own paper on using the CPM for mix design, de Larrard provides no clarification on how to consider the virtual packing density.[12]

The Modified Andersen and Andreasen Model

The original Andersen and Andreasen model was first published in 1930, and involves using a target function based on an infinite distribution of particle sizes.[13] Because there must be finite size limits, Funk and Dinger modified the model to include a minimum particle diameter. The modified equation is shown in Figure 3, where *P(D)* is the fraction of total solids smaller than diameter *D*, and *q* the distribution modulus.[14] This equation generates an "ideal" gradation curve when presented graphically, which mix designs can be visually adjusted to match.

$$P(D) = \frac{D^q - D_{min}^q}{D_{max}^q - D_{min}^q}$$

Figure 3. Equation. Modified Andersen and Andreasen model.

The variable *q* is not a fixed or measurable variable, but instead is a variable to be adjusted until the particle size distribution curve of the selected materials is as close as possible to an "ideal" particle size distribution. It has been found that the optimal packing density for a mixture that is flowable and self-consolidating can be obtained by using a value of *q* between 0.22 and 0.25.[15-17]

Test Matrix Mix Design

Test matrix-based mix design has been used extensively to design non-proprietary mixes in Arkansas[18], Colorado[19], Michigan[20], Montana[21], and South Carolina[22], and for other geographic regions around the United States.[23] This procedure requires less

calculations than using a particle packing model but requires much more experimental work and a greater expenditure of materials. Published papers that have utilized a matrix-based frequently include sections addressing particle packing in the cement paste, but correlate the higher particle packing with increased workability in measures such as the ASTM C1611 spread test.[23] In a typical UHPC test matrix design, the first step is establishing a baseline mortar mix. The baseline mix can either be based off a previous successful mix design from literature, or a new mortar can be developed. Once a baseline has been established, each component of the mix design is then tested for strength via compression testing and for workability via flow table testing. These components are then weighted against the objectives of the mix designer to determine if the mix is successful.

MECHANICAL PROPERTIES OF UHPC

Compressive Strength

Across numerous studies, a wide range of mechanical properties is observed depending on the materials used and the way the UHPC was cured. In Federal Highway Administration's (FHWA) 2006 report, mechanical properties of a commercially available UHPC, Ductal®, were investigated.[5] Steam-treated and untreated UHPC specimens demonstrated an average strength of 28.0 ksi and 18.3 ksi, respectively.[5] Another study showed compressive strength of UHPC to be 25.8 ksi when cured at room temperature.[24]

Table 2 summarizes compressive strength of various UHPC mix designs across numerous studies.

Table 2. 28-day compressive strength of UHPC from previous research.

Research led by	Compressive Strength (ksi)
Graybeal	18.3 – 28.0[25]
US Army Corps of Engineers	25.9 – 31.3[26]
Kim Huy Hoang, Philipp Hadl, Nguyen Viet Tue	27.7 – 28.6[27]
MDOT, Ahlborn, Peuse, Misson	23.9 – 31.1[28]
MDT, Berry	19.2[29]
Ahmad, Hakeem, Maslehuddin	23.4[30]

The variation of compressive strength in the above table is due to several factors such as varying material composition, w/cm, percentage of steel fibers by volume, and curing regime. For example, variation of curing conditions caused specimens from Graybeal to vary from 18.3 – 28.0 ksi. One curing regime subjected specimens to 48 hours of curing in a steam environment (90˚C, 95% humidity) followed by a standard laboratory environment (22˚C, varying humidity) until testing.[25] The other specimens in this research were only subjected to standard laboratory environment until testing. The average 28-day compressive strength of steam-treated specimens was 28 ksi, versus 18.3 ksi for untreated specimens.

The above studies also used silica fume as a key component in the mix design. Silica fume helps improve mechanical properties of the matrix by eliminating voids between particles due to its fineness. It also enhances rheology and secondary hydrates.[31]

However, careful attention must be given in determining the amount of silica fume used in the mix design. A high amount of silica fume in the UHPC mix will require a larger dose of HRWR because of the relatively high surface area to volume ratio of the particles. Using excessive amount of HRWR can cause bleeding or segregation of constituents in UHPC.[31]

Tensile Strength

Different experimental methods such as direct tension, splitting cylinder, and four- point bending of beams were used to determine tensile capacity of UHPC specimens across numerous studies.[32] Graybeal followed procedures from ASTM E8, which is typically used for tension testing of metallic materials, to measure the direct tensile strength of UHPC specimens. Pilot tests were conducted using 1.0 in. by 2.0 in. by 11.9 in. rectangular prisms to determine viability of applying the concepts of the mechanical tests for metals to strain-hardening concretes.[33] After adjusting various parameters such as configuration, thickness, shape, and bond length of grip plates, Graybeal confirmed viability of applying ASTM E8 procedures to test the tensile strength of UHPC. Specimens with 2 in. cross section and lengths of 12 in. and 17 in. were gripped at each end and subjected to a maximum tensile load of approximately 180 kN (40.4 kip).[34] Figure 4 shows the configuration used in this study for the two types of specimens. Strain measurements were taken along the gauge length centered on the mid-length cross section. A parallel ring extensometer with four linear variable differential transformers (LVDTs) were used to measure strain. The results from this study showed a range of 1.24 ksi to 1.68 ksi of average ultimate strength of specimens.

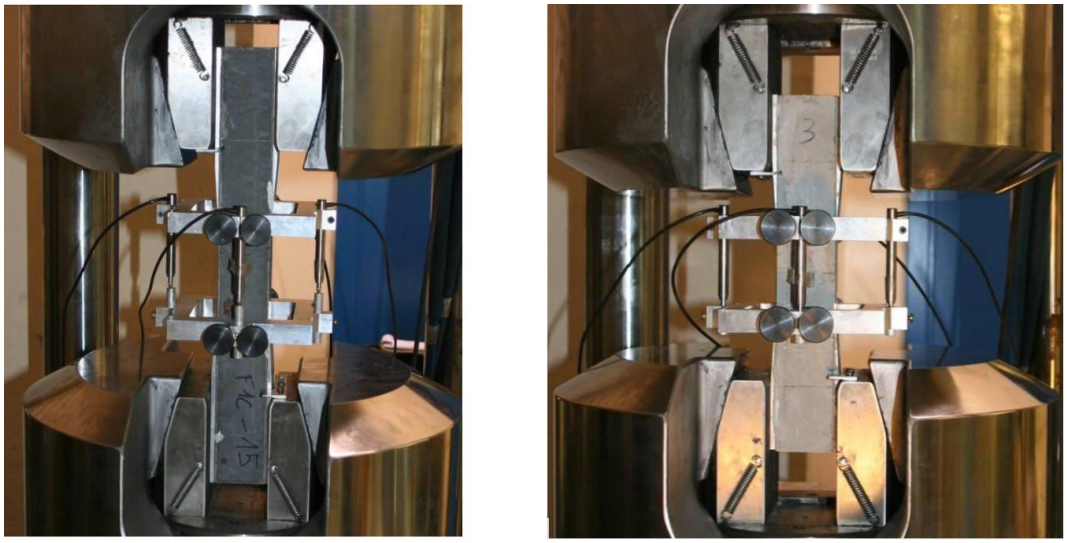

Figure 4. Photo. UHPC direct tension test configuration for 17 in. (left) and 12 in. (right).[34]

Graybeal also measured flexural tensile capacity of UHPC specimens according to procedures outlined in ASTM C1609. Peak strength at first crack and peak strength beyond first crack are determined. Figure 5 shows a typical configuration of the four-point bending test. This research employed three different four-point bend test geometries to investigate flexural behavior of UHPC. Load and midspan deflection were measured during the test period. The associated maximum equivalent bending stress, σ_{equi}, is calculated using the equation in Figure 6. In the equation, M is the maximum moment, *b* is the base of the cross section, and *h* is the height of the cross section. The results are summarized in Table 3 for different UHPC batches and test configurations.

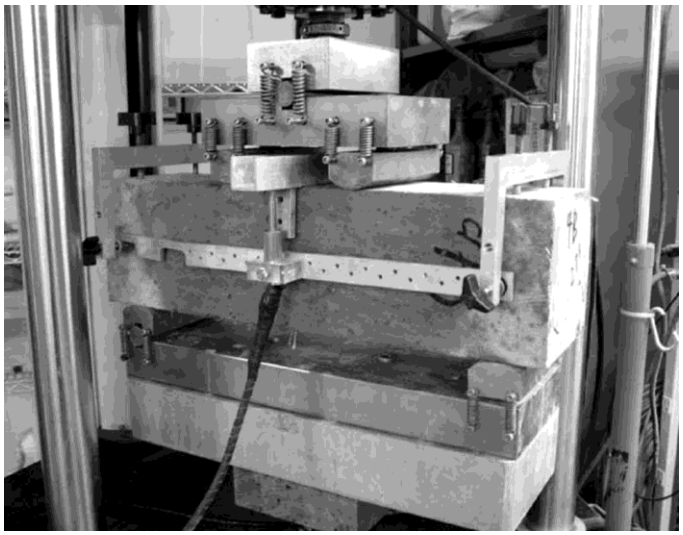

Figure 5. Photo. ASTM C1609 four-point bending configuration.[33]

$$\sigma_{equi} = \frac{6M}{bh^2}$$

Figure 6. Equation. Maximum Equivalent Bending Stress.

Table 3. Maximum average equivalent bending stress for varying UHPC batches and test configurations.[33]

Batch Name	Test Configuration	Number of Specimens Tested	σ_{equi} (ksi)
B2	S	5	4.07
	L	6	4.20
	B	6	3.82
F1A	S	6	3.50
	L	5	3.92
F2A	S	6	2.62
	L	5	3.42
F1B	S	6	3.10
	L	5	3.21
F1C	S	6	4.04
	L	5	4.13

Another research effort performed by Engineer Research and Development Center (ERDC) at U.S. Army Corps of Engineers investigated the flexural performance of UHPC. ERDC investigated and evaluated the performance of Cor-Tuf, a UHPC mix developed at ERDC. Three different dimensions of UHPC beams were tested with and without fibers using steps outlined in ASTM C1609. Table 4 summarizes the average flexural strength of different beam specimens with steel fiber reinforcement. Flexural strength was also calculated using Figure 6. Test results of total applied load versus midspan displacement of 25 mm (0.984 in.) beams with fibers are shown in Figure 7. Steel fibers with tensile strength of 1100 MPa (159.5 ksi) used in this research are shown in Figure 8. The legend shows labels F1 to F9, which represent batch numbers of UHPC with fiber reinforcement. The fibers are 30 mm (1.18 in.) long with a diameter of 0.55 mm (0.217 in.) and are hooked at both ends. Cor-Tuf batches used in this research employed 3.6% of steel fibers by volume.[35]

Table 4. Flexural performance of Cor-Tuf beam specimens.[35]

Beam dimension [l by w by h] in mm (in.)	Average Flexural Strength (psi)	Standard deviation (psi)	Coefficient of variation (%)
356 by 102 by 25 (14 by 4 by 1)	3480	276	8
356 by 102 by 102 (14 by 4 by 4)	4293	116	2.8
1016 by 102 by 102 (40 by 4 by 4)	3466	391	11

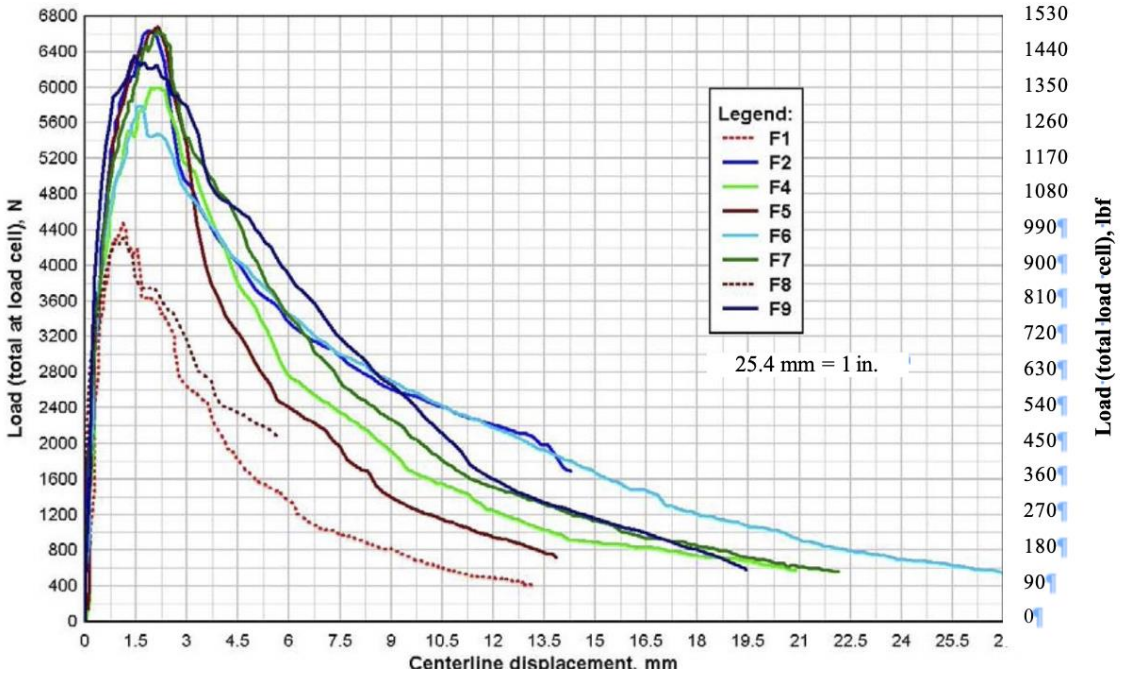

Figure 7. Graph. Applied load versus centerline displacement graph from Cor-Tuf flexural performance test.[35]

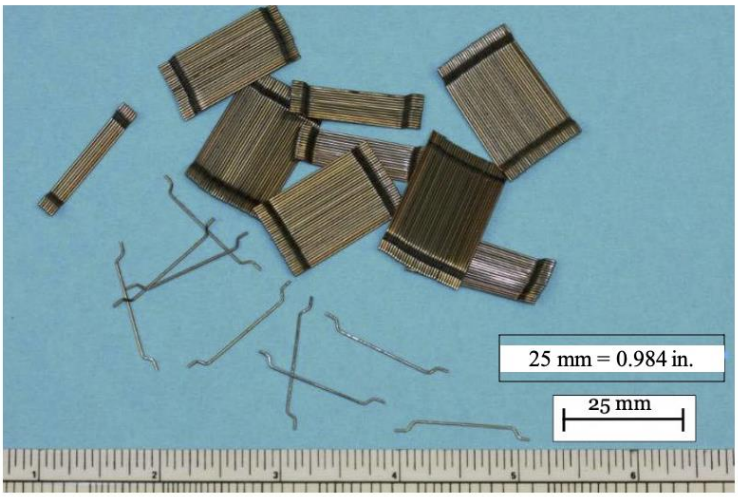

Figure 8. Photo. Hooked end fibers used in Cor-Tuf mix design.[35]

As shown in Figure 7, the initial response of all the specimens is relatively linear. After the linear response, the specimens shifted to a nonlinear response until reaching the peak load, followed by a softening response.[35] Disregarding the two outliers, the greatest variability between specimen responses is observed after the peak load. Two possible

causes for this variability are the material characteristic and effects due to experimental setup. The random distribution and orientation of steel fibers could be the main contributing factor in variability of the post peak load response of specimens.

UHPC AS JOINT BETWEEN STRUCTURAL ELEMENTS

Shear keys are used to transfer forces through joints and to prevent relative vertical displacements between structural elements, such as deck panels and decked bulb-T girders. The structural integrity and durability of concrete used in the shear key is vital to the successful performance of a bridge constructed using precast concrete components.[36] Two advantages of using UHPC as connection material are simplicity and performance. UHPC allows for small, simple connections without requiring post-tensioning or large volumes of field-cast concrete.[37] When used as a connection material between structural elements, UHPC allows for a significantly simpler reinforcement layout compared to when field cast grout is used, as shown in Figure 9. The dense and discontinuous pore structure that is further reinforced with steel fibers allows UHPC to have a more homogeneous stress distribution, better confinement of embedded rebar, and reduced development and splice lengths compared to ordinary concrete.[38]

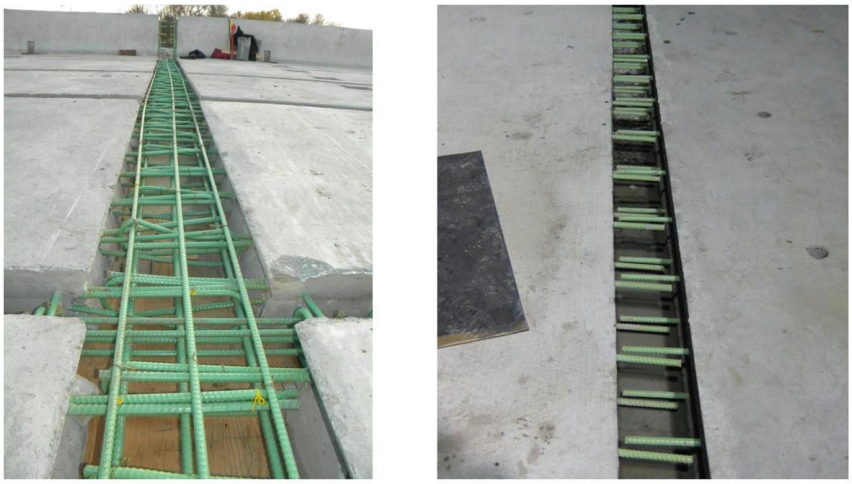

Figure 9. Photo. Joint detail using field cast grout (left). Joint detail using UHPC (right).[38]

Figure 10 shows a UHPC connection detail between precast structural decks used by New York State DOT (NYSDOT) on I-81 in Syracuse, New York. The rebars extrude into the UHPC connection area by 5-1/4 in. with lap length of only 4 in.

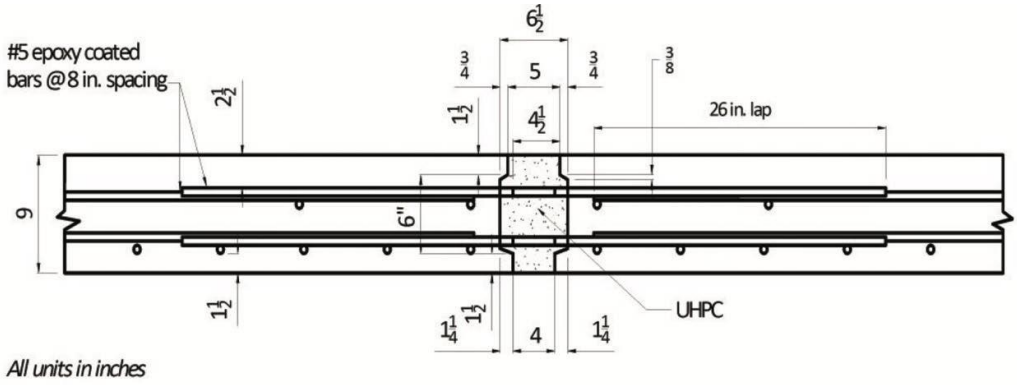

Figure 10. Engineering Drawing. Joint detail of precast concrete decks used by NYSDOT.[37]

As is evident from Figure 9, using UHPC as a connection material can help reduce the connection width. Along with simpler reinforcement layout, the reduced amount of material needed in the connection region can compensate for the relatively higher price of

UHPC. The simplicity of connection details can also reduce the cost in labor, formwork, and materials.

Experimentation of UHPC Joint Between Precast Concrete Deck Panels

NYSDOT in conjunction with FHWA has conducted experiments to assess the performance of UHPC closure pour connections.[39] The tests focused on the structural performance of UHPC connection undergoing cyclic and monotonic truck wheel loading. Figure 11 and Figure 12 show the test setup used to assess longitudinal and transverse UHPC connection performance.

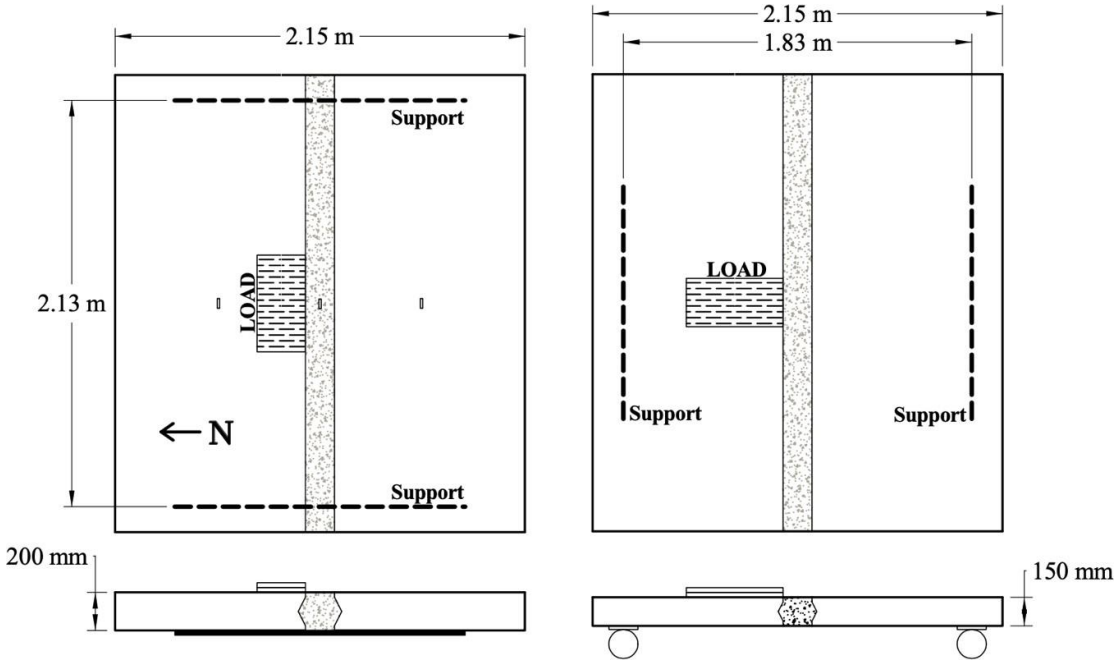

Figure 11. Schematic. Cyclic loading test configuration for deck panels connected using UHPC joint.[39]

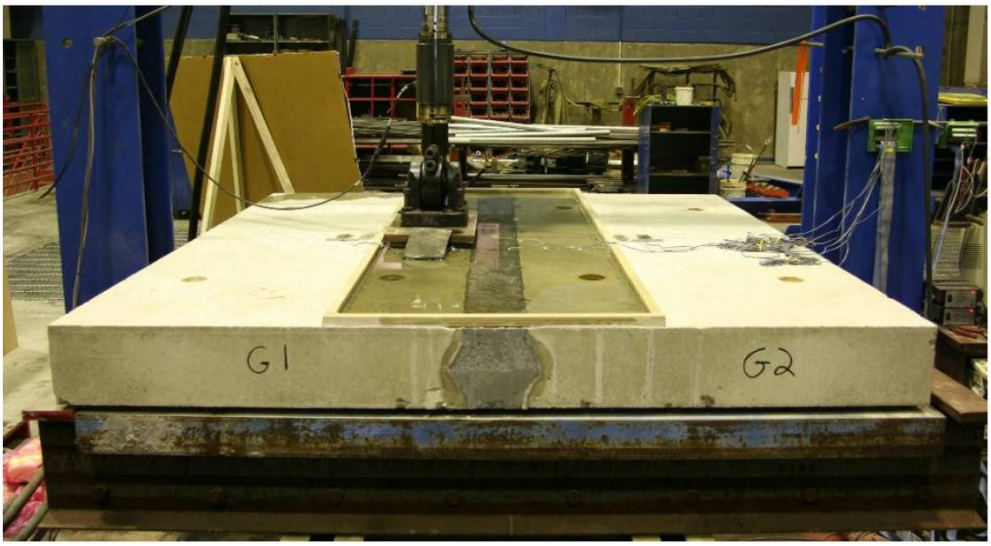

Figure 12. Photo. Cyclic loading configuration using triangular shear key.[39]

In the setup, the specimens were subjected to cyclic loads over a load range which generates a maximum tensile strain of 100 microns. This tensile strain value was used as a conservative upper limit estimate of what a concrete bridge deck would undergo during service. Initially, 2 million cycles with a peak load of 16 kips were applied. Then, absent signs of degradation, the load range was increased by a factor of 1.33 and 5 million additional cycles were applied. After the cyclic loads, each specimen was subjected to monotonically increasing load until failure. The specimens were monitored visually and electronically throughout the duration of the test for signs of concrete cracking, interface debonding, and flexural stiffness and strain distribution of specimens.

Figure 13 shows the strain and displacement results for one of the specimens. The strain per applied load remains relatively constant during the two phases of cyclic loading. This indicates that the load distribution across the joint through the bonds between the UHPC and precast concrete remained intact throughout the test.

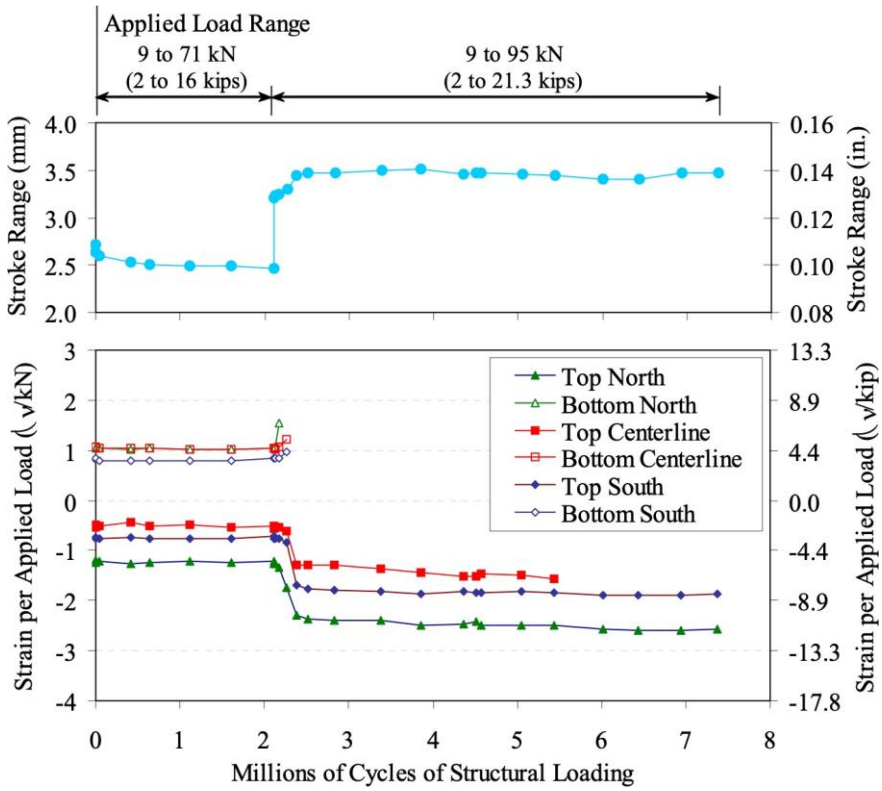

Figure 13. Graph. Strain and displacement results from cyclic loading test.[39]

In addition to the UHPC connection, FHWA has also conducted tests that compare the performance of different field-cast grout materials and connection details of precast concrete deck panels.[40] The general details of specimens used in this research are shown in Figure 14. The variation in lap splice lengths within the connection region between two deck panels is due to the varying development lengths of rebars embedded in different grout materials. The grout materials are G1, G1IC, M1, E1, and U2, which stand for non- shrink cementitious grout, non-shrink cementitious grout with internal curing, magnesium phosphate grout, epoxy grout, and UHPC, respectively.

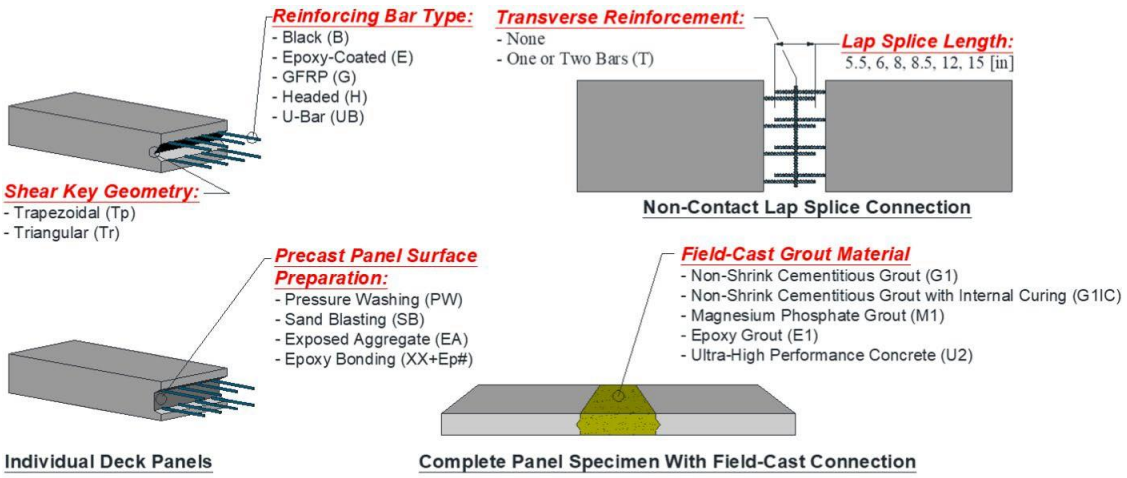

Figure 14. Schematic. Deck level connection specimens and test variables.[40]

The UHPC used in this experiment is a proprietary mix that was pre-blended and pre-bagged by the manufacturer. The pre-bagged powder was mixed with a phosphonate plasticizer, a polycarboxylate HRWR, a non-chloride accelerator, and steel fibers. The fibers were provided by a separate manufacturer from the UHPC. The nominal length and diameter of the fibers are 13 mm (0.512 in.) and 0.2 mm (0.008 in.), respectively. The tensile strength of fibers was specified by the manufacturer as 290 ksi.[40] The surface of the deck panels along the length of the joint had exposed aggregate (EA) finish with amplitude of 1/4 in. to provide bond between the grout materials and the concrete deck panels, as shown in Figure 15.

Figure 15. Photo. EA surface of a precast concrete deck.[40]

The specimens in this experiment were subjected to three different loading procedures applied in succession: pre-crack cyclic loading, post-cracking fatigue loading, and monotonic ultimate loading. If a specimen lost the capability to withstand further loading during one of the loading procedures, then subsequent loading was not applied.[40] Figure 16 shows the setup for a four-point bending test of the specimen.

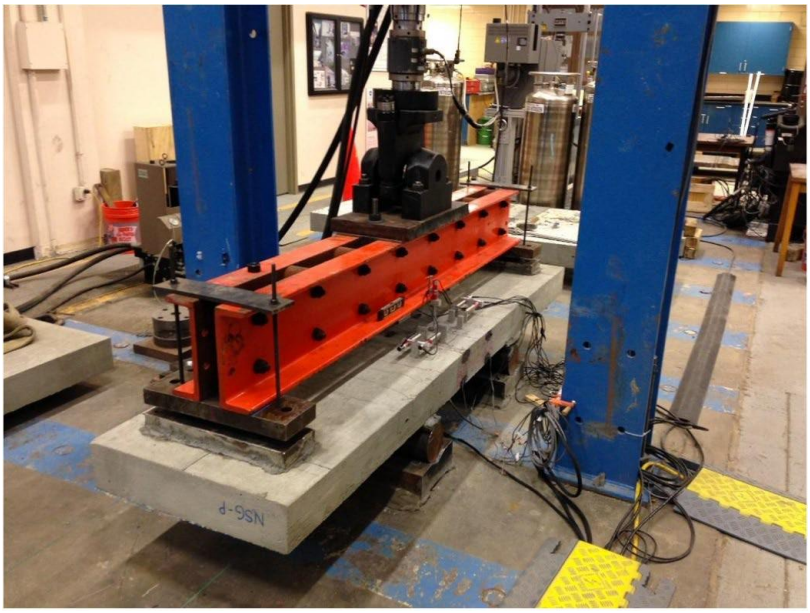

Figure 16. Photo. Deck panel specimen during loading.[40]

The applied load during pre-crack cyclic loading procedure ranged between 10 and 120 percent of the cracking moment, M_{cr}. During this procedure, observations were made to identify first cracking at the interface between precast concrete and grout materials. Premature interface cracking can lead to durability issues because external agents such as water and chloride can penetrate through the cracks. Most specimens that employed a non-shrink cementitious grout (G1) showed interface cracking even before the loads were applied due to shrinkage. All specimens that employed a magnesium phosphate rapid-setting cementitious grout (M1) showed interface cracking after 0.8 M_{cr} cycles. G1 and M1 grouts showed poor bonding with the precast concrete surfaces regardless of joint surface preparation. Specimens that used epoxy (E1) and UHPC (U2) grout fared well. Interface cracking were observed for all the specimens with sand-blasted joint surfaces using E1 grout at the 0.8 M_{cr} cycles. The remaining specimens showed interface cracking between 1.0 M_{cr} and the end of the loading procedure. The specimens that employed U2 grout without EA joint surface showed interface cracking at 0.8 M_{cr} cycles. All the specimens that had EA joint surface exhibited interface cracking beyond at least 1.2 M_{cr} cycle. The observations during and after the pre-crack cyclic loading indicate that UHPC performed better than all the other connection materials when EA surface preparation was employed. Figure 17 shows representative photographs of the connection regions after the loading procedure. Figure 18 shows a computerized drawing of cracks that occurred in the specimens using UHPC connection. The drawing shows that there were no cracks that occurred due to shrinkage.

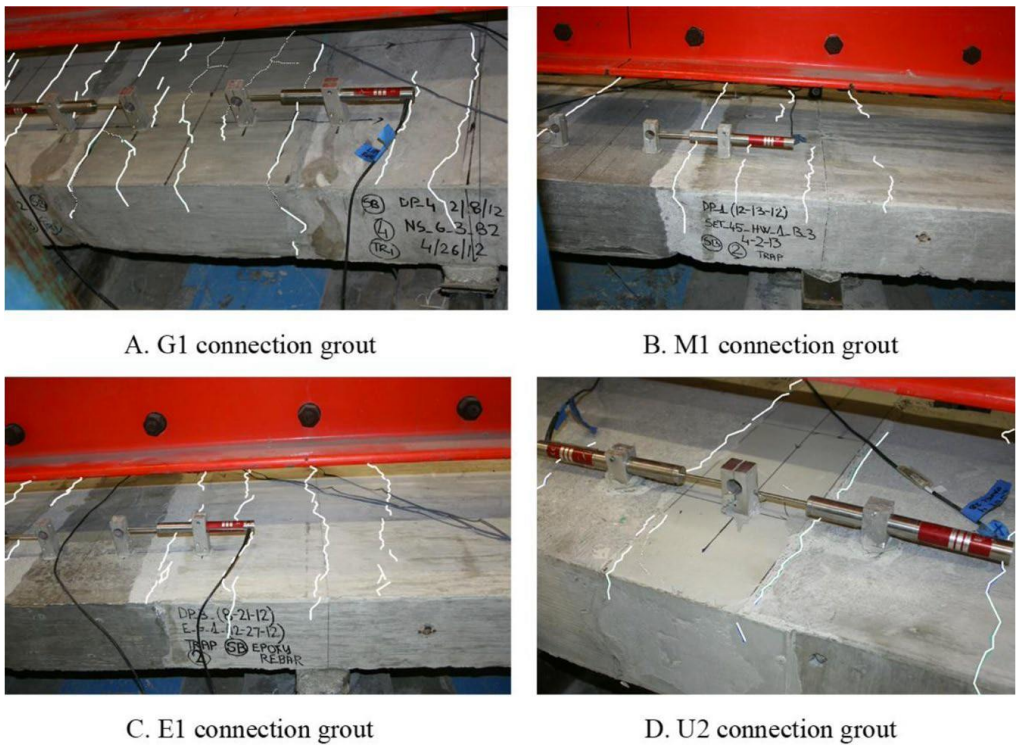

Figure 17. Photos. Representative photos of deck-level connection regions pre-cracking cyclic loading.[40]

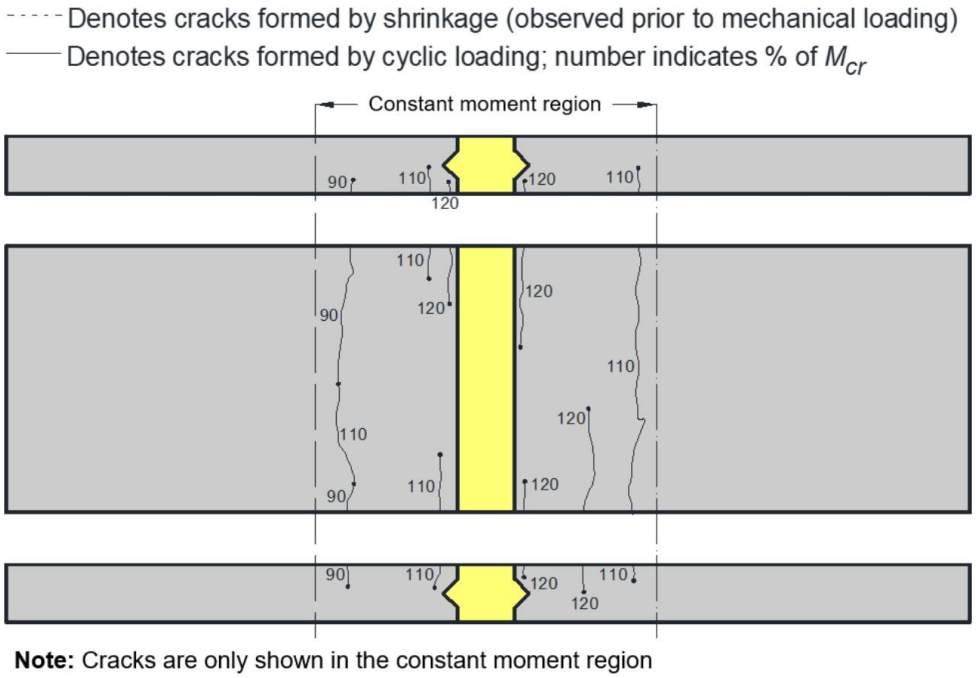

Figure 18. Schematic. Computerized illustration of damage progression during pre-cracking cyclic loading for a specimen employing UHPC connection.[40]

The lack of cracks within the connection region during pre-cracking cyclic loading indicates that when the UHPC connection fails, it will do so after the panels have failed. This particular investigation showed that the full flexural capacity of the deck panels was realized before failure occurred, due to concrete crushing, for specimens that employed UHPC connections.[40] The UHPC connections allowed the deck panel specimen to behave as though it were monolithically cast. The simpler connection detail, long-term maintenance cost, and durability of UHPC are some of the advantages of employing it as a connection material.[40]

ACCELERATED BRIDGE CONSTRUCTION IN GEORGIA

Accelerated bridge construction and UHPC has been used on two GDOT projects to date. The first structure in Georgia to incorporate UHPC was a bridge on State Road 211 over Beech Creek near Athens, GA. It consists of a single 148-foot span, with a 40-foot gutter-to-gutter width. Full depth precast deck panels 8.75 inches thick were used in place of a cast-in-place deck. The rebar overlap in the transverse and longitudinal joints was 5 in. The bottom of the transverse joint was designed to fit snugly to reduce the amount of necessary formwork, while the top was given a 2-in. gap to allow for UHPC placement. Additionally, UHPC was utilized in the shear connections. The UHPC used on the project was Ductal UHPC provided by Lafarge. Aside from the first placement day, pours were done in the night in order to avoid hot placement temperatures. [29] A diagram of the joint details is given in Figure 19 and Figure 20. The use of UHPC in this project allowed for accelerated bridge construction, with the bridge opening back up to traffic after only 60 days of construction.

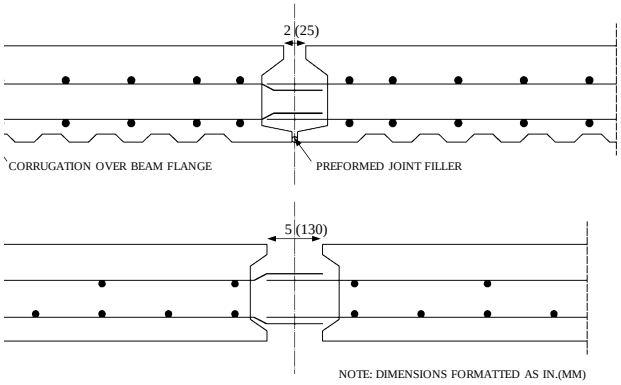

Figure 19. Typical transverse [top] and longitudinal [bottom] joint details from SR 211 Bridge.(41)

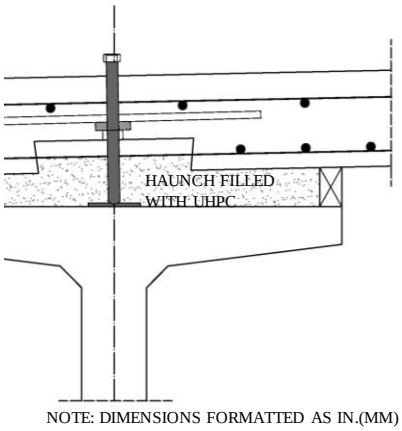

Figure 20. Engineering Drawing. Typical shear connection detail from SR 211 Bridge.(41)

The second bridge to be constructed with UHPC in Georgia was a bridge on County Road 131 in Henry County, Georgia. This bridge was constructed in the same manner as the previous State Road 211 bridge and all joint details were identical except for the transverse joints. After experiencing difficulties with placing UHPC in the 2-in. top opening of joints on the State Road 211 bridge, the transverse joints on the County Road 131 bridge were expanded to 5 in., as seen in Figure 21. Construction workers pouring UHPC into the joint is shown in Figure 22.

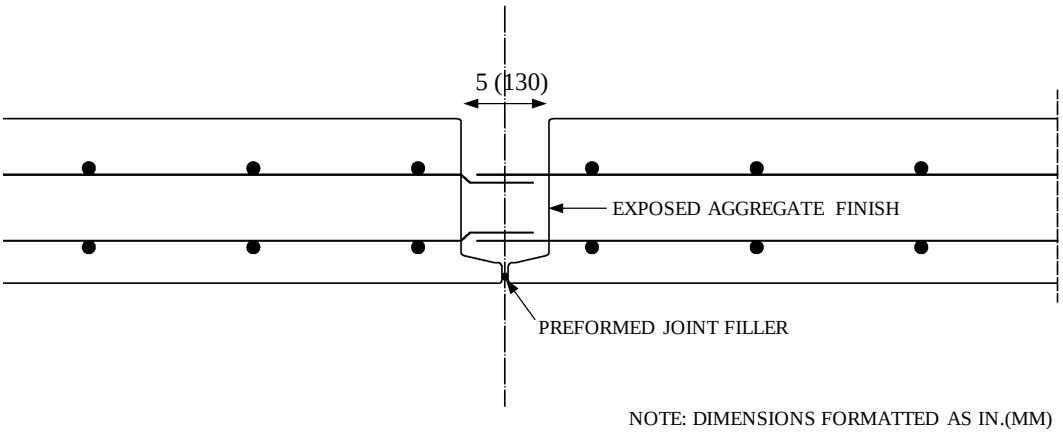

Figure 21. Engineering Drawing. Henry County / County Road 131 transverse joint details.

Figure 22. Photo. Workers fill a transverse joint on the County Road 131 Bridge with UHPC.

THE SUITABILITY OF LOCAL MATERIALS FOR UHPC

Georgia is home to two cement plants and 18 cement terminals, making cement easily accessible from all parts of the state.[42] Georgia also has a wealth of aggregate sources and is supplied by all major admixture suppliers. While Georgia has ample cement and aggregate sources, it is lacking in easy access to silica fume, a common supplementary cementitious material (SCM) used in the production of UHPC.

Silica fume's high reactivity and ultra-fine particle size contribute to developing a dense concrete matrix, greatly improving both the compressive strength and durability of the concrete.[43,44] While silica fume is the most common supplementary cementitious material used in UHPC, other ultra-fine materials such as limestone, powdered silica, powdered phonolite, and metakaolin have been found to be suitable replacements for silica fume in providing improved density and compressive strength.[45] Of these materials, Georgia has both limestone and kaolinite in plentiful supply. Georgia's limestone deposits have been well-documented as far back as 1916, but it is Georgia's kaolinite supply that sets it apart from other states. Georgia is one of the leading kaolinite-producing regions in the world.[46,47] The availability of metakaolin in Georgia makes it an attractive option as a replacement for silica fume, as it has been shown that metakaolin can perform as a suitable replacement for silica fume in UHPC.[48,49]

CHAPTER 3. LABORATORY-SCALE MATERIAL STUDIES

The first set of experiments that were conducted were at the laboratory scale and used a bench top mixer. These experiments focused on understanding the effects of multiple properties (e.g., cement type, sand, mixing protocol) on the workability of the material. The results of those studies are included in this chapter.

MIX DESIGN PROCESS

A dual approach for the mix design process was considered to find a workable mix and determine the degree to which it could be improved though particle packing. First a test matrix approach was taken to develop UHPC mixes that met performance criteria for workability and strength. The process followed is outlined in Figure 23. This approach built upon published non-proprietary UHPC mixes, substituting locally available materials to minimize cost. The approach first identified appropriate water-to-binder ratios (w/b) and then adjusted the superplasticizer content to achieve desired flow. This initial identified mixture is then used as a baseline mixture, with subsequent mixes changing one mix design variable at a time to observe the effects of the change. Upon completion of the test matrix approach, the final mix was evaluated for further optimization using particle packing.

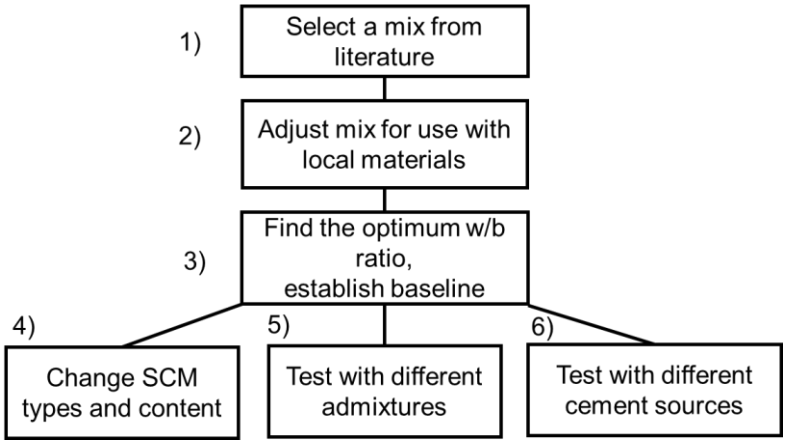

Figure 23. Schematic. Testing order for the parametric approach.

Each trial mix was evaluated based on compressive strength and workability. Compressive strength was evaluated by means of ASTM C109 and workability was evaluated via the ASTM C1437 flow table test. The compressive strength targets for the mix were 14,000 psi compressive strength at 3 days and 18,000 psi compressive strength at 28 days. The 14,000 psi target was chosen because it is the strength at which FHWA guidelines allow the development length of reinforcement to be taken as 8 bar diameters.[37] A mix that reaches 14,000 psi compressive strength quickly will enable construction to proceed at a more rapid pace. Compression testing specimens are shown in Figure 24. The 2-inch by 2-inch cube molds were used because they are the ASTM standard for testing mortars, which UHPC can be considered as due to the absence of coarse aggregates in the mix. Fibers were not included in these specimens because their contribution to compressive strength is marginal and because steel fibers were temporarily unavailable due to the effects of steel tariffs.[50]

Figure 24. Photo. Mortar cube specimens being cast for compression testing.

Due to the tight spaces and narrow joint widths, UHPC must be self-consolidating when used as a joint filler in ABC construction. No matter which materials are included in UHPC, it will be expected to be self-consolidating. For this reason, every mix was adjusted via the addition of superplasticizer until it reached a 9-inch-diameter flow on the ASTM C1437 test (Figure 25), plus or minus one half inch. The process by which these superplasticizer adjustments were made is detailed in below. The 9-inch target was chosen because it would allow for self-consolidating behavior upon the addition of workability-reducing steel fibers in the large-scale trials.[(51)]

Figure 25. Photo. ASTM C1437 flow test.

Following the parameterization approach, the software EMMA was used to conduct a particle packing optimization. Particle packing optimization eliminates void space in the concrete, creating a denser material with higher compressive strength. This optimization was done with the same materials used in the test-matrix trials. The software used for this optimizations uses the modified Andersen and Andreasen model to evaluate the particle packing of the mix design.[52] It was chosen for this process because it could easily and quickly evaluate a single mix, in a simple graphical interface, as opposed to the Compressible Particle Method, which requires complicated math and comprehensive testing to be done on each particle size used in the mix. The simplicity and ease of use of the modified Andersen and Andreasen approach made it ideal for optimizing a single mix.

MATERIALS

Three commercially produced cements readily available in Georgia were selected for testing: Holcim ASTM C150 Types I (Holcim; Duluth, Georgia), I/II (Argos; Atlanta, Georgia), and Type III (Argos; Atlanta, Georgia). The Bogue composition and Blaine

fineness of these cements, provided by the manufacturer, are shown in Table 5. These cements were chosen due to their low cost and widespread availability. The Type I cement was ordered as a baseline because of its relatively high C3S content. The Type I/II and Type III cements were included to evaluate the effects of decreasing the C3S content and the effects of increasing fineness, respectively.

Table 5. Cement composition.

Cement ID:	**Holcim Type I**	**Argos Type I/II**	**Argos Type III**
C_2S (%)	18	18	17
C_3S (%)	58	52	53
C_3A (%)	2	6	7
C_4AF (%)	13	9	10
SiO_2 (%)	20.5	20.1	20.4
Al_2O_3 (%)	4.4	4.4	4.9
Fe_2O_3 (%)	3.1	3.1	3.4
CaO (%)	64.1	62.7	63.6
MgO (%)	2.5	2.9	1.3
SO_3 (%)	3.3	3.1	3.6
CO_2 (%)	2	1.9	1.9
Limestone (%)	2.5	2.6	0
NaEq (%)	0.40	0.34	0.46
Loss on Ignition (%)	2.0	2.8	1.9
Blaine Fineness (m^2/kg)	394	394	538
Specific Gravity	3.10	3.16	3.15

Both ASTM C618 Class C and Class F fly ash were obtained locally (Boral Resources, Taylorsville, GA). Metakaolin (BASF Metamax, McIntyre, GA) was selected for testing due to its high purity and small particle size. This central location would serve to make it easily available throughout the state. This material is viewed as a potential substitute for silica fume, which is more commonly used in UHPC but is not produced in Georgia. One type of masonry sand (South Georgia Sand; Bainbridge, Georgia) was selected for initial testing. Masonry sand was selected because of its fineness and because fine sands are

generally used for UHPC. This masonry sand is alluvial, and gradation data for it is shown in Table 6 and Figure 26.

Table 6. Masonry sand gradation data.

Sieve Size	Masonry Sand
	Percent Passing (%)
#4	100
#8	99.99
#16	95.08
#30	63.98
#50	17.99
#100	1.53
#200	0.29
Fineness Modulus	**2.21**
Specific Gravity (ASTM C128)	**2.65**
Absorption Capacity (%) (ASTM C128)	**0.93**

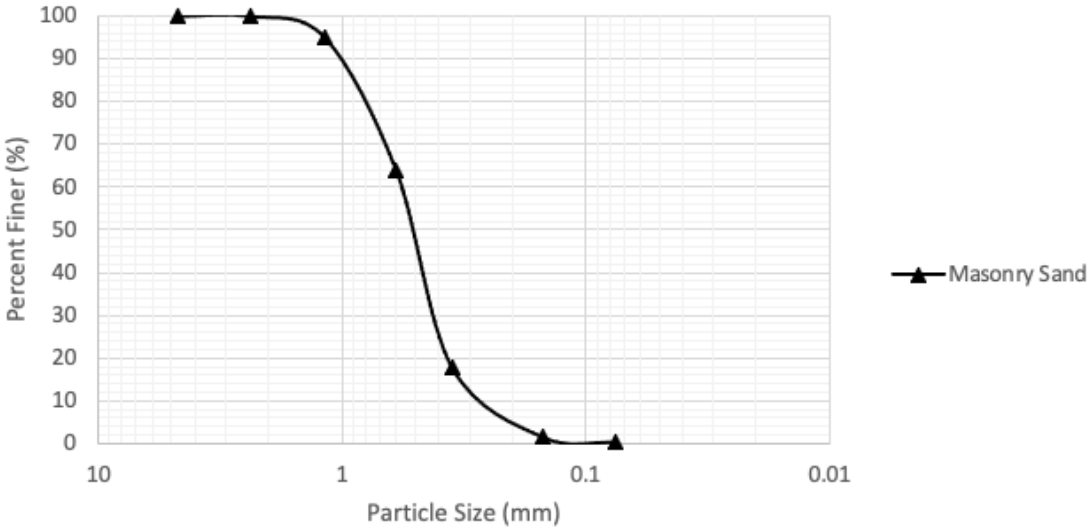

Figure 26. Graph. Masonry sand gradation curve.

Two widely available commercial superplasticizers were evaluated: Sika ViscoCrete 2100 and BASF MasterGlenium 7920. Both admixtures are polycarboxylate ether high-

range water reducers conforming to ASTM C494 requirements. Additionally, an accelerator (BASF MasterSet AC 534) was used in some mixes. These admixtures are all widely available and easily obtained in Georgia.

MIXING PROCEDURE

To conserve materials and aid in the ease of mixing, initial mixing was performed in 0.05 ft^3 batches. A 10-quart (0.33 ft^3) benchtop planetary mixer (Hobart) with a paddle blade was used to mix all mixture components. The following mixing procedure was adapted from several papers on UHPC mix development.[21,50,52]

1. Mix oven-dry sand and SCMs on low speed for 2 minutes
2. Add cement and mix on low for 1 minute
3. Add water over the course of 30 seconds and mix on low for a further 30 seconds
4. Add superplasticizer and mix on low for ten minutes
5. Test the material's flow
6. Cast specimens

If further flow was needed after step 5, superplasticizer was added in 2 mL doses and mixed for a further 2 minutes per dose until the mix reached 9 in. of flow. The mix would then be re-mixed following the above procedure with the adjusted amount of superplasticizer. This method allows for all mixes to be evaluated with the same mixing time. Superplasticizer was added after the water because it has been observed that delaying the addition of superplasticizer increases the fluidity of self-consolidating concrete and UHPC.[54,55]

CASTING AND TESTING PROCEDURES

Nine 2-in. by 2-in. by 2-in. cubic specimens were cast for each mix done. UHPC was allowed to flow into each mold until the mold was slightly over-filled, then the mold was struck five times with a mallet to drive out any air bubbles. The specimens were then trowelled down to the height of the mold, covered with plastic to prevent the escape of moisture, and allowed to set for 24 hours. After being removed from the molds the specimens were labelled and left to cure in a 73° F bath of water saturated with lime. Specimens were tested for compressive strength at 3, 7, and 28-day intervals, with three specimens being tested at each age. The cubes were loaded at a rate of 18,000 pounds per minute until failure.

MATERIAL CONSTITUENT STUDIES

The process of designing the mix followed a test-matrix based approach coupled with a particle packing analysis. First, a baseline mixture was established by adapting a mix from literature. Then this baseline mix was adjusted one component at a time to determine what effects the changed component would have on compressive strength, workability, or both.

As a starting point for the mix design, the general UHPC-4 mixture from the 2013 FHWA Tech Note Development of Non-Proprietary Ultra-high Performance Concrete for Use in the Highway Bridge Sector was selected for adjustment.[23] This mix was chosen because this UHPC was presented as being adaptable to materials found throughout the United States and was one of few that incorporated fly ash over other materials not found in Georgia, such as silica flour.

The UHPC-4 mix incorporates silica fume. Therefore, the first adaptation was to replace silica fume with metakaolin 1:1 by weight. Additionally, regular Portland cement was used in place of white Portland as an availability and cost-saving measure. This initial mix design is shown in Table 7.

Table 7. Initial UHPC mix.

UHPC-4 (Q; United States) [21]	
Material	**Quantity**
White Portland Cement	1248 lb/yd^3
Class F Fly Ash	303 lb/yd^3
Silica Fume	312 lb/yd^3
Masonry Sand	1871 lb/yd^3
Superplasticizer	45 lb/yd^3
Water/Binder: 0.154	

To begin the adjustments, silica fume was replaced with a one-to-one weight ratio with metakaolin, as seen in Table 8. This mix design was attempted twice, but neither attempt was successful in developing a cohesive mixture. Large agglomerations of metakaolin were observed in both mixes, and despite the addition of superplasticizer the cement and aggregates remained very dry and crumbly. The mixture was reapportioned to reduce the metakaolin content and to increase sand and fly ash, due to their lower cost and potential to improve workability. Additional water was also added for workability purposes. The adjusted mix is shown in Table 9. This mix proved to be workable, so testing proceeded to identify which w/b ratio would be set as the baseline value for use in following tests.

Table 8. One-to-one replacement of silica fume with metakaolin.

Material	Quantity
Type I Portland Cement	1248 lb/yd^3
Class F Fly Ash	303 lb/yd^3
Metakaolin	312 lb/yd^3
Masonry Sand	1871 lb/yd^3
Superplasticizer	45 lb/yd^3
Water/Binder: 0.154	

Table 9. Adjusted mix with reduced metakaolin.

Material	Quantity
Type I Portland Cement	1248 lb/yd^3
Class F Fly Ash	387 lb/yd^3
Metakaolin	100 lb/yd^3
Masonry Sand	1997 lb/yd^3
Superplasticizer	45 lb/yd^3
Water/Binder: 0.25	

Water to Binder Ratio

The mix in Table 9 was tested at w/b ratios of 0.14, 0.18, 0.25, and 0.30 to determine which w/b ratio would provide the highest strength. These w/b ratios were chosen to represent the wide range of w/b ratios that are commonly reported in UHPC literature. These mixes and their corresponding superplasticizer dosage are given in Table 10. It was found that the 0.18 w/b ratio provided the highest strengths of the w/b ratios tested.

Table 10. w/b ratio trial mixes.

Material	Quantity			
	0.14 W/B	**0.18 W/B**	**0.25 W/B**	**0.30 W/B**
Type I Portland Cement	1248 lb/yd^3	1248 lb/yd^3	1248 lb/yd^3	1248 lb/yd^3
Class F Fly Ash	387 lb/yd^3	387 lb/yd^3	387 lb/yd^3	387 lb/yd^3
Metakaolin	100 lb/yd^3	100 lb/yd^3	100 lb/yd^3	100 lb/yd^3
Masonry Sand	1997 lb/yd^3	1997 lb/yd^3	1997 lb/yd^3	1997 lb/yd^3
Superplasticizer (BASF 7920)	13.5 L/yd^3	8.64 L/yd^3	2.70 L/yd^3	1.62 L/yd^3
Water/Binder	0.14	0.20	0.25	0.30

Figure 27 shows the influence of w/b on strength development over time. A 0.18 w/b ratio (0.25 w/c ratio) was the only mix to surpass the 18,000 psi compressive strength target. It is believed that the 0.14 w/b mix (0.2 w/c) had its early strength hampered by the excessive amount of superplasticizer necessary to achieve workability. It was found that the 0.18 w/b ratio provided the highest strengths of the w/b ratios tested. From this, the "GT Baseline" mix was established, as shown in Table 11, and used for all future tests at the laboratory scale.

An interesting result, however, is that despite lower 3- and 7-day strengths, the 0.3 w/b mix achieved the same 28-day strength as the 0.25 w/b mix. Because fly ash reacts more slowly than metakaolin, this late-age strength gain is likely due to later pozzolanic reaction of the fly ash.[56,57] It can be inferred, then, that at these very low w/b ratios there is a proportion of fly ash that is unreacted and instead serves as an inert filler material.

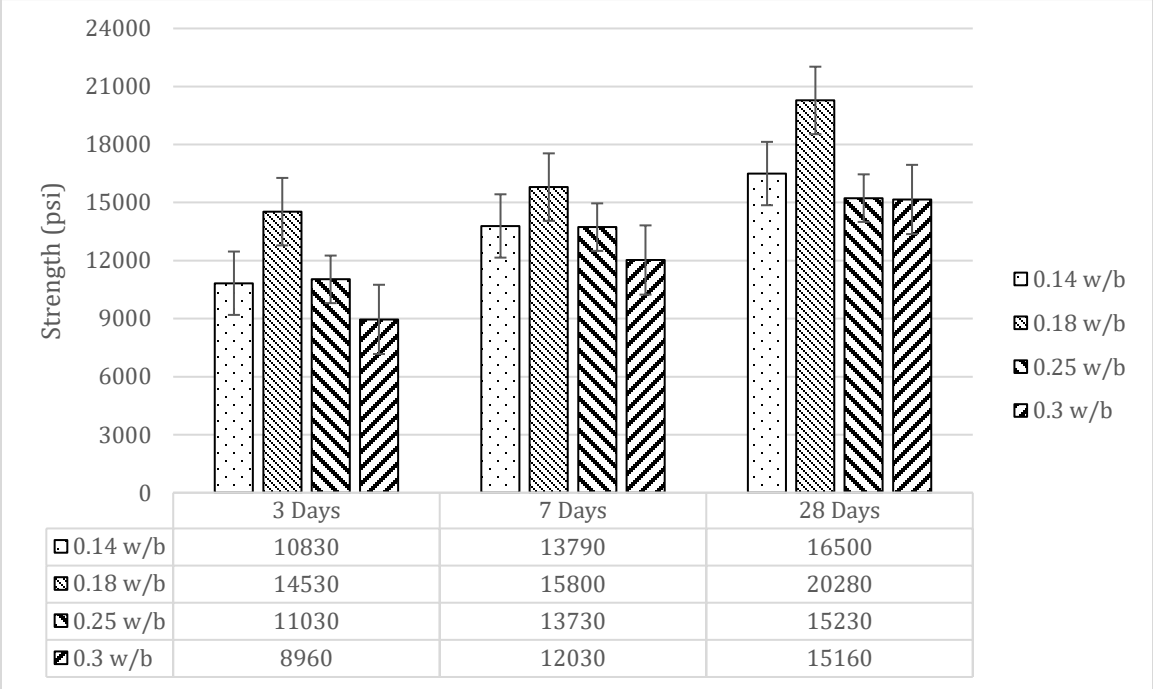

	3 Days	7 Days	28 Days
0.14 w/b	10830	13790	16500
0.18 w/b	14530	15800	20280
0.25 w/b	11030	13730	15230
0.3 w/b	8960	12030	15160

Figure 27. Graph. Effects w/b ratio on compressive strength.

Table 11. GT Baseline mix constituents.

Material	Quantity
Type I Portland Cement	1248 lb/yd^3
Class F Fly Ash	387 lb/yd^3
Metakaolin	100 lb/yd^3
Masonry Sand	1997 lb/yd^3
Superplasticizer (BASF 7920)	8.64 L/yd^3
Water/Binder: 0.18	

Supplementary Cementitious Material Content and Type

Following the water/binder trials, the supplementary cementitious material contents in the mix were adjusted to determine their effects on compressive strength. Class C fly ash was substituted 1:1 by weight with class F fly ash in the baseline mixture. This mix was given the name "FA (C)". Additionally, two mixes containing 8% and 10%, with metakaolin replacing less-reactive fly ash, were attempted. Besides the changes in SCM content, all other design variables were held constant. These mixes were called 8MK and 10MK, respectively. These mix designs are shown in Table 12.

Table 12. Alternative SCM composition mix designs.

Material	Quantity		
	FA (C)	*8MK*	*10MK*
Type I Portland Cement	1248 lb/yd^3	1248 lb/yd^3	1248 lb/yd^3
Fly Ash (class)	387 (C) lb/yd^3	348 (F) lb/yd^3	313.2 (F) lb/yd^3
Metakaolin	100 lb/yd^3	139 lb/yd^3	173.5 lb/yd^3
Masonry Sand	1997 lb/yd^3	1997 lb/yd^3	1997 lb/yd^3
Superplasticizer (BASF 7920)	8.64 L/yd^3	9.72 L/yd^3	10.8 L/yd^3
Water/Binder: 0.18			

The results of these tests are shown in Figure 28. From the figure, it can be seen that the 1:1 replacement of class F fly ash with class C fly ash is the only adjustment that still exceeds the 18,000 psi strength target. Strengths fell as the amount of metakaolin in the mix increased. Additionally, expansion of the concrete was observed in the 8% and 10% metakaolin mixes, as shown in Figure 29. This type of expansion could be an issue in accelerated bridge construction where precast members could be pushed out of place by expanding concrete.

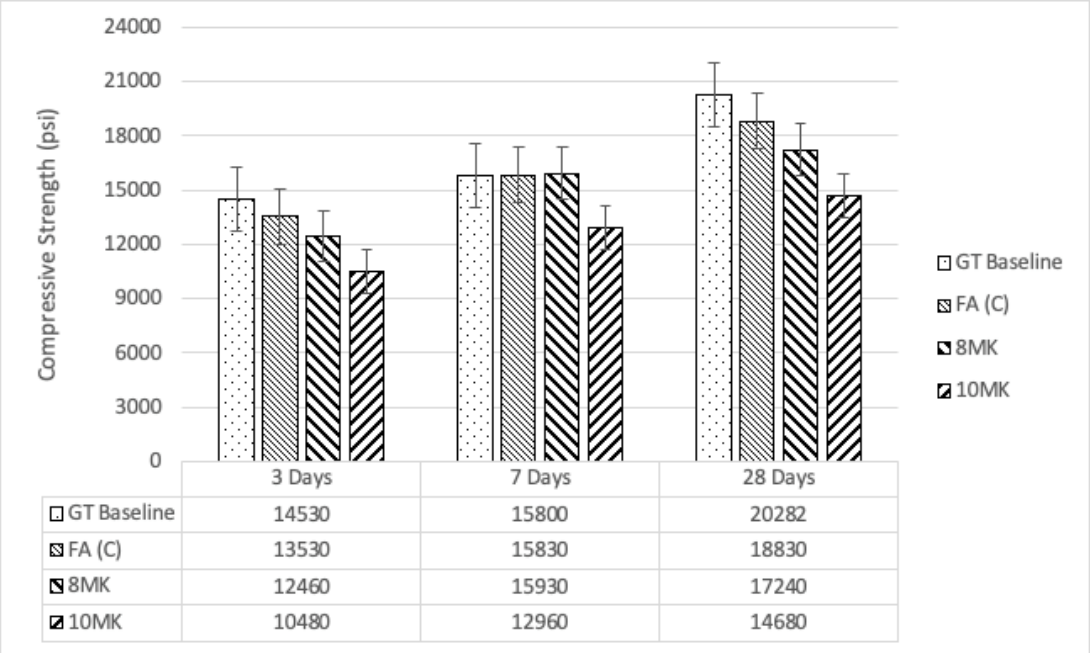

	3 Days	7 Days	28 Days
GT Baseline	14530	15800	20282
FA (C)	13530	15830	18830
8MK	12460	15930	17240
10MK	10480	12960	14680

Figure 28. Graph. Effects of adjusting SCM content on compressive strength.

Figure 29. Photo. Mix 10MK showing expansion above the molds.

Effects of Admixtures

The effects of using a different superplasticizer were also examined, with Sika 2100 being evaluated as a replacement for the BASF MasterGlenium 7920 used in the Baseline mix. This mix was given the name “SP2”. Further trials tested the effects that the addition of 20 ounces per hundred weight of cement (oz/cwt), called ACC-20 and 40 oz/cwt of accelerating admixture had on the compressive strength development of the mix. These mixes were referred to as ACC-20 and ACC-40, respectively. The mix designs and admixture dosages are shown in Table 13.

Table 13. Admixture trial mixes.

Material	**Quantity**		
	SP2	*ACC-20*	*ACC-40*
Type I Portland Cement	1248 lb/yd^3	1248 lb/yd^3	1248 lb/yd^3
Fly Ash (Class F)	387 lb/yd^3	387 lb/yd^3	387 lb/yd^3
Metakaolin	100 lb/yd^3	100 lb/yd^3	100 lb/yd^3
Masonry Sand	1997 lb/yd^3	1997 lb/yd^3	1997 lb/yd^3
Superplasticizer	8.64 L/yd^3 (SIKA 2100)	8.64 L/yd^3 (BASF 7920)	8.64 L/yd^3 (BASF 7920)
Accelerator (BASF Masterset 534)	---	10.26 L/yd^3	20.52 L/yd^3
Water/Binder: 0.18			

The results from these mixes are shown in Figure 30.The effect of different admixtures was compared, to examine sensitivity of the GT Baseline mix to alternative admixtures. Both superplasticizers examined produced virtually identical strengths at the similar dosage levels. Since both are based on polycarboxylate ether chemistry, the similar behavior is expected. However, manufacturers have different proprietary admixture compositions, with the superplasticizer used in Baseline having a 33% solids content while the superplasticizer in SP2 contains 40% solids. The similarity in dosages between these two is encouraging, as it suggests that UHPC can be produced rather robustly using a variety of materials suppliers.

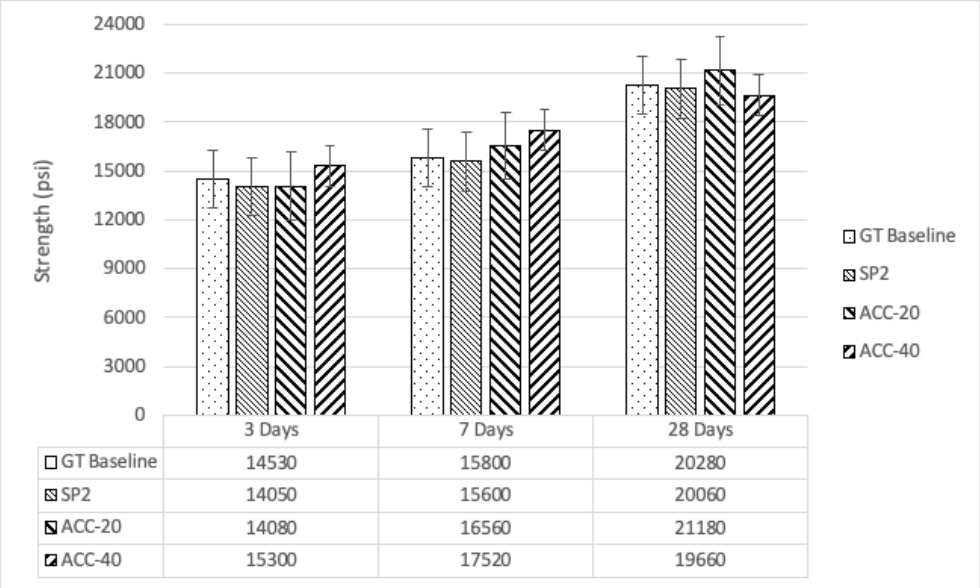

	3 Days	7 Days	28 Days
GT Baseline	14530	15800	20280
SP2	14050	15600	20060
ACC-20	14080	16560	21180
ACC-40	15300	17520	19660

Figure 30. Graph. Effects of admixture on compressive strength.

Cement Sources

Finally, the cement source was varied to observe its effect on the strength and flowability. The Type I cement used in the Baseline had a higher C3S content than the alternative Type I/II trialed, providing insight into how C3S content affects strength development. The Type I/II and Type III versions are practically identical save for their Blaine fineness, providing insight into the effects of fineness on strength development. The results of this study are given in Figure 30. It was found that the mix would exceed 18,000 psi compressive strength objective with any of the chosen cements. The 3-day strength of the Type I/II and Type III mixes was reduced compared to the GT Baseline. Although the 7-Day strength for both the Type I/II and Type I was equal, the Type I performed better across the full range of days. This can be attributed to the higher C3S content of the Type I cement. The Type III cement exhibited higher 3-day strength than the chemically similar Type I/II, demonstrating the effects of cement fineness on early-age strength.

Table 14. Alternative Cement Mix Designs.

Material	Quantity	
	BL I/II	**BL III**
Portland Cement	1248 lb/yd^3 (Type I/II)	1248 lb/yd^3 (Type III)
Class F Fly Ash	387 lb/yd^3	387 lb/yd^3
Metakaolin	100 lb/yd^3	100 lb/yd^3
Masonry Sand	1997 lb/yd^3	1997 lb/yd^3
Superplasticizer (BASF 7920)	8.64 L/yd^3	8.64 L/yd^3
Water/Binder: 0.18		

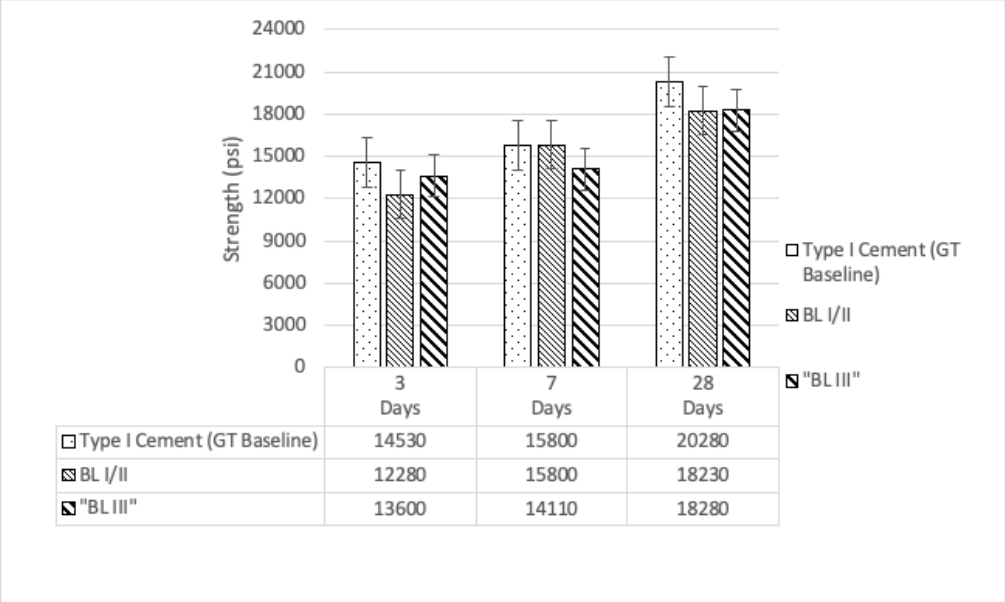

Figure 31. Graph. Effects of Cement type on concrete strength.

PARTICLE PACKING OPTIMIZATION

Following the test matrix approach, the GT Baseline mix was optimized via the modified Andersen and Andreasen model developed by Funk and Dinger. First, the particle size distribution of every cement and supplementary cementitious material was acquired using a laser size analyzer. Gradations for the two sands were obtained through a sieve analysis. The gradation information was imported into EMMA, a software available for free through ELKEM Silica. The GT Baseline mix design was entered, and a distribution

modulus, *q*, value was selected to generate the ideal distribution curve. For this optimization, a *q* value of 0.25 was selected, based upon literature.[58,59] The baseline mix design was compared with the ideal distribution curve. This result is shown in Figure 32, where the red curve represents an ideal distribution and the blue line is the unchanged distribution of the GT Baseline mix.

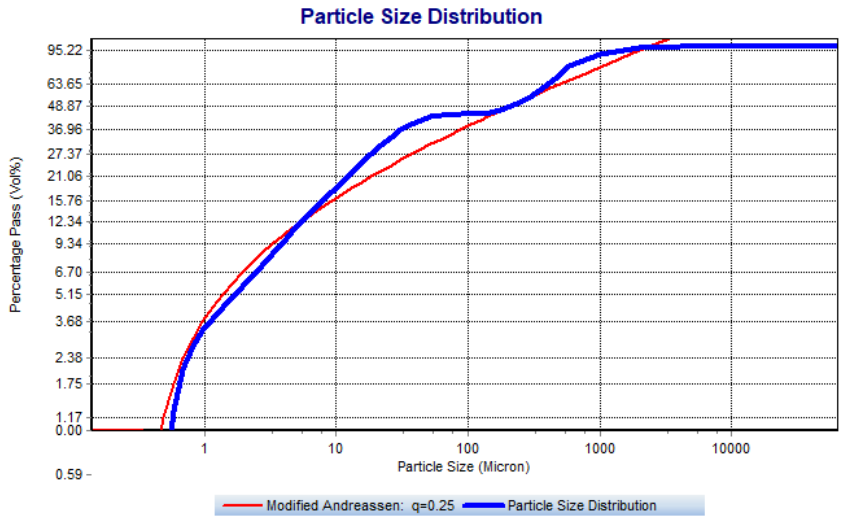

Figure 32. Graph. Particle size distribution of the GT Baseline mix.

The modified Andersen and Andreasen model is an iterative approach, and requires adjustments to be made until the mix's particle size distribution matches the ideal packing curve. After many adjustments, the mix in

Table 15 was found to best represent the ideal packing curve. Alongside the optimized mix shown is the Baseline mix for comparison. The particle size distribution for the optimized mix is shown in Figure 33.

Table 15. The Particle Packing Optimized Baseline Mix.

Material	Quantity	
	Optimized Mix	*GT Baseline*
Type III Portland Cement	826.5 lb/yd^3	1248 lb/yd^3
Class F Fly Ash	357.9 lb/yd^3	387 lb/yd^3
Metakaolin	165.7 lb/yd^3	100 lb/yd^3
Masonry Sand	2381.6 lb/yd^3	1997 lb/yd^3
Superplasticizer	Determined during testing	8.64 L/yd^3
Water/Binder: 0.18		

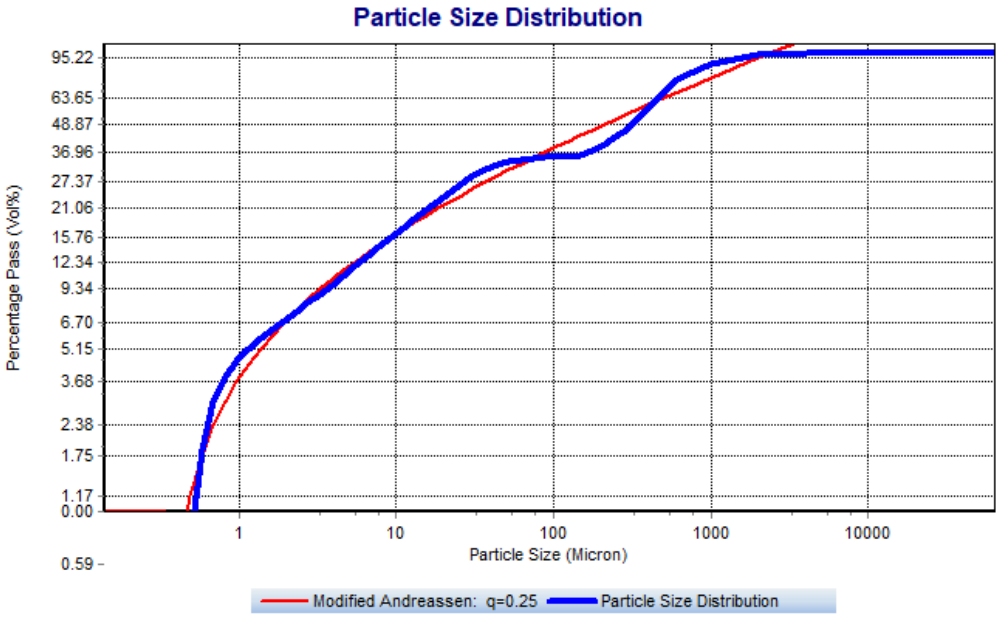

Figure 33. Graph. Particle size distribution of the Optimized Baseline mix.

Over the course of testing, however, the optimized mix had design issues the prevented its consideration as a potential UHPC mix. The mix was attempted at w/b ratios ranging from 0.15 to 0.25, the common range of UHPC w/b ratios, and even up to a 0.30 w/b ratio. In all these cases, workability was very poor and required the addition of superplasticizer to a level that prevented the samples from setting. Because the concrete never set, compression tests were unable to be performed. Further experiments with this mix were discontinued.

SUMMARY

The GT Baseline mix performed the best out of all mixes considered. This mix is self-consolidating, is produced entirely from local materials, and exceeds the 18,000 psi compressive strength requirement. It does also not require expensive accelerators or specialty mixing equipment. For future work, this mix will be referred to as "GT UHPC" and is shown in Table 16. If a project requires a guarantee of higher early strengths, it has also been shown that the addition of 10.26 liters per cubic yard of accelerating admixture may be added to the mixer for little additional cost. This mix will provide the starting point for production batching discussed in the next chapter.

Table 16. GT UHPC mix constituents.

Material	Quantity
Type I Portland Cement	1,248 lb/yd^3
Class F Fly Ash	387 lb/yd^3
Metakaolin	100 lb/yd^3
Masonry Sand	1,997 lb/yd^3
Superplasticizer (BASF 7920)	320 mL/ft^3
Water/Binder: 0.18	

Additionally, it was observed that:

1. Some portion of fly ash remains unreacted in the mix, as can be seen by the w/b targeting trials. The replacement of fly ash with additional metakaolin should be avoided, however, due to issues with expansion that occur at higher metakaolin replacement levels.

2. The addition of accelerating admixtures can provide strengths above 21,000 psi, but higher dosages of accelerator reduce the late-age strength of the mix.

3. In order to ensure that the 18,000 psi compressive strength limit is reached, cement with a high C3S content should be used. While 52% C3S cement (Argos type I/II) was found to provide adequate strengths, a C3S content of 58% or above is recommended.

4. Particle packing optimization led to a sharp decrease in workability, to the mix's ultimate detriment. Packing is an important consideration, but it alone does not determine the suitability of a mix for use as UHPC for accelerated bridge construction.

CHAPTER 4. PRODUCTION-SCALE STUDIES

As discussed in the previous chapter, the GT UHPC mix has been proven to meet compression strength and workability benchmarks in the 10-quart benchtop mixer. However, further experiments were necessary to ensure that the mix's properties remain the same as the batch size is scaled up and a different style of mixer is used. While a benchtop mixer may suffice for laboratory scale testing, placing UHPC in the field requires much larger batches and the use of a high-shear pan mixer, as seen in Figure 34. Furthermore, the workability of the GT UHPC mix has not been established with steel fibers in the mix. This chapter will serve to establish a mixing procedure for field use of GT UHPC and provide further data on compressive strength and workability once fibers have been added to the mix. Additionally, this chapter includes studies as to the effect of sand type on production-scale mixes.

Figure 34. Photo. UHPC being mixed in a high-shear pan mixer in the field.

MIXING STUDIES

The major consideration when changing mixers is the consideration of mixing energy imparted by the mixer.[60] When mixing concrete, energy from the mixer is imparted to

disperse the mix components and hydrate the cement paste. An excess of mixing energy, however, will accelerate the reaction of the cement hydration and cause a loss of workability, as shown in Figure 35.[60,61] Different mixers impart different amounts of energy based on how they operate, but in general the optimal mixing time to achieve high workability and dispersion in UHPC is between 10 and 20 minutes. Mixing times beyond this range can result in porous, less-workable mixes.[62] If the GT UHPC mix is to be used, a proper mixing procedure to reliably produce GT UHPC in this timespan using a high-intensity mixer like those used in the field is necessary.

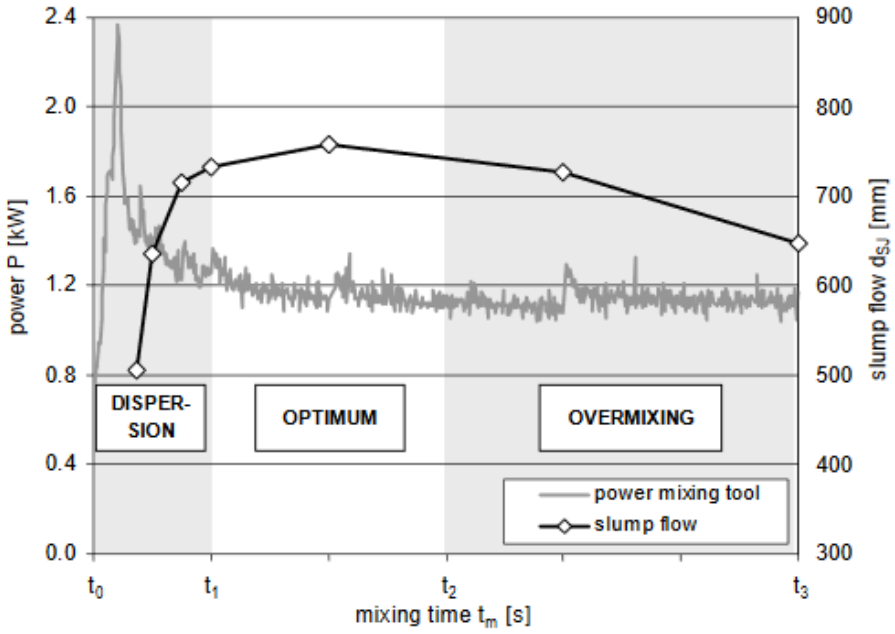

Figure 35. Graph. Effects of overmixing on slump loss.[60]

Mixing Equipment

The mixer that was used for these experiments is an Eirich R08W. This intensive shear pan mixer has an inclined barrel that rotates clockwise. This clockwise rotation carries concrete into a rotor spinning counter-clockwise. A fixed scraper further agitates the

concrete as it moves past the rotor. This mixing action is demonstrated by Figure 36. This style of mixer has been used previously to produce UHPC by Georgia Tech[63], the Army Corps of Engineers[64], and by researchers abroad.[65-68] This track record demonstrates that this mixer is equivalent to other mixers used for UHPC and is suitable for use in developing mixing procedures for the GT UHPC.

Figure 36. Schematic. Mixing action of the Eirich R08W mixer.[65]

Steel Fibers

Steel fibers are a necessary inclusion in UHPC to provide tensile and flexural strength. The addition of steel fibers causes a decrease in concrete workability and good workability is necessary to ensure proper dispersion of the fibers.[51,68-70] Too much workability, however, will cause the fibers to segregate from the mixture.[70] Because the small-scale mix development of GT UHPC did not involve fibers, it is imperative that the effects of fiber addition be observed in a large-scale setting.

The fibers used in this mix are brass-coated steel fibers 13 mm in length and 0.2 mm in diameter. They have a nominal tensile strength of 2,750 MPa (398 ksi), a Young's

modulus of 200,000 MPa (29,000 ksi), and are produced in Georgia (Bekaert; Rome, Georgia).[71] This size and brand of fiber is very common in UHPC production as these fibers are used in every type of UHPC that is commercially available and their short length relative to other fibers allows for improved performance when dosed as a percentage of the mix volume.[72-74]

Mixing Procedure Trials

In previous work at Georgia Tech, the rotor speed on the mixer was limited to 35 rotations per minute (RPM) for the duration of the mix.[63] Other research has shown, however, that a hybrid mixing approach that combines both high and low speed mixing speeds can help reduce overmixing and decrease mixing time.[60] To determine which mixing procedure is optimal, three different mixing procedures were tested for use with the GT UHPC. The first was mixed entirely at 250 RPM, which will be referred to as "GT-1". Another mix, "GT-2", was mixed entirely at 35 RPM. The third mix was mixed in two stages- the dry materials were mixed at 250 RPM and mixing speed was reduced to 35 RPM upon the addition of water. This mix was referred to as "GT-3". The changes to mix procedure are the only changes made to these mixes, compositionally they are all identical GT UHPC mix. The GT UHPC mix design is shown again in Table 17 in the quantities necessary to batch one cubic foot of concrete and steel fibers. The complete mix procedure for each mix procedure and the associated nomenclature is given in Table 18.

Table 17. GT UHPC mix design used for GT-1, GT-2, and GT-3.

Material	Quantity
Type I Portland Cement	46.20 lb/ft^3
Class F Fly Ash	14.33 lb/ft^3
Metakaolin	3.70 lb/ft^3
Masonry Sand	73.96 lb/ft^3
Superplasticizer (BASF 7920)	320 mL/ft^3
Steel Fibers	9.80 lb/ft^3
Water/Binder: 0.18	

Table 18. Large scale mixing procedures.

Mix Procedure	Mixing Speed (RPM)		
	GT-1	GT-2	GT-3
Mix sand and metakaolin for 2 minutes	250	35	250
Add fly ash and cement, mix for 1 minute	250	35	250
Add water over the course of 30 seconds and let mix for 30 seconds	250	35	35
Add HRWR and mix for 8 minutes	250	35	35
Add half of the steel fibers and mix for 2 minutes	250	35	35
Add remaining steel fibers and mix for 2 minutes	250	35	35

Mixing Procedure Observations

The GT-1 mixing process proved to be very ineffective. As the UHPC became cohesive, the high speed of the rotor began to rebuff the concrete away rather than mix it. As a result, the mixture remained in a stiff and unworkable ring. In an effort to cast specimens, the mix time was extended and additional superplasticizer was added. In total, GT-1 was mixed for 30 minutes and contained 450 mL of superplasticizer, up from the 320 mL initially planned. GT-1 achieved self-consolidating flow with an 8.25-in. flow on the flow plate.

The mixing process for GT-2 and GT-3 was much better. The lower rotor speed allowed concrete to reach the blades of the rotor and increased the agitation of the concrete. GT-2 achieved a 9-in. flow, while GT-3 achieved an 8 ¾-in. flow.

Compression Test Results

As with the laboratory-scale experiments, each mix was evaluated based on its compression strength and flow measurements. In a departure from the laboratory scale tests, however, the compression specimens for the large-scale test were cast in 10 cm x 10 cm x 10 cm (3.93 in. x 3.93 in. x 3.93 in.) cubic molds. Additional discussion on the testing protocol is provided in Chapter 5. The compression test results for each mixing procedure are given in Figure 37. GT-2 failed to reach the 14,000 psi compressive strength benchmark by 7 days, achieving only 10,000 psi compressive strength at that age. GT-3 was the only mixing procedure that reached both the 14,000 psi 3-day strength benchmark and the 18,000 psi 28-day strength target.

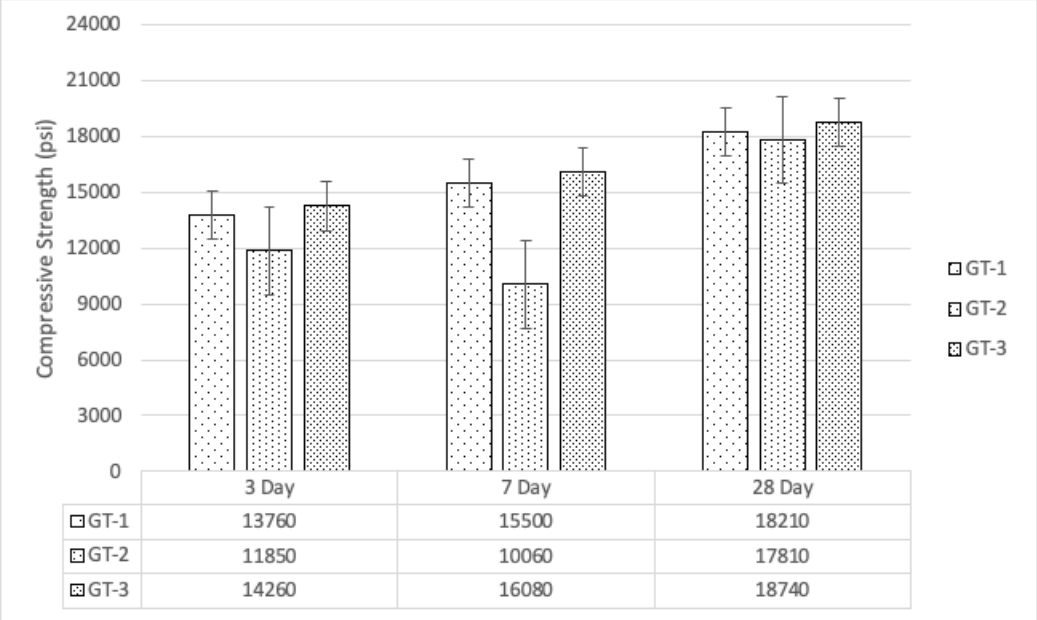

	3 Day	7 Day	28 Day
GT-1	13760	15500	18210
GT-2	11850	10060	17810
GT-3	14260	16080	18740

Figure 37. Graph. Compressive strength for varying mix processes.

The difference in strength values between the GT-2 procedure and the others is believed to be related to the dispersion of the metakaolin in the mix. Both GT-1 and GT-3 blended the sand and metakaolin at high speeds, imparting more energy to break apart agglomerations of metakaolin. This dispersion of metakaolin has been shown to increase its pozzolanic effects by exposing a higher surface area of metakaolin to the mix.[75] Because it produces a mix that meets strength targets, it does not require additional superplasticizer, and stays within the preferred mixing timeframe of 10 to 20 minutes GT-3 mixing process continued for future experiments.

Summary

From the experiments, it was observed that the inclusion of steel fibers did not affect the ability of the UHPC to reach a self-consolidating state at the dosage of superplasticizer determined by the small-scale mixing trials. Both GT-2 and GT-3 mixing procedures produced self-consolidating UHPC with the inclusion of fibers.

The workability issues, extended mixing time, and need for additional superplasticizer eliminated GT-1 as a feasible mixing process. Despite the extended mixing time and increased dosage of superplasticizer, however, the early-age strength of GT-1 was higher than GT-2. In fact, GT-2 failed to reach the 14,000 psi compressive strength benchmark by 7 days, achieving only 10,000 psi compressive strength at that age. GT-3 was the only mixing procedure that reached both the 14,000 psi 3-day strength benchmark and the 18,000 psi 28-day strength target.

The difference in strength values between the GT-2 procedure and the others is believed to be related to the dispersion of the metakaolin in the mix. Both GT-1 and GT-3 blended

the sand and metakaolin at high speeds, imparting more energy to break apart agglomerations of metakaolin. This dispersion of metakaolin has been shown to increase its pozzolanic effects by exposing a higher surface area of metakaolin to the mix.[75] Because it produces a mix that meets strength targets, does not require additional superplasticizer, and stays within the preferred mixing timeframe of 10 to 20 minutes it is recommended that the GT-3 mixing process be adopted for the production of GT UHPC.

EFFECTS OF ALTERNATE SAND

Once a proper mixing procedure had been established for the GT UHPC, different sources of sand from around the state were acquired to test the suitability of alternate aggregate sources. The baseline GT UHPC uses masonry sand from southern Georgia, so masonry sands from both northern (River Sand Inc, Buford, Georgia) and central (Butler Sand, Butler, Georgia) Georgia were acquired to evaluate their suitability for use in UHPC. Additionally, a coarser river sand for use in general construction was acquired from the same southern quarry as the southern masonry sand. The particle size distributions and material data of these sands are shown in Table 19 and Figure 38. These sands were compared to the previously used south Georgia masonry sand (GT UHPC). These mixes were given names corresponding to their sands. “GT-C”, “GT-N”, and “GT-RS” corresponded with the central masonry sand, the northern masonry sand, and the southern river sand, respectively. Additionally, a version of the GT-RS mix was performed in which silica fume replaced the metakaolin to see how the mix would perform without metakaolin. This mix design is given in Table 20.

Table 19. Alternative sand data.

Sieve Size	Percent Passing (%)		
	Northern Masonry Sand	Central Masonry Sand	South Georgia River Sand
#4	100	100	99.39
#8	100	99.97	95.24
#16	98.92	99.05	81.8
#30	84.55	87.11	49.58
#50	33.71	41.85	13.3
#100	3.93	6.7	1.19
#200	0.23	0.21	0.2
Fineness Modulus	**1.79**	**1.65**	**2.59**
Specific Gravity (ASTM C128)	**2.4**	**2.63**	**2.65**
Absorption Capacity (ASTM C128)	**1.1%**	**0.93%**	**0.53%**

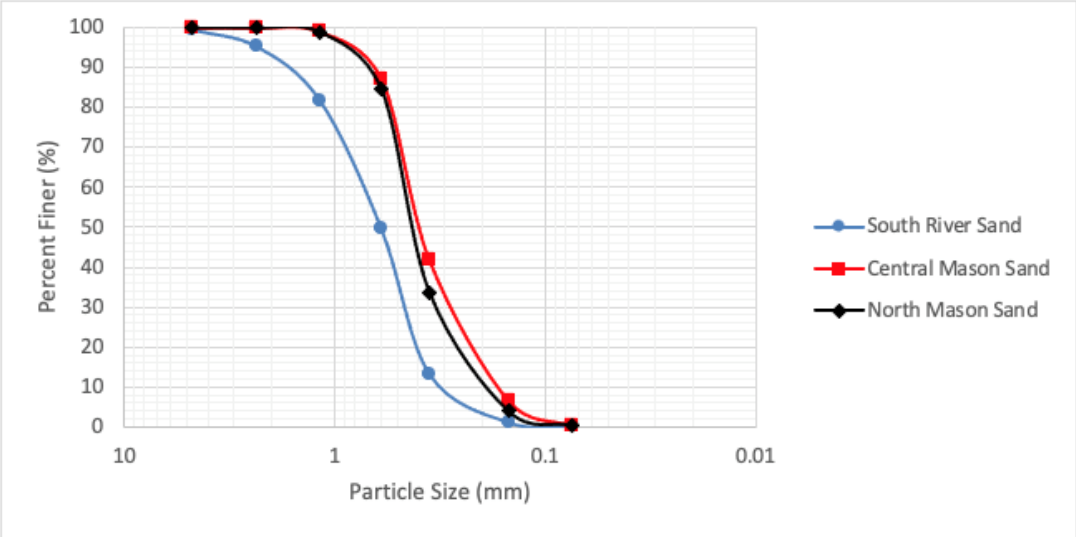

Figure 38. Graph. Gradation curves for alternative sands.

Table 20. The GT-RS-SF Mix.

Material	Quantity
Type I Portland Cement	1,248 lb/yd^3
Class F Fly Ash	387 lb/yd^3
Silica Fume	100 lb/yd^3
South Georgia River Sand	1,997 lb/yd^3
Superplasticizer (BASF 7920)	320 mL/ft^3
Water/Binder: 0.18	

Compression Test Results

The compression results of these tests are shown in Figure 39 and mix data is shown in Table 21.

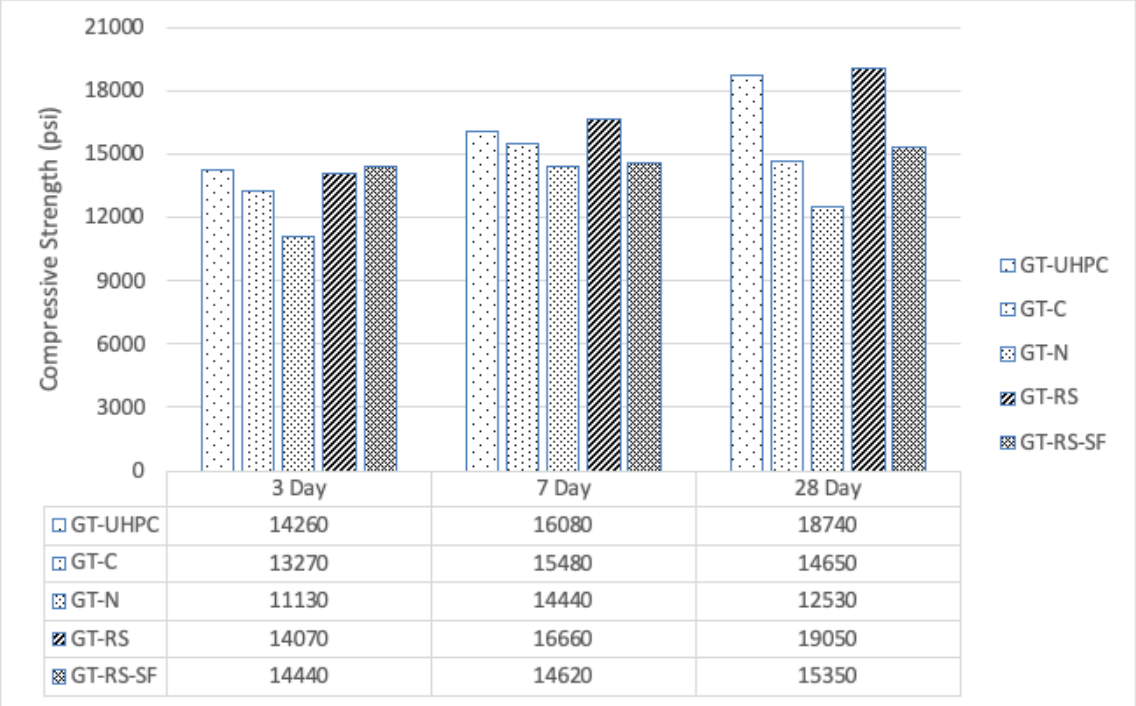

	3 Day	7 Day	28 Day
GT-UHPC	14260	16080	18740
GT-C	13270	15480	14650
GT-N	11130	14440	12530
GT-RS	14070	16660	19050
GT-RS-SF	14440	14620	15350

Figure 39. Graph. Compression data for sand trials.

Table 21. Mix data from sand trials.

	Mix Name			
	GT-C	GT-N	GT-RS	GT-RS-SF
Cement (lb/yd^3)	1248	1248	1248	1248
Fly Ash (lb/yd^3)	387	387	387	387
Metakaolin (lb/yd^3)	100	100	100	0
Silica Fume (lb/yd^3)	0	0	0	100
Sand (lb/yd^3)	1997 (Central Masonry Sand)	1997 (Northern Masonry Sand)	1997 (Southern River Sand)	1997 (Southern River Sand)
Water (lb/yd^3)	312.25	312.25	312.25	312.25
w/cm	0.25	0.25	0.25	0.25
w/b	0.18	0.18	0.18	0.18
Superplasticizer (L/yd^3)	13.5	20.52	8.91	9.99
Mix Time	24 Minutes	32 Minutes	16 Minutes	19 Minutes
Flow	7 3/4"	6"	8 1/2"	7"

Summary

Of the sands tested, the North Georgia masonry sand performed the worst when used in the GT UHPC mix. The GT-N mix required an extended mixing period and the addition of 137.5% more superplasticizer than was initially planned for. Despite this high amount of superplasticizer, the mix still only achieved 6 inches of flow and had low workability. The compressive strengths for the mix were also the lowest of all mixes tested, with no strength development between the 7 and 28-day compressive tests. The northern masonry sand was also the poorest quality sand evaluated. It contained many platy minerals and organic inclusions that were visible to the naked eye.

The Central Georgia Masonry sand performed slightly better than the northern sand but was still unsatisfactory. The GT-C mix required less additional mixing time and required only a 56% increase in superplasticizer dosage over the GT UHPC specification. This sand also provided a more workable mix, achieving a 7 ¾-in. flow result. However, compressive strengths still fell short of the 18,000 psi compressive strength requirement

and this mix displayed the same lack of strength development between 7 and 28 days as the GT-N Mix.

The South Georgia river sand had the highest performance of all sands tested. The total mix time was identical to the GT-UHPC at 16 minutes. The mix was self-consolidating with an 8 ½-in. flow and the GT-RS mix only required an additional 3% dosage of superplasticizer over the GT UHPC specification. The GT-RS mix was also the only alternative mix design tested that met the 14,000 psi 3-day strength and 18,000 psi 18-day strength targets. The GT-RS-SF mix variant had high early age, meeting the 14,000 psi 3-day strength. However, it showed very little strength gain at 7 and 28 days and required additional mixing time and superplasticizer over the regular GT-RS mix. The results of the GT-RS-SF mix indicate that metakaolin provides an advantage over silica fume in the GT UHPC mix.

The sieve analysis gradations for the sands tested are shown in

Table 22. The highest performing sands - and indeed the only sands that could be used to meet strength requirements - were the masonry and river sands from Southern Georgia. It can be seen in

Table 22 that these sands are very clean, with a very low content of fine sand. The southern masonry sand only contains 1.53% material finer than a #100 sieve, while the river sand contains only 1.19% material finer than a #100 sieve. Additionally, both the

central and northern masonry sands contain roughly double the amount of material that passes a #50 sieve than the southern masonry sand. These results indicate that having a fine sand only serves as a detriment to GT UHPC.

Table 22. Gradation data for all sands.

Sieve Size	Percent Passing (%)			
	Northern Masonry Sand	Central Masonry Sand	South Georgia River Sand	South Masonry Sand
#4	100	100	99.39	100
#8	100	99.97	95.24	99.99
#16	98.92	99.05	81.8	95.08
#30	84.55	87.11	49.58	63.98
#50	33.71	41.85	13.3	17.99
#100	3.93	6.7	1.19	1.53
#200	0.23	0.21	0.2	0.29
Fineness Modulus	**1.79**	**1.65**	**2.59**	**2.21**
Specific Gravity (ASTM C128)	**2.4**	**2.63**	**2.65**	**2.65**
Absorption Capacity (ASTM C128)	**1.1%**	**0.93%**	**0.53%**	**0.93**

CHAPTER 5. PROTOCOL FOR MATERIAL MIXING AND MATERIAL TESTING

Using the results from the laboratory and production studies, additional production runs were conducted to prepare for the structural evaluation. To accurately compare the final material batches, a standard protocol for mixing and mechanical testing was developed.

MIXING PROCEDURE

An intensive mixer manufactured by Eirich USA was used to make the majority of the UHPC in this study. The model of the mixer is R08W, which has a capacity of 75 L (2.65 ft^3) and 120 kg (265 lbs).[76] Figure 40 illustrates the mixing method and turning geometry of R08W. The rotor and mixing pan rotate in opposite directions allowing materials to mix thoroughly. The fixed scraper also agitates the concrete mix. The combination of high rotating speeds and geometry produces optimum homogenization of different materials.[77] Figure 41 gives a photo of the R08W used to make UHPC in this study.

Figure 40. Photo. UHPC being mixed with R08W.

Figure 41. Photo. Eirich R08W used to make all UHPC in this investigation.

To achieve optimum workability and consistency in the UHPC mix, several procedures were implemented. Masonry sand, metakaolin, cement, and fly ash are initially dry mixed for a total of 10 minutes to break up any agglomerations and ensure that materials are evenly dispersed. It has been observed that using metakaolin drives up the temperature of the mix to a noticeable degree. A higher temperature of the mix can decrease the workability of UHPC. To offset the increase in temperature, at least half of the water was replaced with ice cubes. The step-by-step procedure is:

1. Add masonry sand and metakaolin in the mixer. Mix at ~250 rpm for 5 minutes.
2. Add cement and fly ash. Mix at ~250 rpm for 5 minutes.
3. Take 3/4 of HRWR and add to 0.175 of w/cm worth of water. Stir thoroughly.

4. Keep running the mixer at ~250 rpm. Gradually pour the water-HRWR solution into the mix over the course of 1 to 2 minutes.
5. After all water-HRWR solution has been added, increase the speed to ~400 rpm. Mix for 8 minutes.
6. Pour the remaining 1/4 of HRWR into the remaining 0.005 w/cm worth of water.
7. Gradually pour the remaining water-HRWR into the mixer in 1 minute.
8. Decrease the speed to ~180 rpm. Mix for 5 minutes.
9. Perform flow table test per ASTM C1437 with exceptions outlined in ASTM C1856.
10. Keep the mixer running at ~60 rpm while performing flow test.
11. Once desirable flow diameter is confirmed, gradually add steel fibers to the mix within 1 to 2 minutes. Mix at ~180 rpm for 5 minutes.
12. Cast UHPC.

The mixing procedure was developed through multiple trial pours in the laboratory. Satisfactory workability is achieved when there is a delayed addition of water and HRWR (steps 6 and 7). If all the batch water and HRWR are added at the very beginning of wet mixing, the UHPC has a state of poor workability. The mix also sets up relatively quickly in the mixer and becomes extremely difficult to place into molds. It has been observed that when UHPC is allowed to sit in the mixer for longer than 10 minutes without agitation, a dry skin forms on the surface that makes the mix more difficult to maneuver. Although this dry skin is easy to break apart manually, it is recommended to agitate the mix using the mixer to avoid difficulties in placing fresh UHPC. In the above procedure, step 10 was implemented to address this issue. This is especially prescient when casting UHPC in multiple layers since the dry skin can potentially create an interface between layers and reduce the randomness of steel fiber orientation. It is

important to determine the flow diameter of freshly mixed UHPC, step 9, prior to adding steel fibers, step 11. When fibers are added without achieving the desired flow diameter of UHPC, the mix stiffens and loses significant workability. This can result in poor quality of casting as shown in Figure 42.

Figure 42. Photo. 100 mm cube specimen. The shape is distorted due to poor workability of UHPC.

MECHANICAL TESTING

Compressive Strength Test Procedure

During the development of a non-proprietary mix design, UHPC specimens used to test for compressive strength were cast into 100 mm (3.94 in.) cubic molds. 3 in. by 6 in. cylinders were also cast along with the 100 mm cubes during construction of structural test specimens which will be discussed in detail in Chapter 5. One cubic foot of UHPC was made per batch during the development of non-proprietary UHPC mix design. The dimensions of cube and cylinder specimens and the load rate at which they were tested

conform to specifications in British Standards (BS) EN-12390 and ASTM C39, respectively. To perform the compressive strength tests, smooth testing surfaces are required. Unlike cylindrical molds, cubic molds allow the specimens to have five smooth surfaces. Grinding down an uneven surface for testing was not necessary, which helped expedite the process. Figure 43 shows the molds used to make compressive test specimens. Cube and cylinder specimens that are ready for testing are shown in Figure 44 and Figure 45, respectively. All compressive strength test specimens were placed in a static servo-hydraulic SATEC compression frame that has a capacity of 800 kips. Testing was displacement-controlled, and displacement was increased steadily by the SATEC until automatically stopped, when the specimen lost further load-carrying capacity. The maximum load is recorded for every specimen.

Figure 43. Photo. 100 mm cube molds used for casting UHPC.

Figure 44. Photo. 100 mm UHPC cube specimen ready for testing.

Figure 45. Photo. 3 in. by 6 in. UHPC cylinder ready for testing.

For every batch of UHPC during the mix design development and structural specimen construction, nine cubic specimens were cast and screeded before being covered with plastic wrap to prevent moisture loss. Screeding UHPC is not always recommended nor manageable, especially in a larger-scale cast. However, screeding was done in this investigation to ease the preparation process for testing. All specimens were removed from their molds 24 hours after being cast. They were subsequently stored in a fog room at 73˚F and allowed to cure until testing. There was no thermal treatment of specimens or any other notable curing regime. Compressive tests were performed 3, 7, and 28 days after casting. Three cube specimens and three cylinder specimens were tested on each test day. The ends of cylinder specimens were ground with an end-grinder, shown in Figure 46, to ensure smooth testing surfaces. For cube specimens, the testing procedure adhered to EN-12390-3. The load rate specified in EN- 12390-3 is between 0.2 MPa/s (29 psi/s) and 1.0 MPa/s (145 psi/s).[78] The average value, 0.6 MPa/s (87 psi/s), was chosen for all compressive strength tests of cubic specimens in this study. For cylinder specimens, the load rate of 37 psi/s specified in ASTM C39 was modified to 150 psi/s per Graybeal's previous study.[3]

Figure 46. Photo. Grinding a 3 in. by 6 in. cylinder to ensure smooth testing surface.

Flexural Test Procedure

Beam specimens were cast to evaluate the flexural performance of non- proprietary UHPC. These specimens were cast simultaneously with the cube and cylinder specimens. Specimens were covered with plastic wrap after casting and were demolded 24 hours later. They were then placed in a fog room at 73˚F until testing at 28 days after being cast. Two dimensions of beams were used: 2 in. by 2 in. by 17 in. and 3 in. by 3 in. by 12 in. Three specimens were cast for each dimension. Different dimensions were used to evaluate the consistency in flexural performance. Figure 47 shows the beam molds that were used to cast specimens. A four- point bending test configuration was followed per ASTM C78 and C1609 as shown in Figure 48. Beam specimens were placed on a test fixture with an adjustable support span. One of the two supports of the bottom fixture was allowed to slide laterally as the specimen was loaded, acting as a roller support. An LVDT is used to measure the midspan displacement throughout the test. A load cell with a capacity of 10 kips was used to measure the load as the specimen was loaded at 0.01

in/min. The load and midspan displacement data were acquired using National Instrument's LabVIEW, a data acquisition program, at a rate of 3 Hz.

Figure 47. Photo. 3 in. by 3 in. by 12 in. molds (left) and 2 in. by 2 in. by 17 in. molds (right).

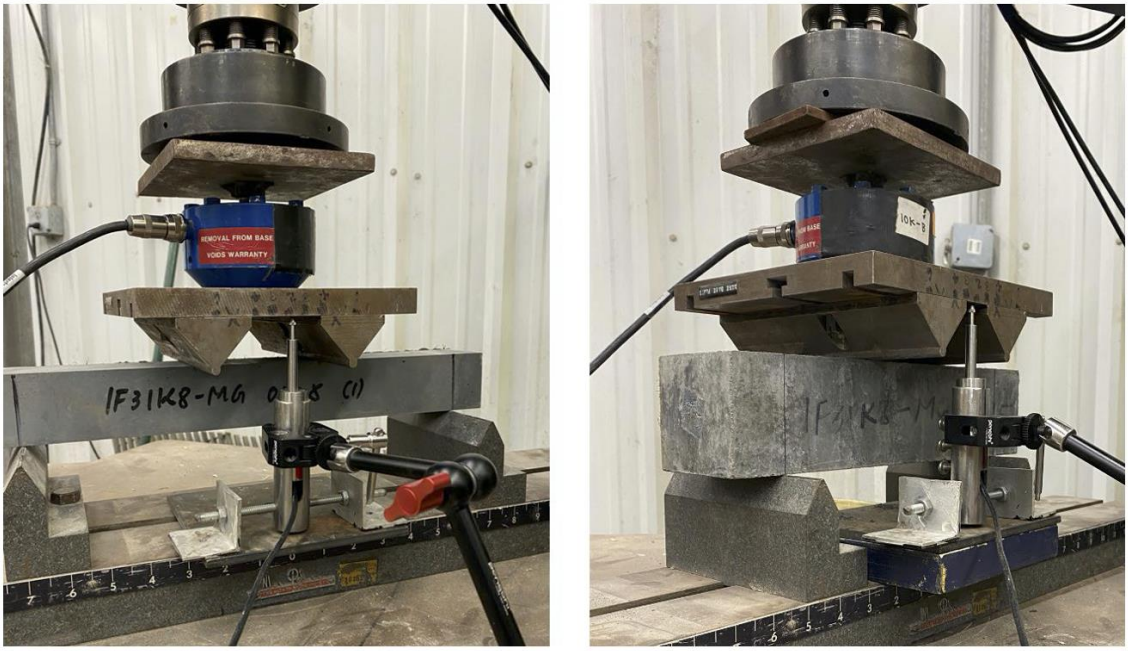

Figure 48. 2 in. by 2 in. by 17 in. beam (left) and 3 in. by 3 in. by 12 in. beam (right) during testing.

CHAPTER 6. GDOT NON-PROPRIETARY MIX EVALUATION

The non-proprietary UHPC mix design for GDOT has a target compressive strength of at least 18,000 psi at 28 days with sufficient tensile strength and ductility. The high compressive strength and tensile capacity of UHPC will allow for smaller and simpler joint connections between structural elements in ABC. The materials used to make this UHPC should also be easily acquired within the state of Georgia. This chapter evaluates the material and mechanical properties of the two most promising UHPC mixes using the procedures outlined in Chapter 5.

MIX NOMENCLATURE

Table 23 shows the material composition of a non-proprietary UHPC developed in this study. For comparison, Table 24 shows one of several non-proprietary mixes from a previous study by Graybeal. The mix design in Table 24 is chosen for comparison amongst others because of its high average 28-day compressive strength of 29 ksi and identical amount of cement used in Graybeal's non-proprietary mix.[79] To differentiate the two mix designs, each mix is given a specific nomenclature. The non-proprietary mix in Table 23 is referred to as 1F31K8. The mix with silica fume is referred to as 1F24Sf25. Figure 49 explains the nomenclature in detail. Table 9 summarizes the materials and their respective suppliers.

Table 23. Material composition of GT UHPC (1F31K8).

Materials	Weight (pcy)	Ratio per Cement Weight
Type I Portland Cement	1248	1
Class F Fly ash	387	0.31
Metakaolin	100	0.08
Masonry sand	1997	1.60
HRWR	25.7	0.02
Water	303	0.24
Steel fibers	264.6	0.21

Table 24. Graybeal's non-proprietary mix (1F24Sf25).[79]

Materials	Weight (pcy)	Ratio per Cement Weight
White cement	1248	1
Fly ash	303	0.24
Silica fume	312	0.25
Fine aggregate	1871	1.5
HRWR	45	0.036
Water	287	0.23

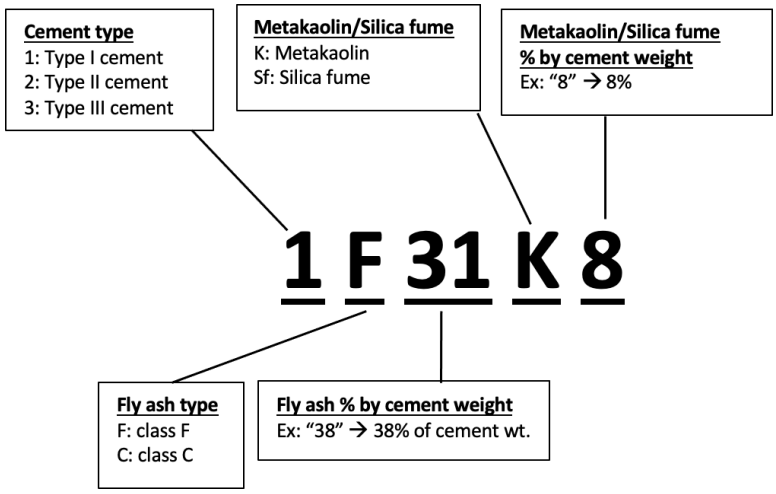

Figure 49. Schematic. Explanation of nomenclature used to differentiate mixes.

Table 25. Materials and their respective suppliers for 1F31K8.

Materials	Suppliers
Type I Portland Cement	LaFarge-Holcim
Class F Fly Ash	Boral Resources
Metakaolin	BASF Kaolin
Masonry sand	Vulcan Materials
HRWR	MBCC Master Builders Solutions
Steel Fibers	Bekaert

The HRWR used in the non-proprietary mix is MasterGlenium® 7920. It is a polycarboxylate ether HRWR that conforms to ASTM C494 requirements.[31] Steel fibers marketed under the name Dramix® were procured from Bekaert. These fibers have nominal length of 13 mm (0.5 in.), diameter of 0.2 mm (0.008 in.), and tensile capacity of 2,600 MPa (377 ksi).[32] Masonry sand used in the mix has all particles passing the No. 4 sieve and a fineness modulus of 1.59. The absorption capacity and specific gravity of the masonry sand is 0.51% and 2.58, respectively.

Figure 50 shows the sieve analysis results for the masonry sand procured from Vulcan Materials' quarry. Details of the sieve analysis of masonry sand used in 1F31K8 are given in Appendix A.

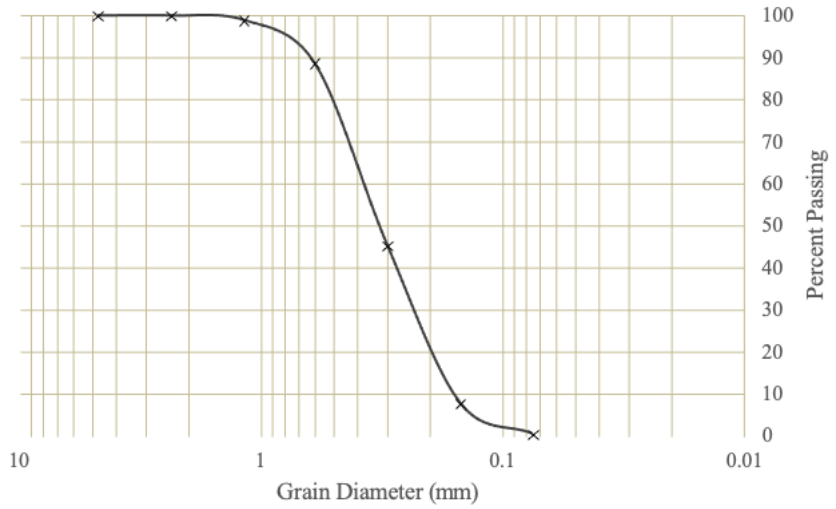

Figure 50. Graph. Sieve analysis result of masonry sand used in 1F31K8.

INITIAL OBSERVATIONS OF UHPC

Observations of 1F31K8

As mentioned previously, it is important to achieve satisfactory workability of UHPC prior to adding fibers. The desired flow diameter of 1F31K8 is at least 9 in., adhering to procedures listed in ASTM C1437 with modifications outlined in ASTM C1856.[40] This value is chosen based on numerous observations of UHPC mixtures that exhibited either poor workability or too much fluidity. A flow test of UHPC with a diameter of 7-5/8 in. and relatively poor workability is shown in Figure 51. An acceptable flow diameter of approximately 9-1/4 in. in one direction is shown in Figure 52. Increasing the w/cm ratio of the mix design can help increase the workability of UHPC. However, it should be noted that increasing w/cm ratio can lead to segregation of steel fibers. This can render the UHPC ineffective, as it reduces the randomness of fiber distribution.

Figure 51. Photo. Flow diameter of 7-5/8 in. indicative of poor workability.

Figure 52. Photo. Flow diameter of 9-1/4 in. indicative of good workability.

It is noteworthy to mention that a 1:1 replacement of silica fume with metakaolin did not result in a successful batch of UHPC. Rougeau and Borys investigated use of ultra-fine particles other than silica fume in UHPC mixes. Using metakaolin and pulverized fly ash in UHPC required a higher dosage of superplasticizer and water to achieve the same workability as UHPC using silica fume .[80] Although higher amounts of water can improve the workability of UHPC, it will compromise the strength and quality of the final product. These observations align with those made in this investigation. During the development of 1F31K8, a higher metakaolin to cement ratio resulted in poor workability of UHPC, it will compromise the strength and quality of the final product. These observations align with those made in this investigation. During the development of 1F31K8, a higher metakaolin to cement ratio resulted in poor workability in several batches. Figure 53 shows a mix with 0.12 of metakaolin-to-cement ratio that became relatively solid and lumpy prior to the flow test. Figure 54 shows a flow diameter of 4-3/8 in. of the UHPC mix. The mix had very poor workability and did not behave like a self-consolidating concrete.

Figure 53. Photo. Indication of poor workability of a UHPC batch with 0.12 metakaolin-to- cement ratio.

Figure 54. Photo. Flow diameter of 4-3/8 in. indicates poor workability of the above mix.

Observations of 1F24Sf25

To directly compare the mix design developed for GDOT's use, the aforementioned 1F24Sf25 was also mixed and tested during this investigation. The main difference is the

use of silica fume instead of metakaolin. Silica fume used in this investigation was supplied by Elkem Materials. While mixing 1F24Sf25, there was no significant rise in temperature of the mix unlike in the case of 1F31K8. The reason for this may be due to the absence of metakaolin in 1F24Sf25. Figure 55 shows a flow table test for 1F24Sf25. The average flow diameter was 8-5/8 in. Although the flow diameter is lower than the desired diameter for 1F31K8, 1F24Sf25 displayed satisfactory workability for a prolonged period.

Figure 55. Photo. Flow test of 1F24Sf25.

MECHANICAL PROPERTIES

Compressive Strength During Development

Compressive tests were conducted using the protocol in the previous chapter. One common failure mode was observed across every cube specimen. The steel fibers in the mix design of UHPC allowed specimens to fail in a ductile mode. Figure 56 shows the

failure mode of cube specimens. The cubic shape of each specimen is somewhat retained due to the steel fibers. The surface cracks that are shown in Figure 56 reveal how fibers are holding onto the concrete and prevent it from failing abruptly. Delamination of surfaces is a common observation made across all the cube specimens that failed in compression.

Figure 56. Photo. Failure mode of 100 mm UHPC cube specimens after compressive strength test.

The average compressive strength test results across nine batches of 1F31K8 during development are shown in Table 26. Average compressive test results for two batches of 1F24Sf25 are shown in Table 27. A bar graph comparing the average strength results between the two mixes is shown in Figure 57. All test compression test results are summarized in Appendix B.

Table 26. Average compressive strength of 1F31K8 during development.

Days cured	Average Strength (ksi)	Standard deviation (ksi)	COV (%)
3	14.35	0.79	5.48
7	16.14	0.68	4.24
28	18.55	1.11	5.96

Table 27. Compressive test results for 1F24Sf25.

Days cured	Average Strength (ksi)	Standard deviation (ksi)	COV (%)
3	12.86	0.19	1.50
7	14.10	0.81	5.72
28	16.74	0.94	5.59

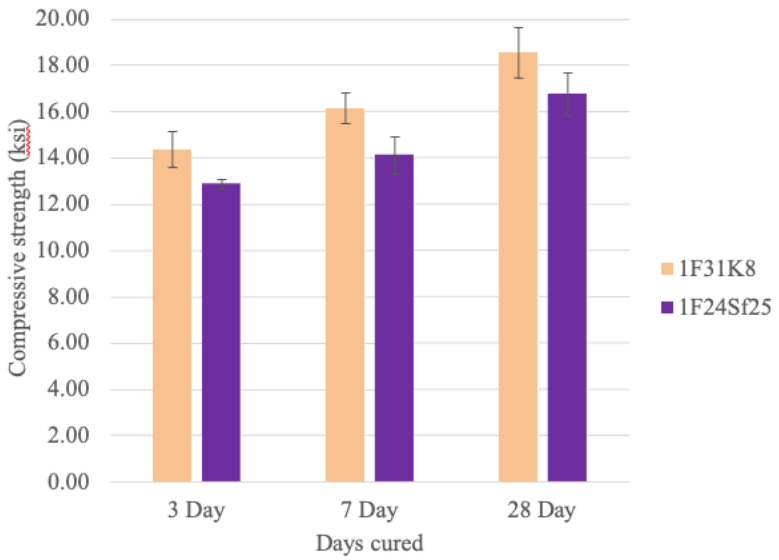

Figure 57. Graph. Average compressive strength comparing 1F31K8 and 1F24Sf25.

It can be seen from the above tables that the values of coefficient of variation in both mix designs across all the batches are less than 6%. This demonstrates consistency in the mixes, likely due to the high shear mixer's ability to homogenize the materials. It is also noted that compressive strength of 1F24Sf25 is lower than that of 1F31K8 for all three curing times. 1F24Sf25 is based on a non-proprietary mix design by Graybeal with a reported compressive strength of 29 ksi.[79] It should be noted that the material suppliers here may not be the same as those used by Graybeal. Also, the mixer used to make the UHPC batches in Graybeal's studies is an open, 1/2 horsepower bench top mixer that is not identical to the one used in this investigation. These reasons could have led to discrepancies in results between literature and this investigation.

Compressive Strength Results of Cubes vs. Cylinders

Cylinder specimens were cast and tested alongside cube specimens for batches of 1F31K8 that were used as closure pours between precast concrete deck panels. Further detail regarding construction of closure pours between precast concrete deck panels will be discussed in Chapter 7. Figure 58 shows cylinder specimens that failed under compression. Like the cube specimens, the cylinder specimens also displayed ductile modes of failure. Delamination of surface is evident in all the cylinder specimens.

Figure 58. Photo. 3 in. by 6 in. cylinders after compression tests.

The compressive strength results of 1F31K8 are summarized in Table 28. Batch numbers that start with the letter “C” indicate that these batches were used to construct closure pours of structural test specimens. The coefficient of variability for these results are summarized in Table 29. The data suggests that there is only a minor difference in strength values of 3 in. by 6 in. cylinders and 100 mm cubes until the 28-day tests. Coefficient of variability across different batches, test days, and specimen shapes also suggest that there is consistency in the mixes. This suggests that cube specimens may be viable to evaluate the compressive strength of UHPC. Using cube molds for casting UHPC is more convenient because of multiple smooth testing surfaces, whereas cylinders require grinding down both ends to ensure smooth testing surfaces.

Table 28. Average compressive strength of 1F31K8 used in closure pours.

Batch No.	Days Cured					
	3		7		28	
	Cubes	Cylinders	Cubes	Cylinders	Cubes	Cylinders
	Average strength (ksi)					
C1	15.50	15.44	17.45	17.96	21.04	23.92
C2	16.02	16.13	18.34	18.89	20.32	24.31
C3	15.83	15.52	17.66	18.73	--*	--*
C4	16.75	16.57	18.71	20.48	--*	--*
C5						
C6						

Table 29. Coefficient of variability of compressive strength of cylinders and cubes.

Batch No.	Days Cured					
	3		7		28	
	Cubes	Cylinders	Cubes	Cylinders	Cubes	Cylinders
	Coefficient of variability (%)					
C1	3.06	--*	0.37	--*	2.09	--*
C2	0.49	1.37	1.13	0.25	2.34	0.76
C3	0.82	3.11	2.07	1.62	--**	--**
C4	1.05	0.46	2.27	1.72	--**	--**
C5						
C6						

*: only one cylinder was tested, no coefficient of variability was calculated.

Flexural Performance

Flexural performance of beam specimens was evaluated using four-point bending configuration, as detailed in Chapter 5. Flexural tests were conducted over tensile tests because of their ease of testing. Due to the steel fibers in the UHPC matrix, every specimen failed in a ductile manner. Figure 59 shows how a crack that formed in the middle third of the span gradually increased in size throughout the test. This is in stark contrast to

the brittle way an unreinforced UHPC beam fails, as shown in Figure 60. An overview of the failure mode of UHPC beam specimens with fiber reinforcement is shown in Figure 61.

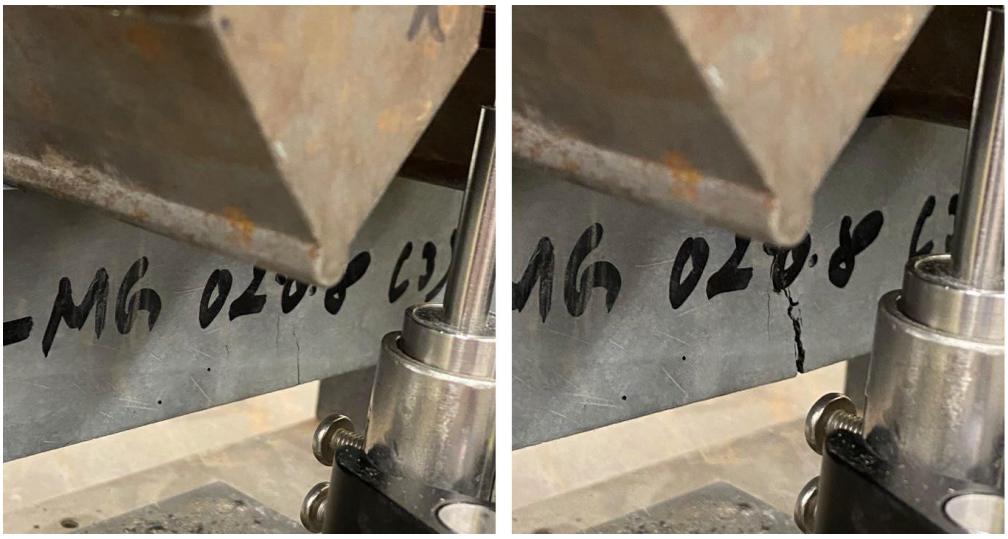

Figure 59. Photo. Formation of a major crack in a beam specimen during four-point bending test.

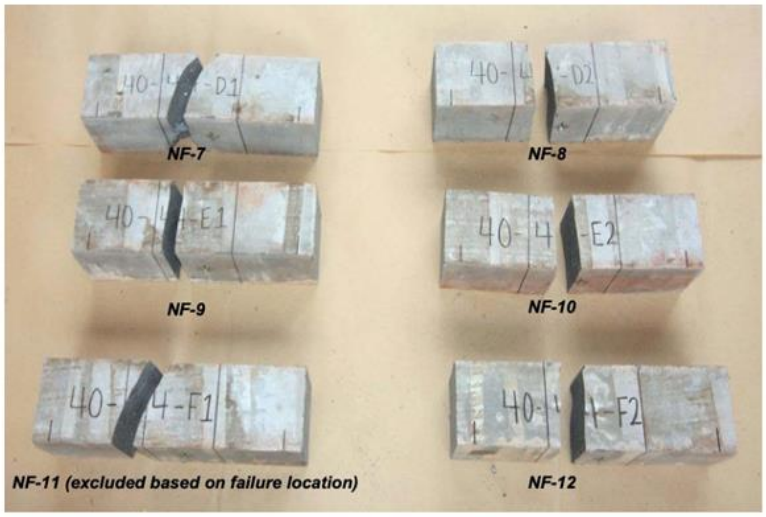

Figure 60. Photo. Unreinforced Cor-Tuf beams after failure.[74]

Figure 61. Photo. UHPC beam specimens after failure.

The ductility of 1F31K8 can be observed quantitatively in the load-displacement graph acquired from testing. Figure 62 and Figure 63 show representative load- displacement graphs of three 2 in. by 2 in. by 17 in. and 3 in. by 3 in. by 12 in. specimens, respectively. After the first peak load, the UHPC beams maintain load carrying capacity throughout the duration of the test, until at least a midspan deflection of L/150, where L represents span length. The modulus of rupture, as determined using Figure 64, of 1F31K8 beams cast during development are summarized in Table 30.

The same quantities for beams cast during construction of closure pours of structural specimens are summarized in Table 31. The modulus of rupture at both peak load and first peak load are at least 2,000 psi across all specimens that have been tested regardless of their dimensions. To compare with data from literature, the average flexural strength was used to compare the flexural strength of both 2 in. by 2 in. and 3 in. by 3 in. beams.

Table 32 and Table 33 summarize the average flexural strength of 1F31K8 beams. The average flexural strength of 2 in. by 2 in. beams across all the batches is 2,895 psi. The average flexural strength of beams of equivalent dimension and span from Graybeal is 3,775 psi. The difference in strength may arise from the fact that all the beams in this investigation were tested 28 days after casting and were stored in a curing room until the day of the test. Graybeal's specimens were tested three months after casting and most specimens underwent steam curing.[34]

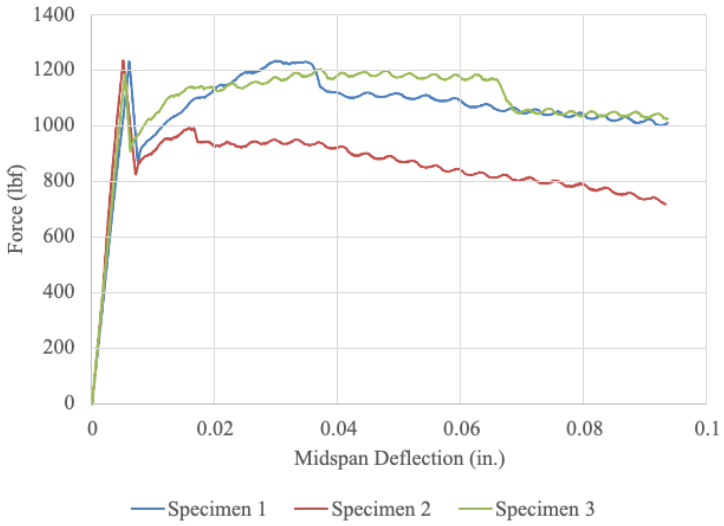

Figure 62. Graph. Load versus displacement graph of 2 in. by 2 in. beams.

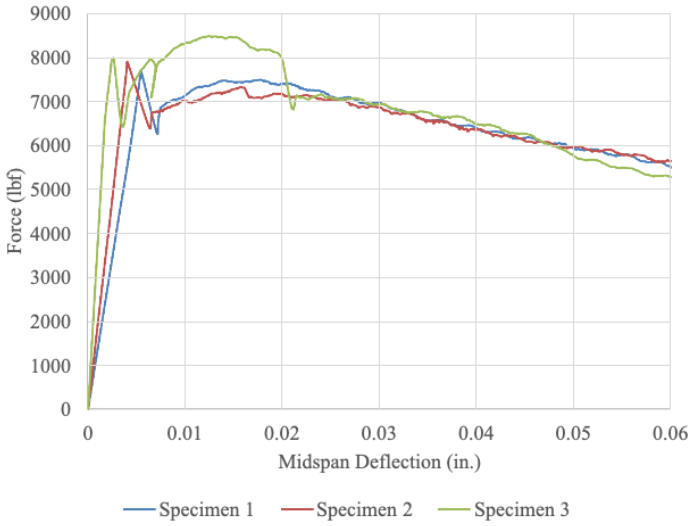

Figure 63. Graph. Load versus displacement graph for 3 in. by 3 in. beams.

$$f_r = \frac{PL}{bd^2}$$

where:

f_r: modulus of rupture, psi
P: the load, lbf
L: the span length, in.
b: average width of the specimen at the fracture, as oriented for testing, in., and
d: average depth of the specimen at the fracture, as oriented for testing, in.

Figure 64. Equation. Modulus of rupture.

Table 30. Average modulus of rupture of 1F31K8 beams cast during development.

Dimension *b* by *h* by *l* (in.)	Span (in.)	Modulus of rupture at first peak load (psi)	Modulus of rupture at peak load (psi)
2 by 2 by 17	14	2215	2550
3 by 3 by 12	9	2385	2860

Table 31. Average modulus of rupture of 1F31K8 beams cast during closure pour construction.

Dimension *b* by *h* by *l* (in.)	Span (in.)	Modulus of rupture at first peak load (psi)	Modulus of rupture at peak load (psi)
2 by 2 y 17	14	2845	3045
3 by 3 by 12	9	2735	3250

Table 32. Average flexural strength of 1F31K8 beams cast during development.

Dimension *b* by *h* by *l* (in.)	Span (in.)	Average flexural strength (psi)
2 by 2 by 17	14	2740
3 by 3 by 12	9	2860

Table 33. Average flexural strength of beam specimens cast during closure pour construction.

Dimension *b* by *h* by *l* (in.)	Span (in.)	Average flexural strength (psi)
2 by 2 by 17	14	3125
3 by 3 by 12	9	3250

Upon completion of each test, specimens were inspected to determine whether the major cracks occurred within the middle third of the respective spans. Data of specimens with cracks that occurred outside of the middle third are not reported. Figure 65 through Figure 68 show major cracks that occurred in 2 in. by 2 in. and 3 in. by 3 in. beams.

Figure 65. Photo. Major crack in the middle third of a 2 in. by 2 in. beam.

Figure 66. Photo. Close-up of the major crack that occurred in the 2 in. by 2 in. beam.

Figure 67. Photo. Major crack in the middle third of a 3 in. by 3 in. beam.

Figure 68. Photo. Close-up of the major crack in the 3 in. by 3 in. beam.

It was observed that the steel fibers bridge the major cracks in the two specimens. The engagement of steel fibers in the cracked zone of the cross section allows for a ductile failure of UHPC beams. Rupture of steel fibers was not observed, which indicates that the failure mode of UHPC beams occurred due to fiber pullout from the matrix. The ductile mode of failure was also observed in the case of compression tests. The ductile behavior of UHPC can potentially allow for reduction of the amount of steel reinforcement as well as the reduction of the development length of individual reinforcement bars.

CHAPTER 7. STRUCTURAL EXPERIMENTS

To evaluate structural viability of the UHPC with Georgian materials in joint pours, precast concrete deck panels of various dimensions were constructed with reinforcing steel bars protruding from one side. All panels in this investigation were fabricated at Tindall Corporation's precast concrete plant in Conley, Georgia. Two panels of equal dimension and embedment length of reinforcement were connected to each other using UHPC as a closure pour. Much of the design of concrete panels and the test setup were based on Graybeal's previous research on UHPC connections between precast bridge deck elements. This chapter describes the design, construction, testing processes and results for the structural evaluation of UHPC closure pours.

PRECAST CONCRETE DECK PANELS

Design

The precast concrete deck panels that are joined together by UHPC were designed as if they were monolithically cast. Protruding reinforcement from two deck panels were interlaced to create a non-contact lap splice region. This connection region was then filled with UHPC. A plan view of 28 in. by 48 in. panels is shown in Figure 69. Two different types of concrete panels were constructed with different dimensions, connection region geometry, and embedment length of reinforcing bars into UHPC. Table 34 summarizes variables in each of the panels. Most of the specimens employ 5 in. of embedment length and 4 in. of non-contact lap splice of protruding rebars in the UHPC connection. This is a recommendation from Graybeal's previous research. It also followed GDOT's current practice, which specifies a minimum embedment length of 8 times the bar diameter.[34]

This requirement applies for No. 8 bar and smaller with yield strength of 75 ksi or less embedded in UHPC with 2% steel fiber content by volume.[23]

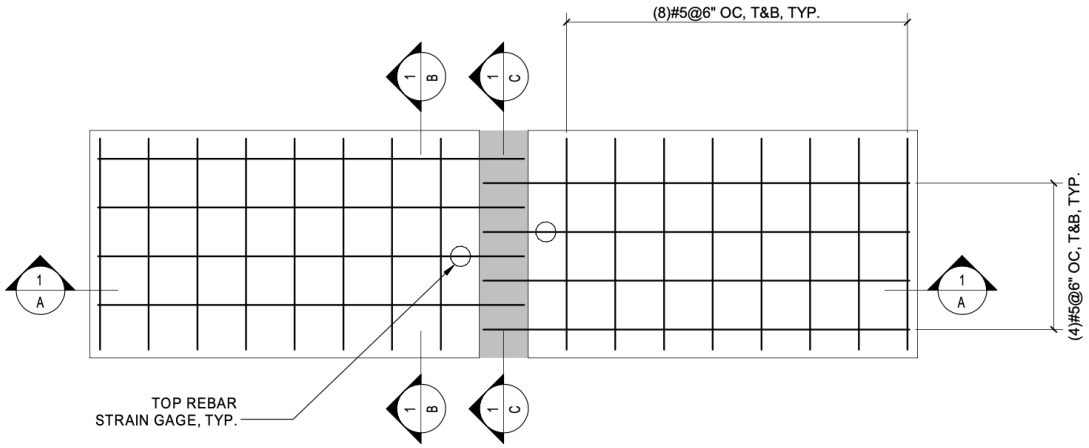

Figure 69. Engineering Drawing. Plan view of a structural test specimen (2) 28 in. by 48 in. panels.

Table 34. Parameters of various precast concrete deck specimens.

Panel dimension *b* by *l* by *h* (in.)	**Embedment length (in.)**	**Non-contact lap splice (in.)**	**Key geometry**	**Quantity**
28 by 48 by 6	5	4	None	4
28 by 48 by 6	5.75	5.5	None	4
28 by 48 by 9	5	4	GDOT specified	4

The panels have two types of connection geometry as shown in Figure 70 and Figure 71. In Graybeal's previous research, triangular and trapezoidal shear key geometries were used to increase the bonding area between UHPC and precast concrete as shown in Figure 72. However, such geometries involve more detailed and extensive effort in creating formworks. To address this issue, specimens that do not incorporate key geometries were constructed along with those that have geometries specified by GDOT. The surfaces of

concrete panels that are in contact with UHPC is specified to have EA surface with 1/8 in. amplitude per GDOT's recommendation to enhance the bond between UHPC and concrete panels.

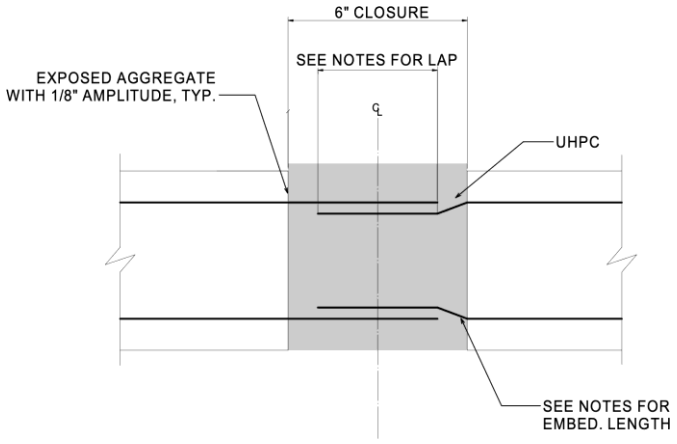

Figure 70. Engineering Drawing. Joint detail without shear key.

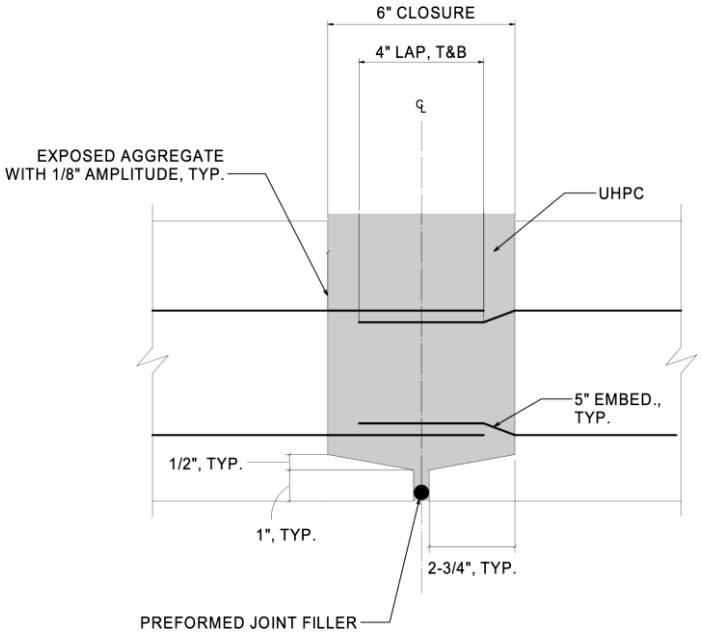

Figure 71. Engineering Drawing. GDOT specified joint detail.

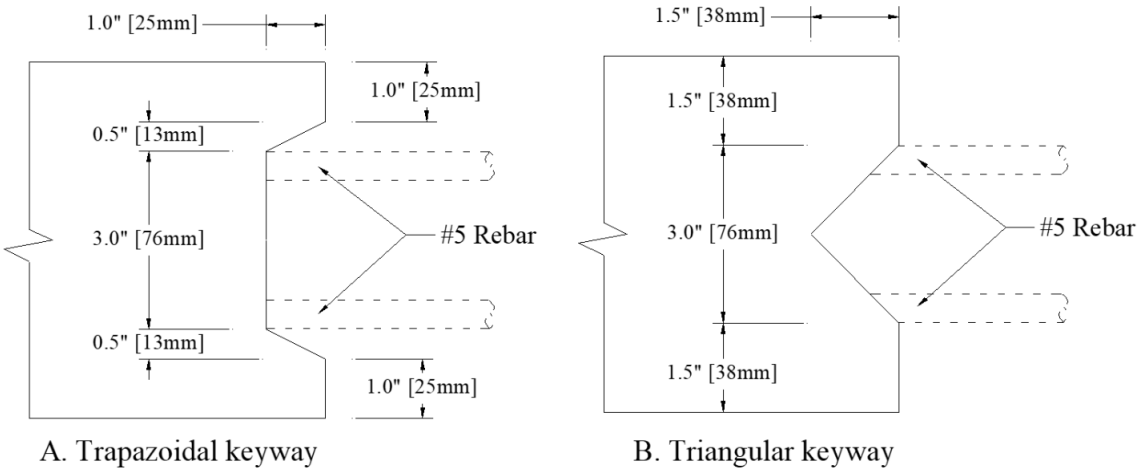

Source: FHWA

Figure 72. Engineering Drawing. Trapezoidal and triangular shear key details.(40)

Strength calculations were performed with the assumption that these panels are monolithically cast with continuous reinforcement. Whitney stress block analysis was used to calculate the moment capacity of the panel cross section. The specified compressive strength of the deck panels is 6,000 psi at 28 days. Detailed calculations can be found in Appendix C and Appendix D for the 6 in and 9 in thick panels respectively. The nominal cracking, yielding, and ultimate moment strengths of 6 in. thick panels are summarized in Table 35. Only No. 5 black bars of Grade 60 are used as reinforcement in this study. Figure 73 shows the cross-sectional used to calculate the moment capacity of deck panels.

Table 35. Cracking, yielding, and nominal moment capacities of 6 in panel cross sections.

Final panel dimension *b* by *h* by *l* (in.)	**Cracking moment, M_{cr} (kip-ft)**	**Yield moment, M_y (kip-ft)**	**Nominal moment, M_n (kip-ft)**
28 by 6 by 102	8.01	26.33	27.45

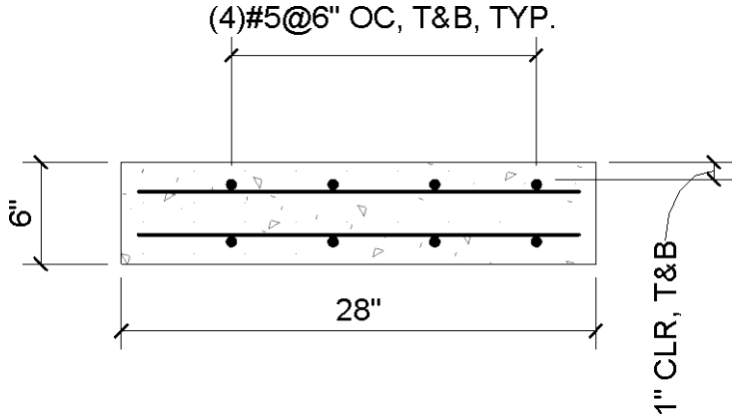

Figure 73. Engineering Drawing. Cross-section of 6 in. thick deck panel specimen.

Construction

All precast deck panels were constructed at Tindall Corporation's precast concrete plant in Conley, Georgia. For every deck panel, a strain gauge was installed on one of the No. 5 bars that will be in tension during structural load testing. Figure 74 shows a No. 5 bar that has been ground to create a smooth surface for strain gauge installation. All strain gauges are from Vishay Precision Group, Inc. (VPG) and have resistance of 350 Ω (±0.3%). The bond agent used to attach these strain gauges to the bars is also from VPG. Strain gauges were wrapped with layers of electric tape and foam tape to provide protection from concrete and water during deck panel construction as shown in Figure 75. Spray on sealant was used to add another layer of protection against water seepage in Figure 76.

Figure 74. Photo. Surface preparation for strain gauge attachment.

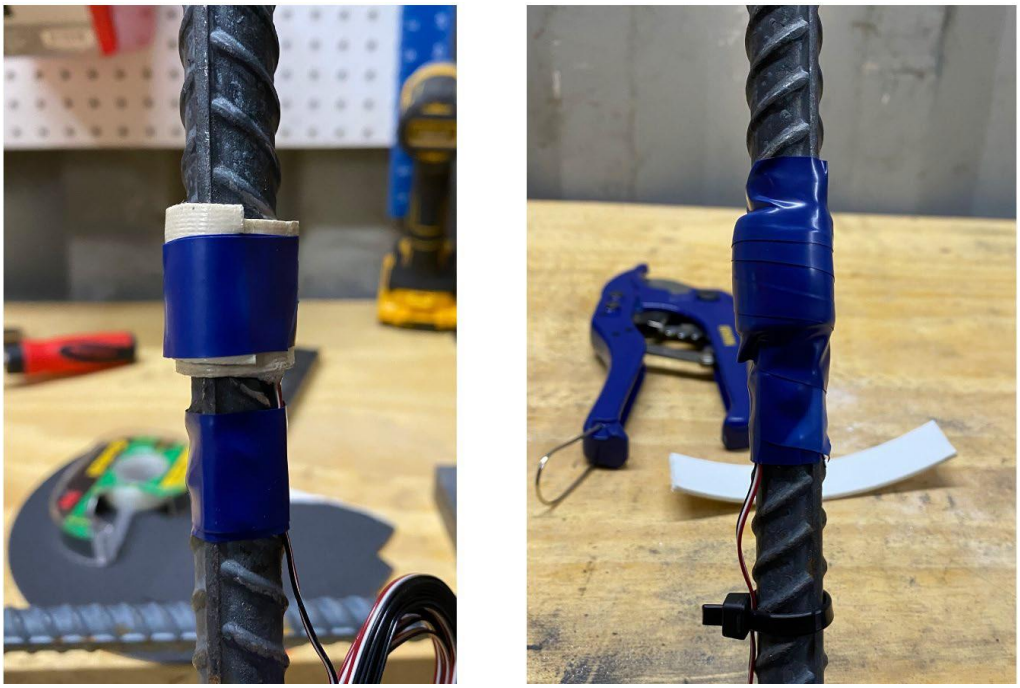

Figure 75. Photo. Foam tape and electrical tape used to protect the attached strain gauge.

Figure 76. Photo. Spray-on sealant being applied to provide protection against water.

Once strain gauge installation was complete, the bars with strain gauges were placed in their respective locations in the panel formworks. An example of a bar as part of the reinforcement cage is shown in Figure 77. Spacing between reinforcing bars and cover distances were measured to ensure panel construction adheres to the design specifications. Figure 78 shows a measurement being taken to confirm spacing of reinforcing bars. Figure 79 shows another measurement that confirms the cover distance of bottom bars for one of the larger panels. A layout of reinforcing bars for a 28 in. by 48 in. by 9 in. panel is shown in Figure 80. Hooked No. 4 bars were installed prior to casting all the panels for lifting purposes shown in Figure 81.

Figure 77. Photo. No. 5 bar with a strain gauge inside reinforcement cage.

Figure 78. Photo. Checking reinforcement spacing of 6 in.

Figure 79. Photo. Checking bottom cover of steel reinforcement in a specimen.

Figure 80. Photo. Reinforcement cage of a 28 in. by 48 in. by 9 in. specimen.

Figure 81. Photo. Hooked No. 4 bars placed inside reinforcement cage for lifting purposes.

After placing the reinforcing bars, the deck panels were cast in one batch using a ready-mix truck shown in Figure 82 and Figure 83. Once all the panels were cast, they were covered with tarp to prevent moisture loss, as shown in Figure 84. All the formwork was removed 4 days after casting. Figure 85 shows compression test cylinders that were cast to evaluate concrete strength at 7 and 28 days after casting and on the day of the structural test. Four cylinders were tested on each of the test days. The compressive strength of concrete used in deck panels is summarized in Table 36. The compressive strength tests adhered to procedures outlined in ASTM C39.

Figure 82. Photo. Deck panel specimen being cast with ready-mix truck.

Figure 83. Photo. Deck panel specimens being cast.

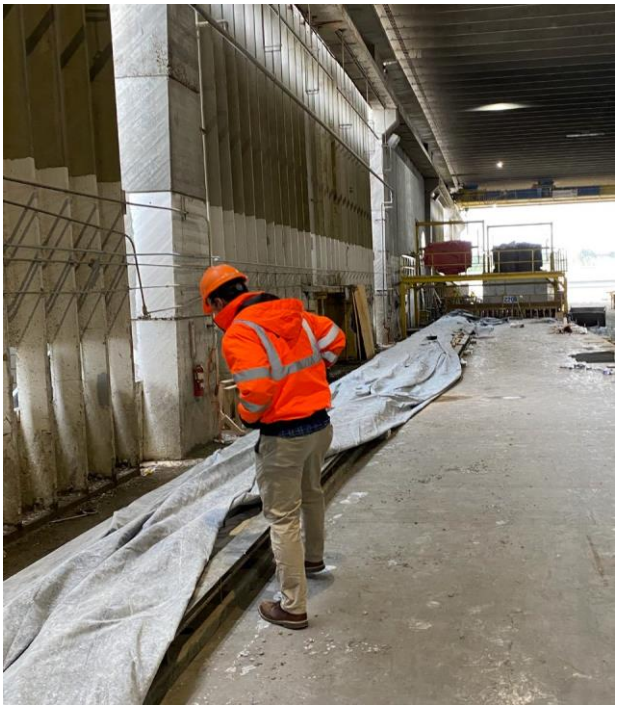

Figure 84. Photo. Tarp used to cover all specimens after casting.

Figure 85. Photo. 4 in. by 8 in. cylinders cast to evaluate concrete strength.

Table 36. Compressive strength of concrete used in deck panels at 7 and 28 days.

Days after casting	Compressive strength (psi)	COV (%)
7	5,775	11.53
28	6,800	3.12

Once all the formwork was removed, the panels were sand blasted to create EA surfaces on the sides where UHPC will come into contact. Sand blasting of the panels is shown in Figure 86. GDOT typically specifies 1/8 in. amplitude of the EA surface for bridge construction in Georgia. The surfaces were constantly checked to ensure correct amplitude of the EA surface shown in Figure 87. An overview of EA finish on one of the panels is shown in Figure 88.

Figure 86. Photo. Sand blasting to create EA surface on specimens.

Figure 87. Photo. Measurement of 1/8 in. of EA amplitude.

Figure 88. Photo. Sand-blasted surface.

Transport

Panels were delivered to the Structural Engineering and Materials Laboratory (SEML) at Georgia Institute of Technology 28 days after they were cast. During transport, some of the panels that incorporated GDOT's key geometry suffered damages in the joint area. Figure 89 shows a damaged joint of one of the concrete deck panels during transport. The "lips" of the joint detail are known to be quite fragile, as it is a commonly occurring phenomena in GDOT's construction practices. It is also for this reason that this research is considering deck panels that do not incorporate the "lips" details. Structural test specimens constructed using these deck panels will allow for an evaluation of eliminating joint details to ease construction processes in the field.

Figure 89. Photo. Damage to GDOT specified joint detail during transport.

STRUCTURAL TEST SPECIMENS

Joint Constrution

Structural test specimens were constructed by placing identical deck panels in such a way that each of the panels' EA surfaces face each other. The joint was measured to ensure 6 in. of width in Figure 90. The protruding reinforcement were interlaced and create non-contact lap splice in the connection shown in Figure 91. Setup of a structural test specimen using deck panels that are 6 in. thick is shown in Figure 92.

Figure 90. Photo. 6 in. wide joint region between two deck panels.

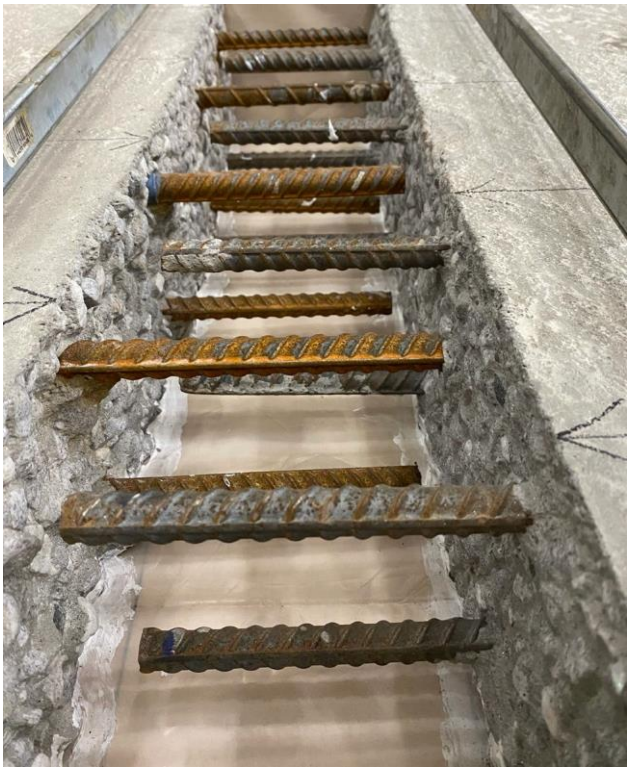

Figure 91. Photo. Non-contact lap splice in the joint region.

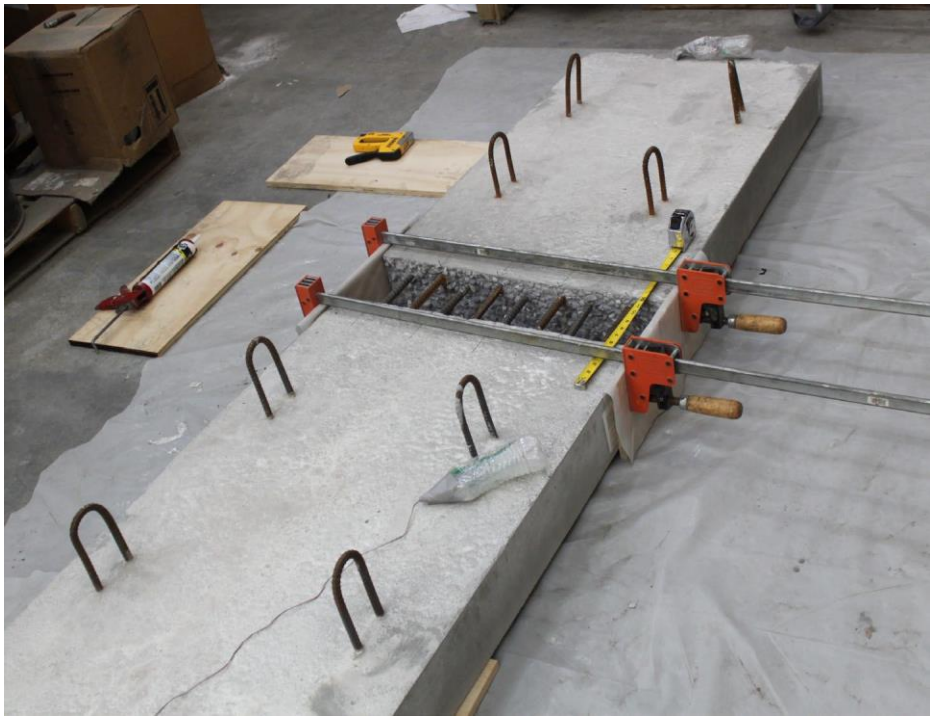

Figure 92. Photo. Setup of two deck panels ready for joint pour.

One batch of UHPC was made to construct the closure pours in one structural specimen and to cast compressive and flexural test specimens. Each batch had 1.6 ft^3 of UHPC. Figure 93 shows the construction of the UHPC joint. UHPC was poured at one end of the joint and was allowed to flow to the other end until the joint was filled. Each joint was filled with UHPC in one pour to prevent the formation of interfaces inside the UHPC. A closer look at the joint during and after UHPC pour is shown in Figure 94 and Figure 95 , respectively. After pouring, the UHPC was covered with plastic to prevent shrinkage.

Figure 93. Photo. UHPC joint pour.

Figure 94. Photo. Close-up of UHPC joint pour.

Figure 95. Photo. UHPC joint after 3 days of curing time and removal of formwork.

As discussed in Chapter 5, 100 mm cube and 3 in. by 6 in. cylinder specimens were tested to evaluate compressive strength at 3, 7, and 28 days after casting. Beam specimens were tested 28 days after casting. Cubes, cylinders, and beams were demolded 24 hours after casting. These specimens were placed in a fog room at 73˚F until testing.

TEST MATRIX

The structural test program consisted of six experiments. The test matrix for the program is given in Table 37. The nomenclature for the naming is L-#-#.#-L. The first letter represents the Key Geometry, “N” for none and “G” for GDOT Specified. The first number is the depth of the panel, the second number is the embedment length, and the final letter designates the specimen of that type.

Table 37. Structural experiments test matrix.

Name	Dimension *b* by *h* by *l* (in.)	Embedment length (in.)	Non-contact lap splice (in.)	Key geometry
N-6-5.0-A*	28 by 6 by 102	5	4	None
N-6-5.75-A*	28 by 6 by 102	5.75	5.5	None
N-6-5.0-B	28 by 6 by 102	5	4	None
N-6-5.75-B	28 by 6 by 102	5.75	5.5	None
G-9-5.0-A	28 by 9 by 102	5	4	GDOT Specified
G-9-5.0-B**	28 by 9 by 102	5	4	GDOT Specified

*Test was considered a proof-of-concept to verify instrumentation and test setup.
**Specimen had large shrinkage crack prior to testing.

TEST N-6-5.0A

The first experiment was conducted on a 6-in. deep specimen with a 5-in. embedment length and no key geometry. It was used as a proof-of-concept test to verify the instrumentation and setup.

Setup

Figure 96 shows an overview of the structural test setup. A negative bending configuration was chosen to easily observe cracks as well as any debonding between UHPC and precast concrete throughout the test. LVDTs were attached on both the tension and compression faces of the concrete specimen. These LVDTs were used to measure the change in displacement across the UHPC joint region. A string potentiometer was installed on the floor to measure the midspan deflection of the specimen as it is loaded. Strain gauges that were pre-installed on two reinforcing bars inside the deck panel specimen are used to measure strain in steel reinforcement. A load cell with a capacity of 100 kips was attached to a hydraulic ram that was operated by a pump with a shut off valve. The load cell bears on a steel plate via a steel sphere that is allowed to rotate to prevent

the hydraulic ram from applying the load at an angle. A W8x48 beam was used to spread the load from the hydraulic jack to the two ends of the deck panel specimen. The panel specimen tested in this investigation incorporated steel reinforcing bars with 5 in. of embedment length and 4 in. of non-contact lap splice in the UHPC joint.

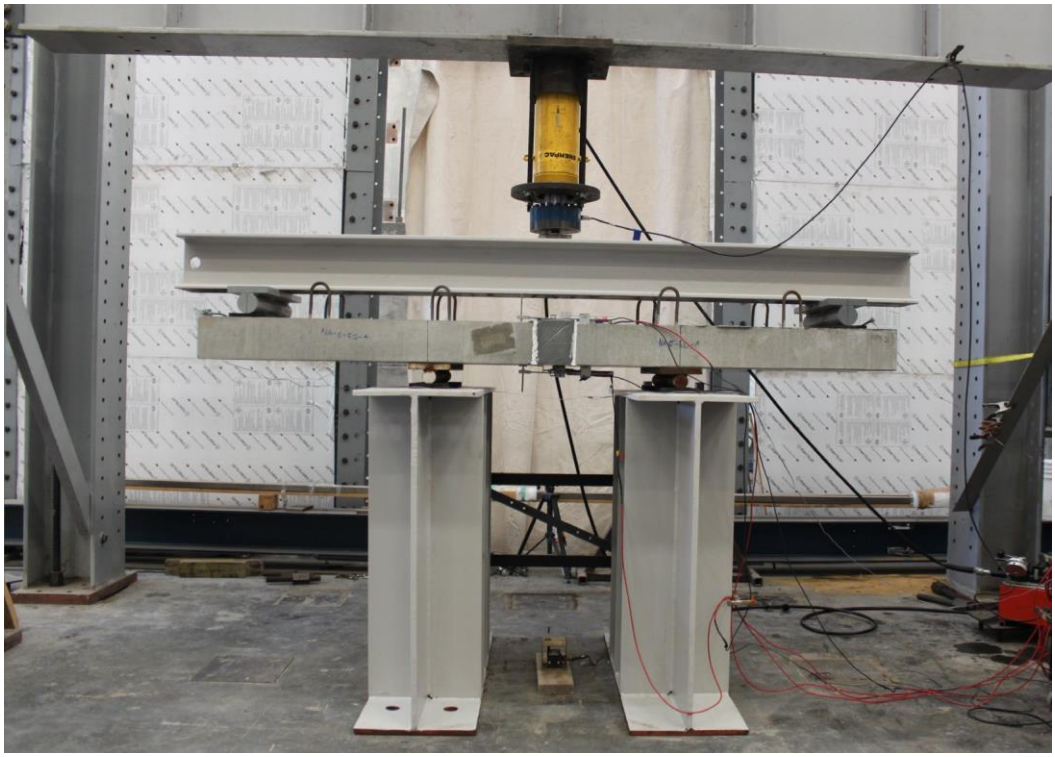

Figure 96. Photo. Deck panel specimen ready for load test.

The deck panel specimen underwent quasi-static loading at a rate of approximately 0.02 in./min. During the test, the applied load was held constant at a) M_{cr}, b) between M_{cr} and yield moment, M_y, c) at nominal moment, M_n, and beyond. This was done to identify cracks that occurred in the maximum moment region, particularly near and in the UHPC joint. The concrete deck panels had an average compressive strength of 7,445 psi with COV of 1.66% on the day of the test. Based on this strength, the load to reach M_{cr} was 7.25 kips. The loads to reach M_y and M_n, were 22 and 23 kips, respectively.

Observations

Visual inspection of the deck panel specimen was conducted at M_{cr} at a load of 7.25 kips. Few cracks were observed in the concrete deck in the maximum moment region. There were no cracks that formed inside the UHPC connection region. Figure 74 shows cracks that were traced at M_{cr}. It is important to note that no visible cracks were observed in the UHPC, as expected.

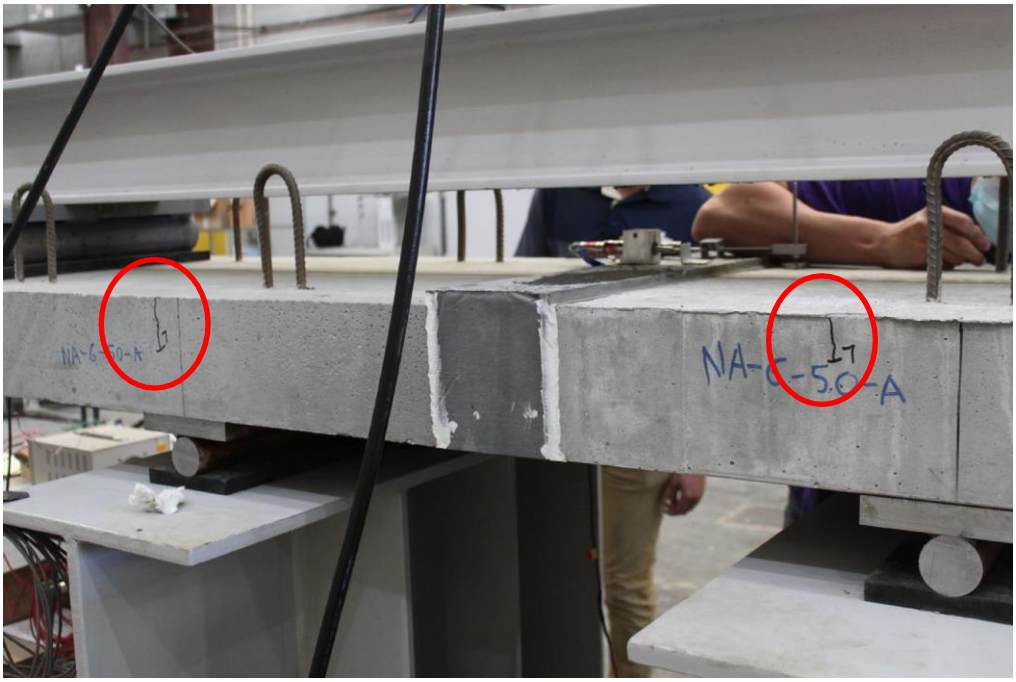

Figure 97. Photo. Cracks observed at M_{cr} circled in red.

The load was held constant at $0.7M_y$ to inspect for any cracks in the deck panel specimen. Additional cracks propagated in the maximum moment region as shown in Figure 98. Cracks also occurred at the interface between the UHPC connection and concrete deck as shown in Figure 99 and Figure 100. No cracks were visible on the surfaces of UHPC joint. The larger cracks in the concrete deck within the maximum moment region indicate engagement of steel reinforcement as the specimen is being loaded.

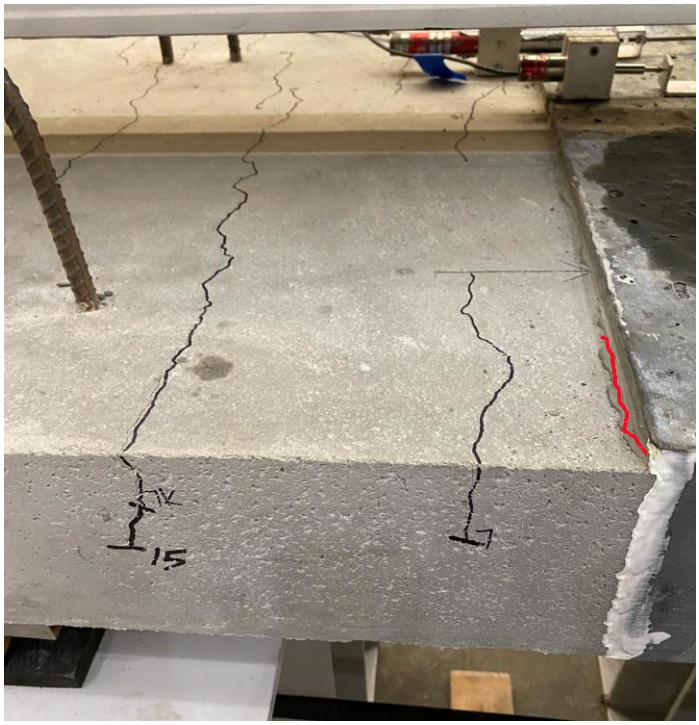

Figure 98. Photo. Cracks in the maximum moment region at 0.7M_y.

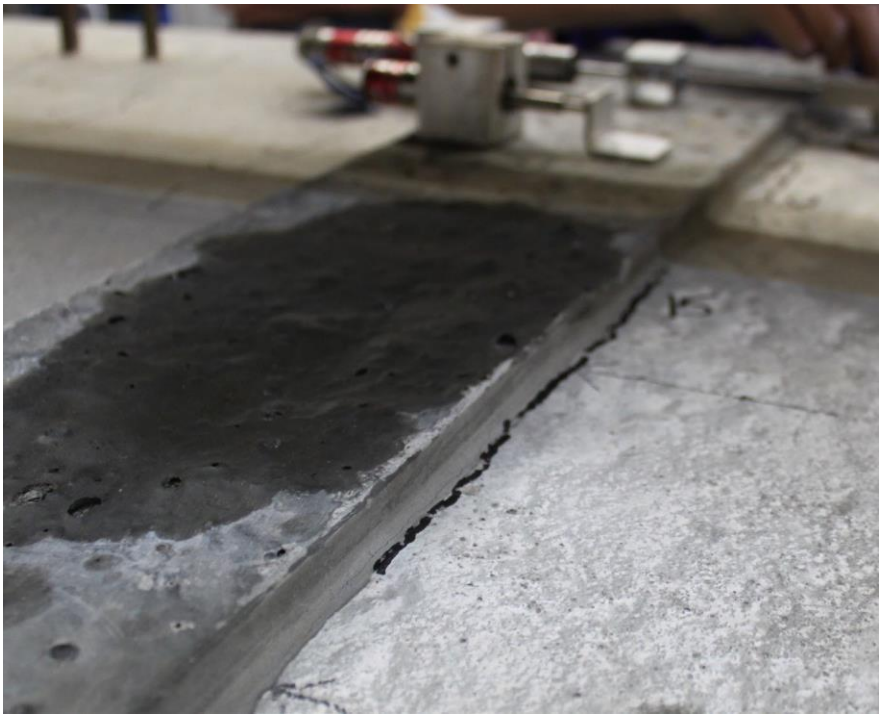

Figure 99. Photo. Cracks at the interface between the UHPC joint and concrete deck panel.

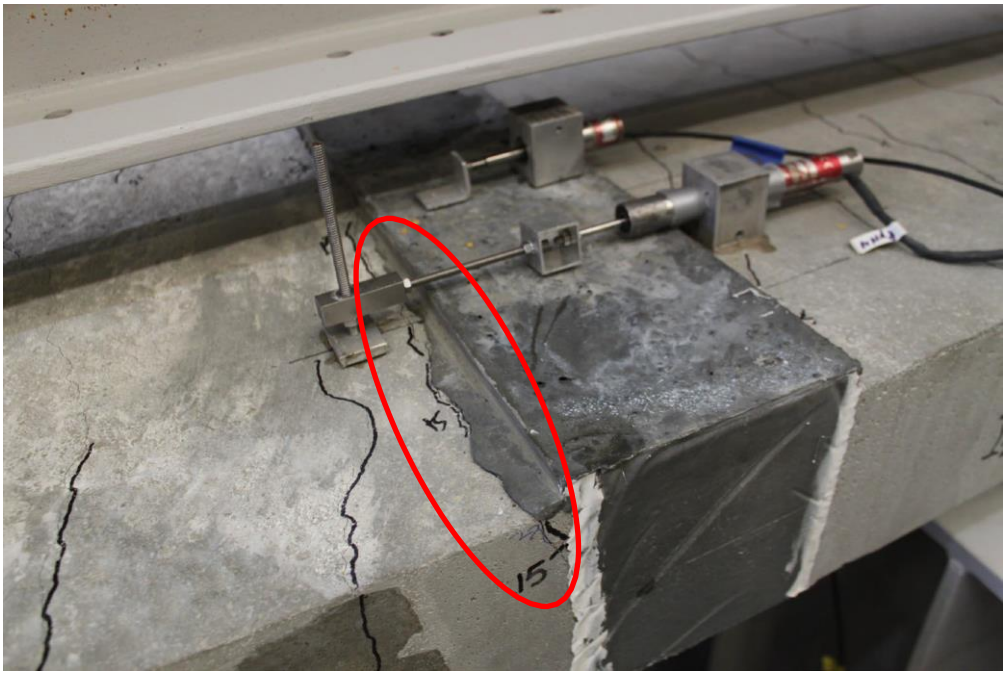

Figure 100. Photo. Cracks at the interface shown inside the red ellipse.

The applied load was held constant at M_y to inspect crack propagation in the specimen, especially in the UHPC connection. The previously observed interface crack had propagated as shown in Figure 101. This crack had a width of 0.007 in. The cracks in the concrete deck within the maximum moment region had a typical width of 0.020 in. These cracks have also propagated throughout the tension surface of the specimen as shown in Figure 102. No cracks were observed inside the connection region.

Figure 101. Photo. Propagation of interface crack at M_y.

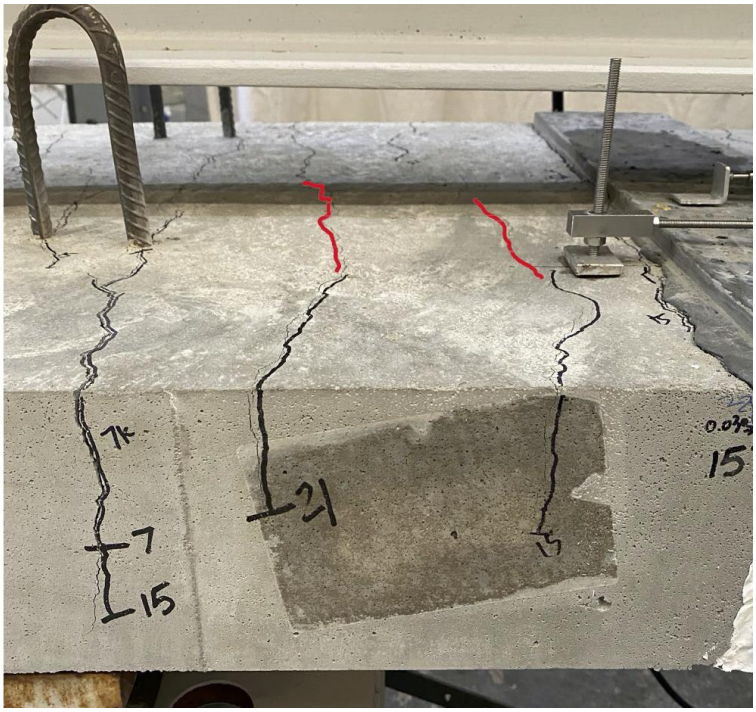

Figure 102. Photo. Crack propagation in the maximum moment region at M_y.

At the nominal flexural strength of the deck panel specimen, interface cracks had an increase in width from 0.007 in. to 0.03 in. The increase in crack width is shown in Figure 103. Thin cracks were also seen on the top face of the UHPC joint as shown in Figure 104.

Figure 103. Photo. Wider crack observed at the interface at M_u.

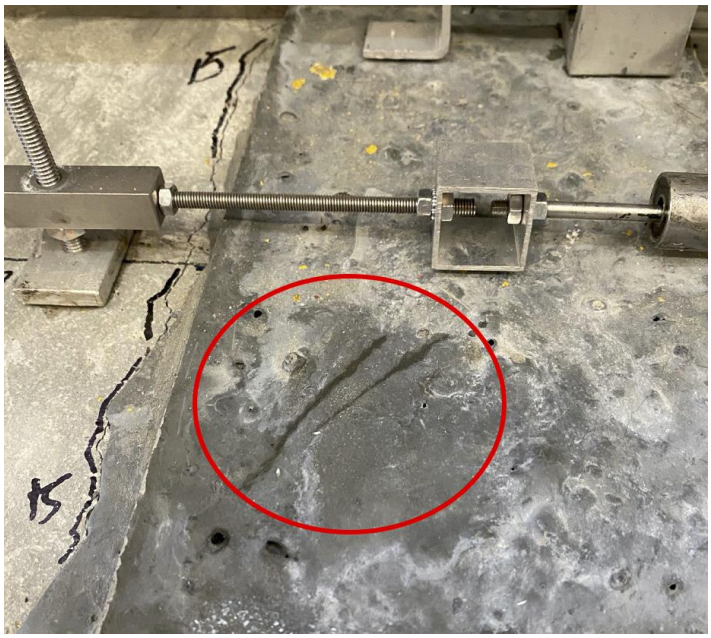

Figure 104. Photo. Cracks on the top face of UHPC joint at circled in red.

At 1.3M_n, the load was held constant to observe any cracks within the UHPC joint. Several cracks appeared on the surfaces of the UHPC. Figure 105 and Figure 106 show the surface cracks in UHPC at 1.3M_n. UHPC surface cracks had typical widths of 0.01 in. The interface cracks widened from 0.03 in. to 0.07 in. The string potentiometer malfunctioned during the test. To measure the approximate midspan deflection after the malfunction, an orange string was pulled taut along the length of the specimen. The vertical distance between the string and the midspan was measured to be 2-7/16 in at the end of the test. Figure 107 shows how the deflection was measured.

Figure 105. Photo. Top surface crack in UHPC at 1.3M_n.

Figure 106. Photo. Side surface crack in UHPC at 1.3M_n.

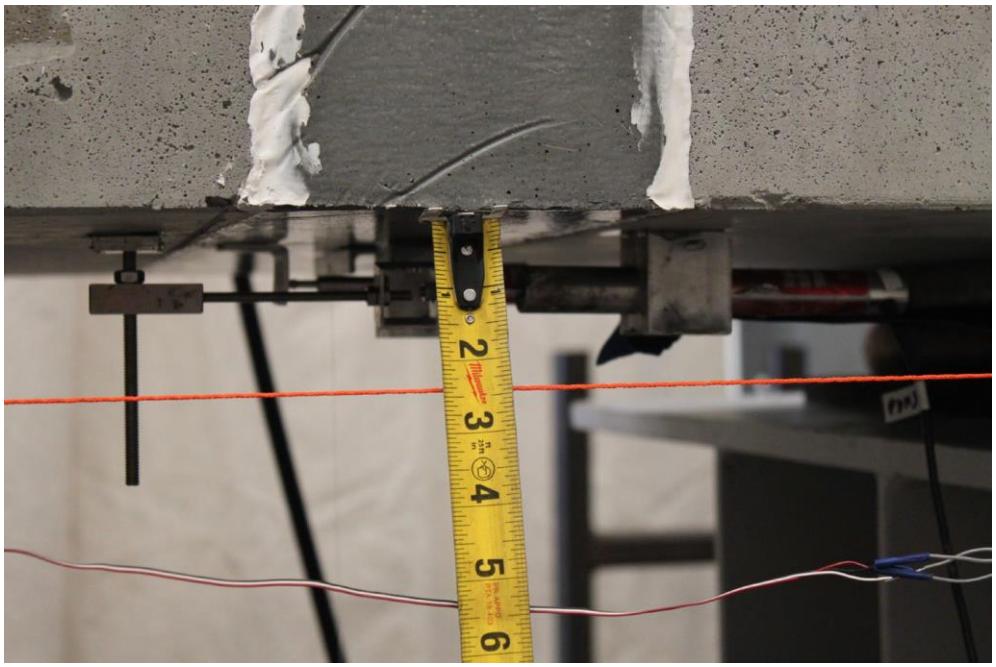

Figure 107. Photo. Approximate measurement of the midspan deflection at 1.3M_n.

Results

Data from LVDT readings are normally used to analyze moment-curvature relationships in the UHPC region and in the concrete deck. LVDTs on the tension side of the UHPC joint region showed erratic results, likely due to a debonding of the mounting. This made it difficult to formulate an accurate moment- curvature relationship within the UHPC joint. As such, it is not appropriate to provide moment-curvature relations for this experiment. However, the conclusions from the test can still be made. The UHPC connection showed no cracks until M_y of the specimen was reached. As the specimen was loaded beyond M_y, thin cracks were observed on the surface of the connection region. Cracks at the interface between UHPC and concrete occurred at lower loads than M_y, but debonding of the two materials was not observed. The steel reinforcing bars have also undergone yielding prior to any observable failure in the connection. These observations indicate a satisfactory behavior of the deck panel specimen that employ the non-proprietary UHPC connection detail. Modifications to the setup and instrumentation were made and are discussed in the following section.

TEST N-6-5.75-A

The second experiment was conducted on a 6-in. deep specimen with a 5.75-in. embedment length and no key geometry. Multiple changes to the experimental setup were made following the lessons learned from the previous experiment.

Setup

The N-6-5.75-A setup included a few major changes, as shown in Figure 108. The support and load plates were originally seated on rubber bearing pads in this research. To ensure even distribution of load in the specimen, the support and load plates were seated

on steel plates, which are then placed on rubber bearing pads. To reduce any tension stiffening effects in the specimen, the support and load plates were replaced such that they are not only free to rotate, but also move horizontally.

Four total LVDTs were mounted to the specimen. Two LVDTs were attached to the tension side of the specimen: one short LVDT within the UHPC portion of the specimen (short gage), and one long LVDT spanning across the UHPC region and attached to the precast concrete panels (long gage). The remaining two LVDTs were mounted to the compression side in the same configuration. These LVDTs were used to measure the linear displacement within and across the UHPC joint because of the tension and compression in the specimen when subject to bending.

Additional instrumentation also included an analog plunge dial gage beneath the specimen to measure the midspan deflection and confirm measurements obtained by the string potentiometer. This dial gage had a maximum range of 4 in. and was positioned such that the upward displacement of the specimen was measured by an extension of the plunger. A digital plunge dial gage was attached to the tension side of the specimen on one side of the UHPC joint and tied to a rigid screw in the panel on the opposite side of the UHPC joint. This was to measure the lateral deflection across the UHPC joint and confirm readings from the LVDTs.

Figure 108. Test N-6-5.0 B setup.

Observations

The specimen at failure is given in Figure 109, Figure 110, and Figure 111. The specimen exhibited crushing of the concrete panels. No cracks or damage was observed in the UHPC joint. The instrumentation and setup functioned appropriately, and the setup was kept consistent for future experiments.

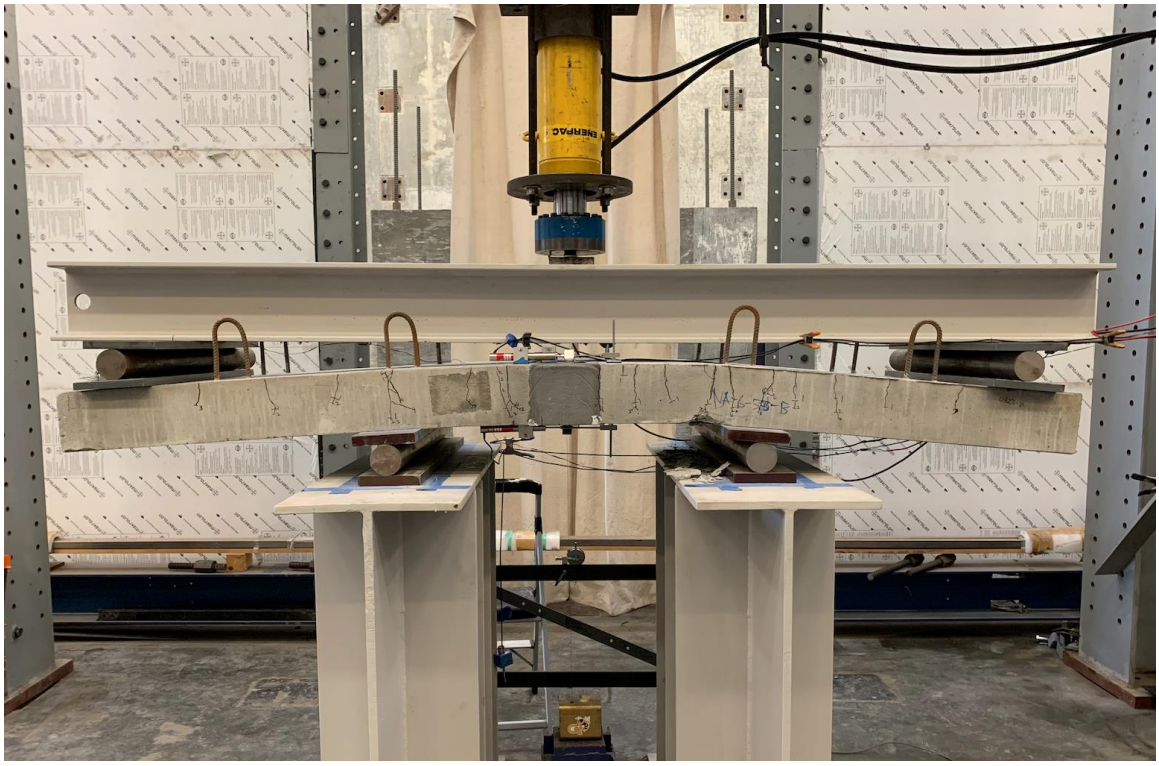

Figure 109. Photo. Specimen N-6-5.75-A at failure.

Figure 110. Photo. Specimen N-6-5.75-A showing concrete panel crushing.

Figure 111. Photo. Specimen N-6-5.75-A tension side at failure.

Results

The force-displacement curve for this experiment is given in Figure 112.

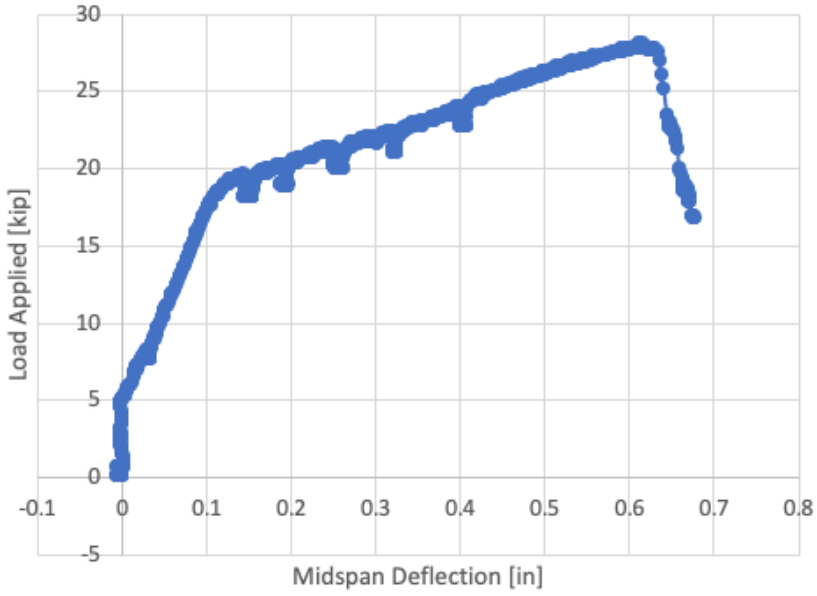

Figure 112. Graph. Force-displacement behavior on N-6-5.75A.

TEST N-6-5.0-B

The third structural experiment was conducted on a 6-in. deep specimen with a 5.0-in. embedment length and no key geometry. This was the second test of this type, as N-6-5.0-A was used as a proof-of-concept to verify the experimental setup.

Setup

The setup, instrumentation, and testing protocol were identical to the second experiment, except for the loading sequence. The specimen was loaded quasi-statically until failure at an average rate of roughly 0.33 kips/min. During testing, loading was paused and held constant at several additional points, including loads corresponding to the cracking moment of the specimen $M_{cr,}$ the yield moment of the specimen M_y, and the nominal moment of the specimen, M_n. This was done to identify and observe the propagation of cracks in the specimen, measure and record notable crack widths and to record data from the dial gages. The calculated M_{cr}, M_y, and M_n of the different cross section types, along

with the applied loads corresponding to these moments are shown below in Table 38 and Table 39. Calculations for the values shown in tables are given in Appendix C.

Table 38. Predicted moments for test specimen sections.

Dimension *b* by *h* by *l* (in.)	Cracking Moment, M_{cr} (kip-ft)	Yield Moment, M_y (kip-ft)	Nominal Moment, M_n (kip-ft)
28 by 6 by 102	8.801	26.33	27.45

Table 39. Predicted applied loads for test specimen sections.

Dimension *b* by *h* by *l* (in.)	Load at Cracking, P_{cr} (kip)	Load at Yield, P_y (kip)	Load at Capacity, P_n (kip)
28 by 6 by 102	6.40	21.99	22.98

Observations

The loading was paused at several points throughout testing to make observations of the test specimen. The observations are as follows, for corresponding loads:

- P = 6.5 kips:

This load corresponds to the cracking moment of the specimen. At this load, small cracks were observed in the concrete panels near the supports of the specimen. These cracks were noted to be <0.005 in. wide at the time of initial observation. As expected, there were no cracks observed within the UHPC region at this loading. The cracks over the supports are shown below in Figure 113.

Figure 113. Photo. Cracks near supports in the precast panels at load P_{cr}.

- P = 10 kips:

At approximately 10 kips, the first appearance of cracking near the UHPC region was observed. Small cracks had formed at the interface between the precast concrete panels and the UHPC joint and were observed on both the west side and east side of the UHPC closure pour. The location of these cracks relative to the UHPC closure pour is shown in Figure 114. These cracks were measured to be <0.005 in. wide at the time of initial observation and were closely monitored throughout the rest of the testing.

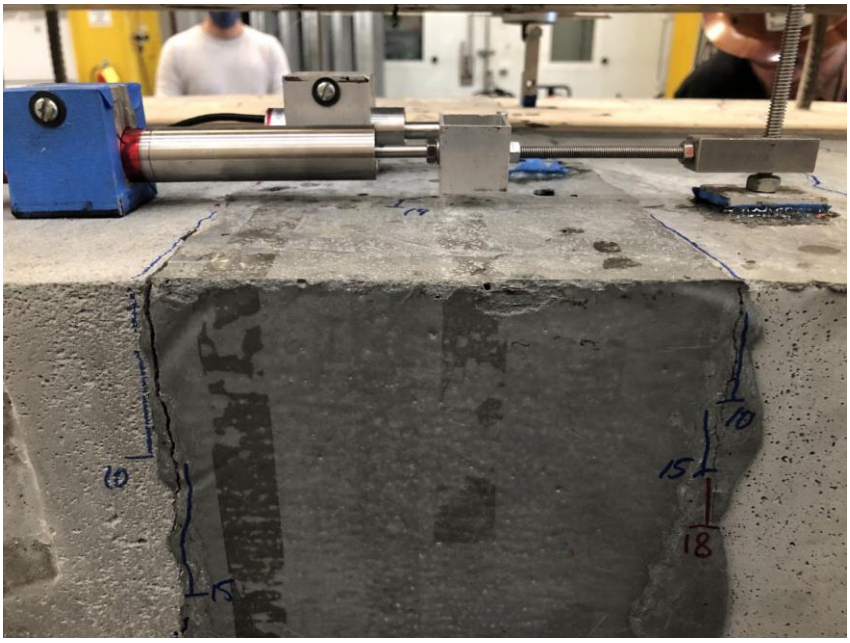

Figure 114. Photo. Cracks surrounding the UHPC joint on the north face of the specimen.

- P = 15 kips:

At approximately15 kips, the largest crack at the UHPC joint and concrete panel interface had widened to approximately 0.015 in. and was observed to have extended across the top of the panel to the other side of the specimen.

- P = 18 kips:

At approximately18 kips, the significant cracks surrounding the UHPC joint were once again measured for width. The results of these measurements are shown below in Figure 115 and Figure 116. At this load, the first cracks within the actual UHPC joint were observed to have formed. All cracks within the UHPC region were noted to be <0.005 in.

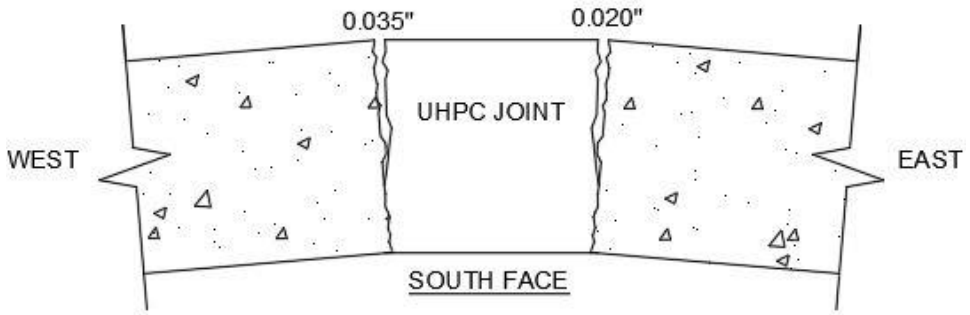

Figure 115. Schematic. Crack widths surrounding UHPC joint on south face of specimen.

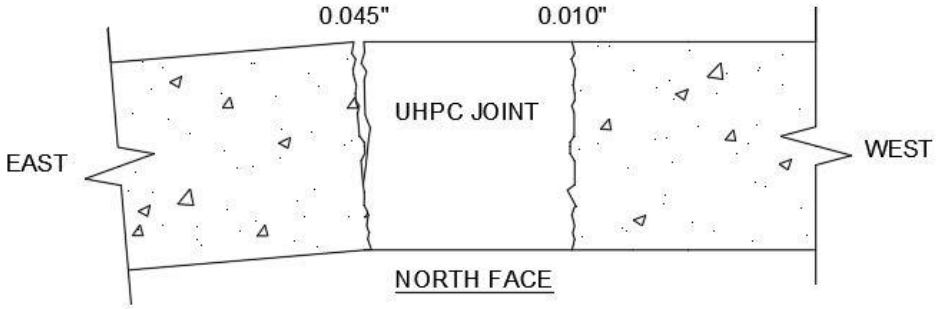

Figure 116. Schematic. Crack widths surrounding UHPC joint on north face of specimen.

At this load, the first cracks within the actual UHPC joint were observed to have formed. All cracks within the UHPC region were noted to be <0.005 in.

After loading to 18 kips, it was observed that the applied load began increasing at a slower rate while the midspan deflection began increasing at a greater rate in comparison to lower ranges of applied loads. This is indicative of yielding of the steel within the concrete. With this observation, researchers began pausing loading more frequently – approximately every 1 kip from 18 kips until P_n was achieved.

- P = 19 kips:

At approximately 19 kips. the cracks surrounding the UHPC had widened. The widest cracks near the UHPC joint on both the south and north face of the specimen were measured to be approximately 0.050 in. These cracks were the same width when measured again at a load of 19.7 kips. Additionally notable is the formation of a small horizontal crack in the precast panel near the location of a tension rebar. This crack could be indicative of debonding of the bar in the precast panel. The same crack did not continue into the UHPC region (see Figure 117).

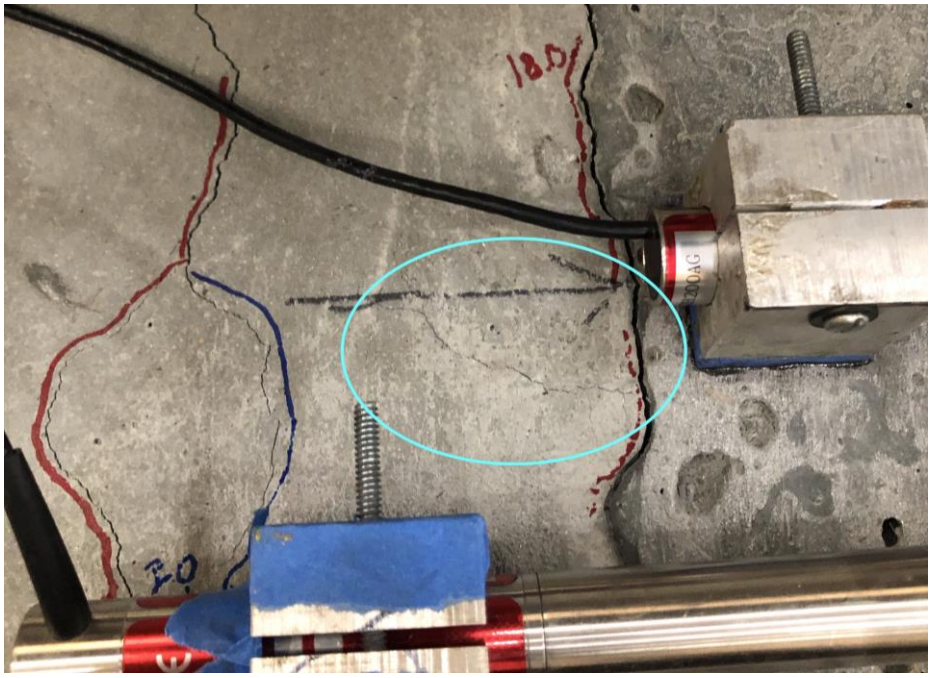

Figure 117. Photo. Horizontal crack formation in precast panel near location of tension bar marked with arrow.

- P = 20.7 kips:

At approximately 20.7 kips, corresponding to a midspan deflection reading from the string potentiometer of about 0.2 in., the widest cracks at the UHPC and concrete interface had widened to a width of about 0.075 in. Loading continued and was

additionally paused at 21.5 kips and 22 kips to record readings from the dial gages. At these loadings, small cracks continued to propagate within the UHPC region, but did not exceed widths of approximately 0.10 in.

- P = 23 kips:

At the nominal capacity of the specimen, the widths of the cracks surrounding the UHPC joint were as shown in Figure 118 and Figure 119.

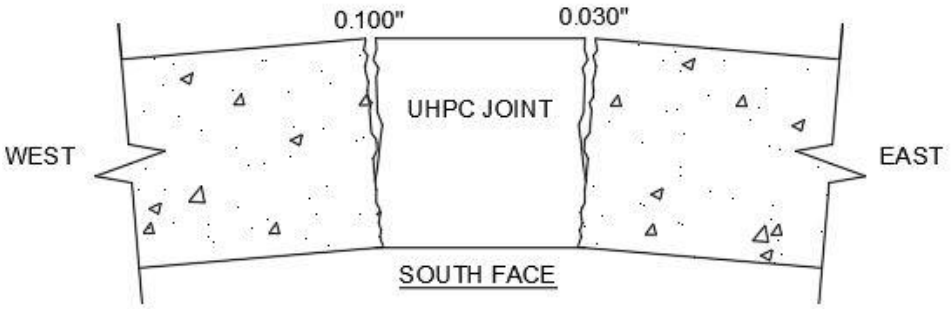

Figure 118. Schematic. Crack widths surrounding UHPC joint on south face of specimen at nominal capacity.

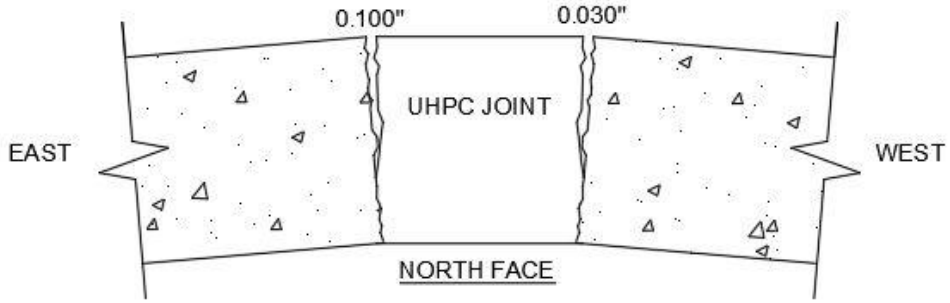

Figure 119. Schematic. Crack widths surrounding UHPC joint on north face of specimen at nominal capacity.

Also notable is the propagation of a diagonal shear crack away from the UHPC joint on the north face of the specimen, foreshadowing a compression strut failure of the precast concrete panels. An image of this crack is shown in Figure 120.

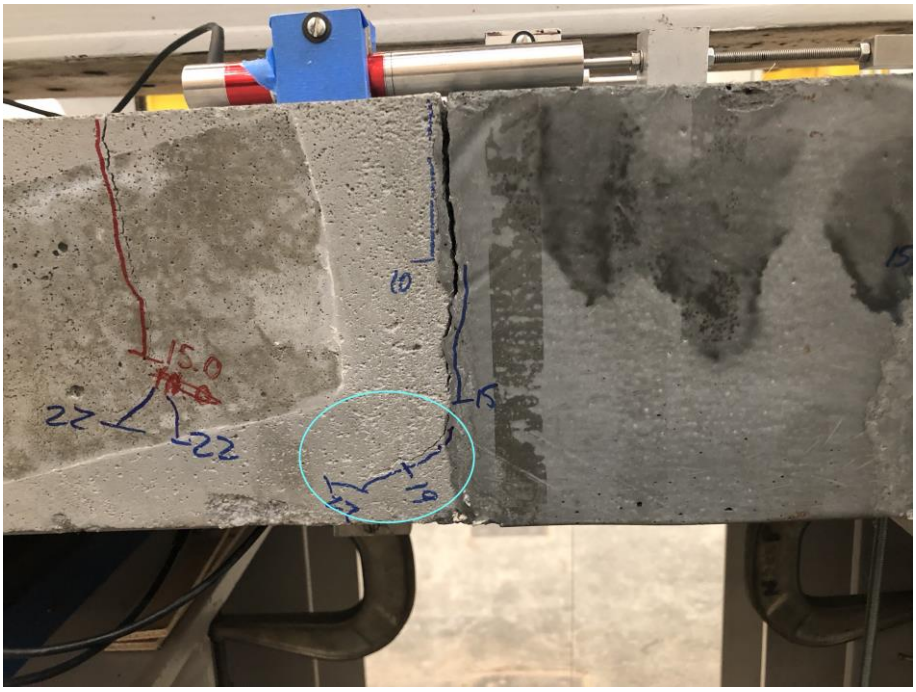

Figure 120. Photo. Diagonal cracking in concrete panel at nominal capacity of specimen.

- P = 25 kips:

The specimen failed at approximately 25 kips, exceeding its nominal capacity by about 8.7% (Figure 121). The failure of the specimen was characterized by crushing of the precast concrete panels near the west support, as shown in Figure 122.

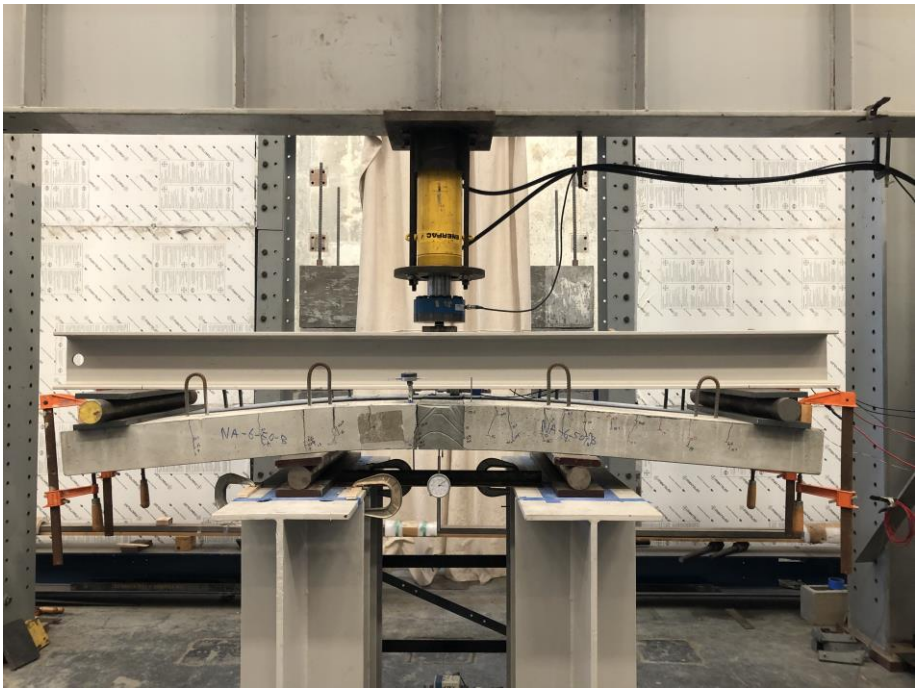

Figure 121. Photo. Specimen N-6-5.0-B at failure.

Figure 122. Photo. Crushing of precast concrete under west support.

The measurement of the final crack width of the largest crack at the concrete and UHPC interface is shown below. The crack was measured to be approximately 0.40 centimeters, or 0.157 in Figure 123.

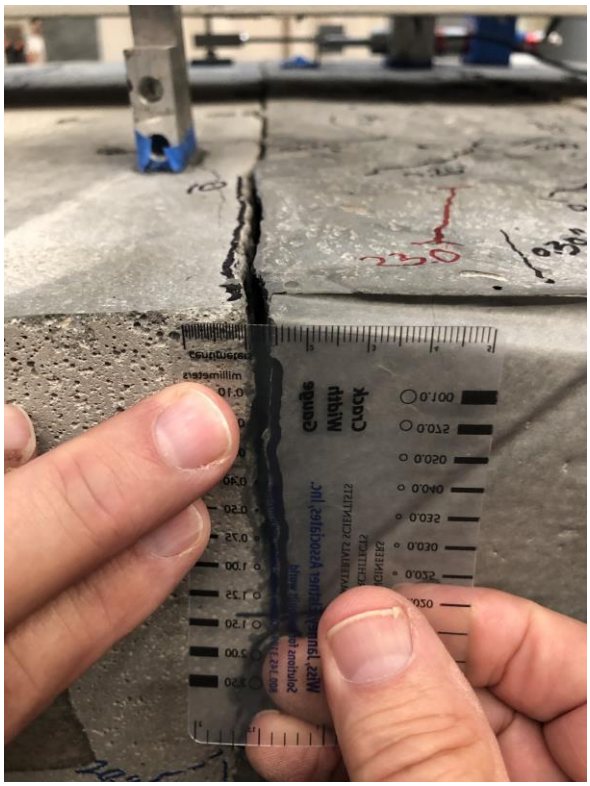

Figure 123. Photo. Measured crack width of crack at UHPC and precast concrete interface.

The UHPC joint did not experience crushing, and crack widths within the region were limited to minor widths compared to cracks in the precast panels The cracks that did occur did not propagate into the depth of the UHPC, as shown in Figure 124.

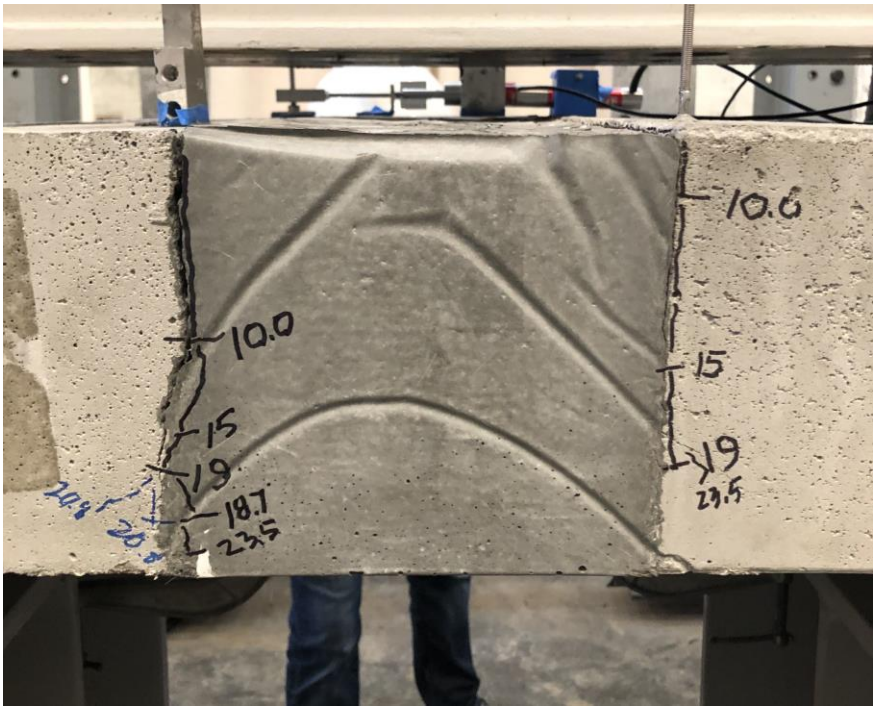

Figure 124. Photo. Closeup of UHPC joint at failure of the specimen.

It should be noted that while small in width, many diagonal cracks had formed on the surface of the UHPC joint. This crack pattern could indicate that there may have been torsional stresses added to the specimen during testing possibly due to the panels not being perfectly level during casting of the UHPC closure pour. These cracks could also have resulted from shear forces between the tension rebars caused by the bars being pulled in opposite directions. Arrows indicating the direction of the tension forces in the rebar have been added to Figure 125 below to help illustrate this concept.

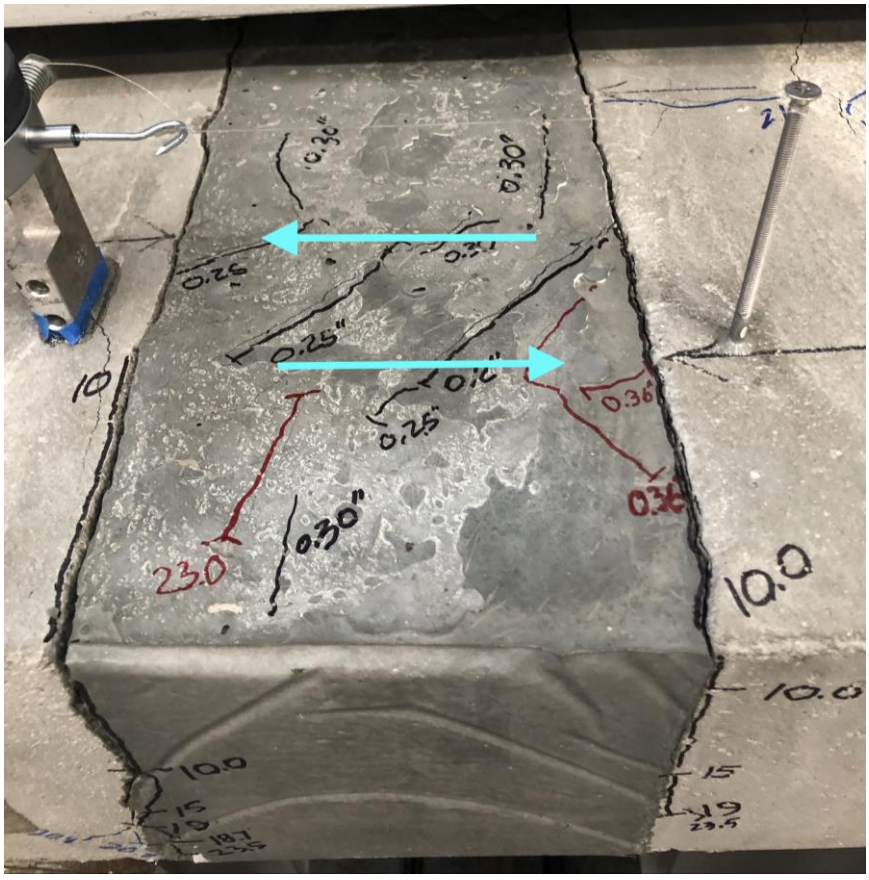

Figure 125. Photo. Close up of diagonal surface cracking within UHPC region.

There was no relative displacement between the UHPC joint and the precast concrete panels observed during testing. This shows that the UHPC was able to bond to the sand blasted surface of the precast panels without forming a cold joint that may have been susceptible to slip.

Results

Table 40 shows the results from the displacement measurements that were taken during the testing of N-6-5.0-B when loading was paused to observe cracking. It can be observed that most of the midspan deflection in the specimen occurred after the applied load had reached 18 kips.

Table 40. Load vs displacement readings for specimen N-6-5.0-B.

Load (kip)	Midspan Dial Gage Reading (in)	Midspan Vertical Deflection (in)	Linear Joint Deflection (in)
1.0	3.520	0.000	0.000
6.5	3.591	-0.071	0.000
10.0	3.561	-0.041	0.000
15.0	3.531	-0.011	0.005
18.1	3.452	0.068	0.025
18.9	3.414	0.106	0.038
19.7	3.378	0.142	0.050
20.7	3.378	0.142	0.050
21.5	3.291	0.229	0.089
22.0	3.243	0.277	0.113
23.0	3.192	0.328	0.142

Using the recordings of the applied loads from the load cell and the midspan deflection readings from the string potentiometer, force-displacement curves were plotted for the specimen. By observation of the experimental data, the values of P_{cr}, P_y, and P_n were determined and are labeled, shown in Figure 126. The force-displacement curves show that the predicted load at cracking of P_{cr} = 6.4 kips and was accurately represented by the data. The loads for P_y were lower than the predicted value of P_y = 21.99 kips. This lower-than-expected yield load results in a reduced amount of work done by the specimen during testing than predicted. The nominal load of P_n = 22.98 kips was confirmed to be exceeded by specimen NA-6-5.0-B by about 7.9% The nominal load of N-6-5.0-B was reached at a midspan displacement of 0.52 in.

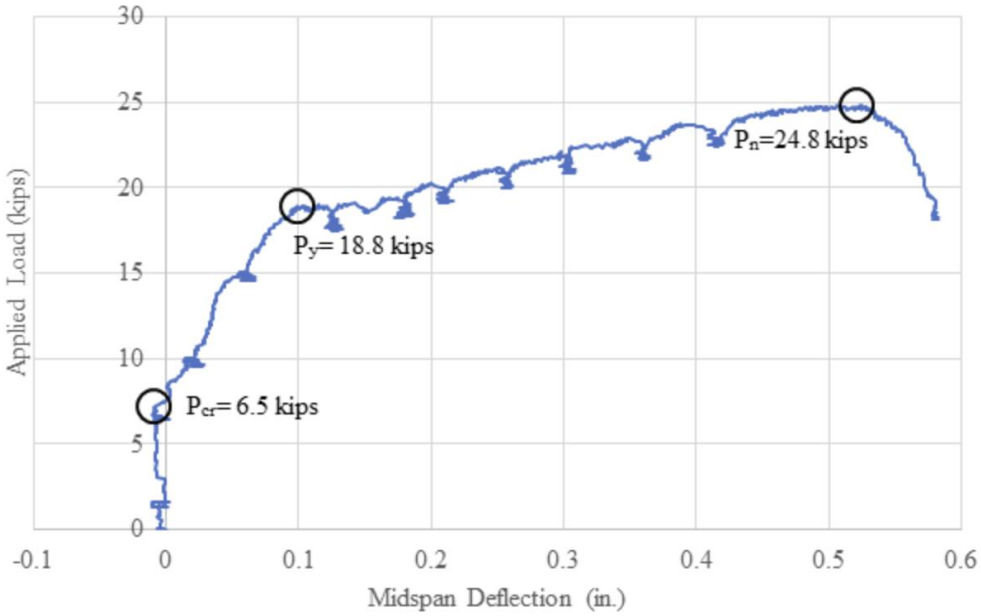

Figure 126. Force displacement curve for Specimen N-6-5.0-B.

TEST N-6-5.75-B

The fourth structural experiment was conducted on a 6-in. deep specimen with a 5.75-in. embedment length and no key geometry. This was the second test of this type, as N-6-5.75-A identical.

Setup

The setup for this experiment was identical to the previous, except for one difference. The specimen was not perfectly cast level and therefore rocked on the supports. The specimen was leveled using a high strength gypsum cement to fill any voids between the bottom of the specimen and the steel supports. This extra step was requisite to decrease the effects of torsional stresses during testing. Figure 127 demonstrates a ¼ in. gap between a corner of specimen N-5-6.75-B and the steel support.

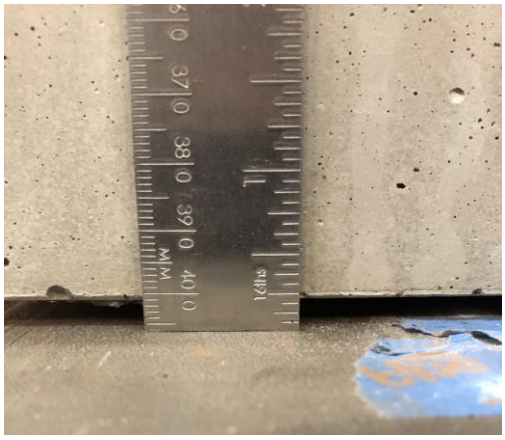

Figure 127. Photo. Underside of specimen N-6-5.75-B showing space between concrete and support.

To ensure a full contact patch between the specimen and the supports, a batch of USG Hydrostone was mixed with a 4:1 ratio of Hydrostone to water to create a putty-like plaster. The specimen was picked up off the supports and a debonding agent was applied to the supports to avoid the plaster sticking to the steel. The plaster was spread along the support, then the specimen was placed back down onto the supports, allowing the plaster to fill the gap and harden with the specimen atop it to stop the specimen from wobbling (Figure 128 and Figure 129).

Figure 128. Photo. Underside of specimen N-6-5.75-B with Hydrostone.

Figure 129. Photo. Closeup of ¼ in. gap filled with Hydrostone.

It must be noted that while the specimen was lifted off the supports using a forklift to apply the Hydrostone, the spreader beam was accidentally pinned against the load cell, causing the specimen to crack above the forklift forks. These cracks were measured to be <0.005 in. in width. Cracks were marked and labelled “pre” to indicate that the cracks took place before the testing occurred (Figure 130). It is not known exactly how much force was applied to the spreader beam to cause the specimen to crack. However, the depth of the most severe cracks was measured to be about 4.25 in., comparable to the depth of cracks caused by a measured load of approximately 10 kips in previously tested specimens (Figure 131). One small crack also appeared at the UHPC/concrete interface on the tension side of the specimen but did not propagate a significant amount into the depth of the specimen (Figure 132). It is possible that this crack is due to shrinkage and was only observed due to increased scrutiny.

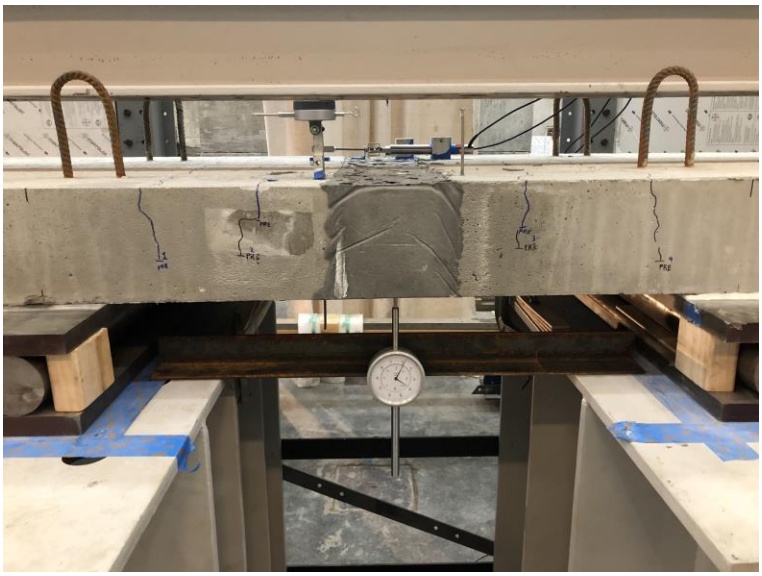

Figure 130. Photo. Locations of pre-test cracks on south face of specimen.

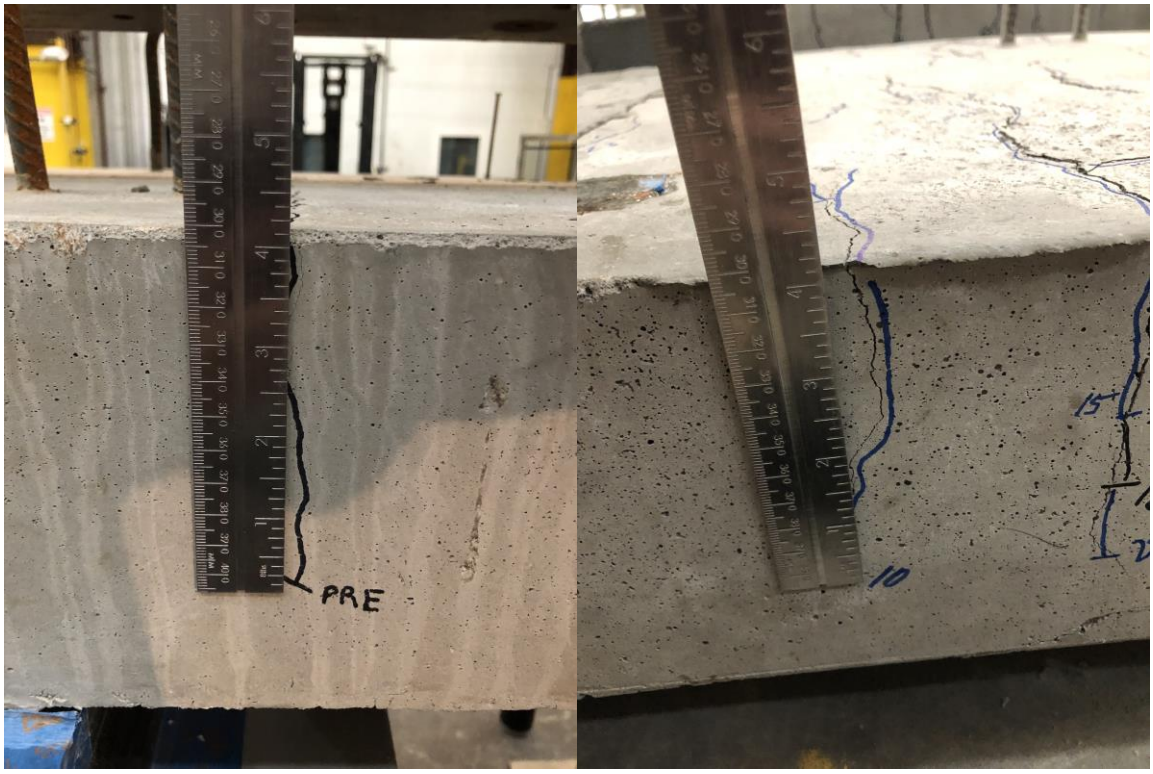

Figure 131. Photo. Comparison of pre-test crack depth on specimen N-6-5.75-B with depth of P = 10 kip crack on specimen N-6-5.0-B.

Figure 132. Photo. Pre-test crack at UHPC and precast concrete interface.

Once all pre-test cracks had been marked and labelled and the specimen was stable on the supports, the testing procedure was followed as normal. It was assumed that the reinforcing steel in the specimen had not been damaged.

Observations

The following observations were made at the pausing of the loads noted:

- P = 6.5 kips:

The loading was first paused at 6.5 kips to observe the specimen at its cracking moment. It was observed that cracks <0.005 in. in width had begun propagating over the supports similar to N-6-5.0B. It was also observed that the pre-test crack at the UHPC/concrete interface had begun propagating into the depth of the specimen but was still <0.005 in. in width.

- P = 10 kips:

Loading continued and paused at roughly 10 kips. At this point, the cracks between the supports began widening to >0.005 in. to where their more exact width could be measured with a crack card. Cracks at the concrete and UHPC interface also became more apparent, appearing on all four corners of the UHPC joint. These cracks near the interface were measured to be approximately 0.007 in. wide at this loading and were continually monitored throughout testing. It was observed that two larger cracks in the concrete panels had formed approximately 3 - 3.5 in. away from the concrete and UHPC interfaces on either side of the UHPC joint. These cracks were measured to be approximately 0.009 in. wide at this loading. As loading continued, widths and locations of major cracks were monitored and recorded.

- P = 15 kips:

At 15 kips, the largest crack in the precast concrete panel was measured to be 0.013 in. The widest cracks at the UHPC and concrete interface had widened to be roughly equal to this width. Additional cracks in the concrete panel had also formed approximately 9 in. away from the UHPC and concrete interface on both the east and west sides of the UHPC joint. Notably, a tension crack appeared directly in the center of the UHPC joint at this loading, as shown in Figure 133 and Figure 134. This crack was measured to be <0.005 in. wide.

Figure 133. Photo. Locations of cracks within UHPC marked at 15 kips.

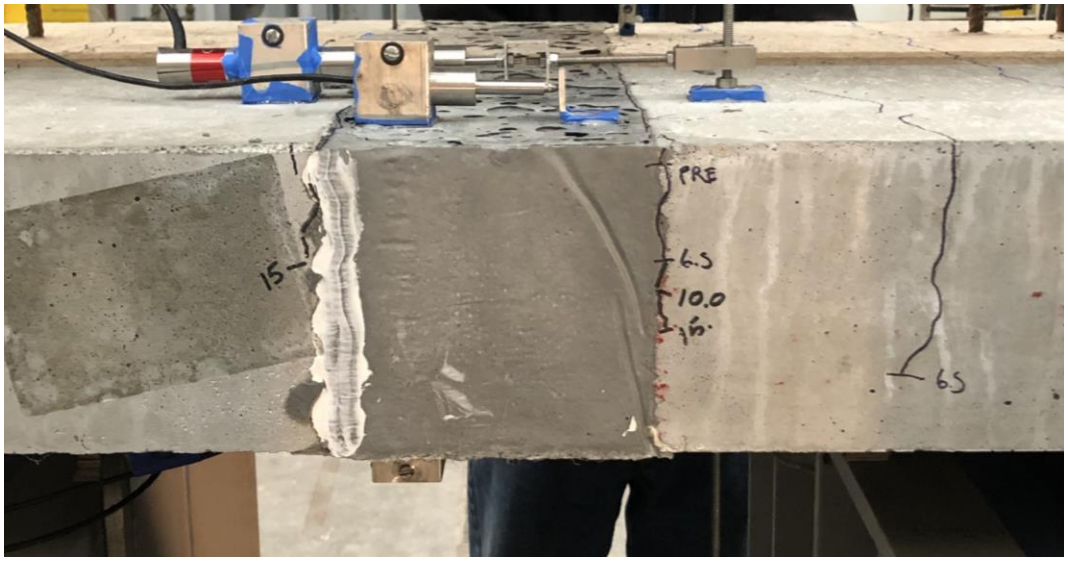

Figure 134. Photo. Cracks surrounding UHPC joint on north face at 15 kips.

- P = 18 kips:

At 18 kips, the load was paused before the load dropped to about 17.25 kips due to relaxation of the specimen. This relaxation may be due to yielding of the steel within the specimen at this loading. Once the load reading had stabilized, crack widths between the supports were measured and recorded, including the newly widening cracks that were observed approximately 9 in. east and west from the UHPC and concrete interface, as shown in Figure 135 and Figure 136.

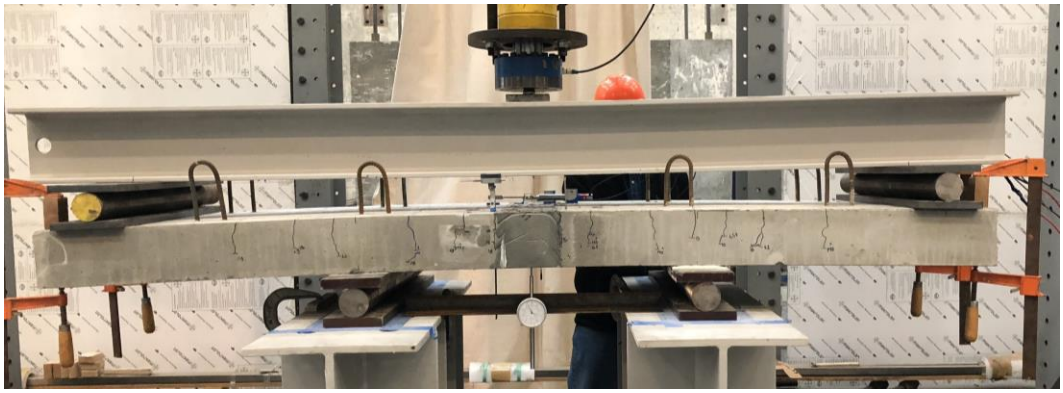

Figure 135. Photos. Specimen NA-6-5.75A at 18 kips showing locations of cracks.

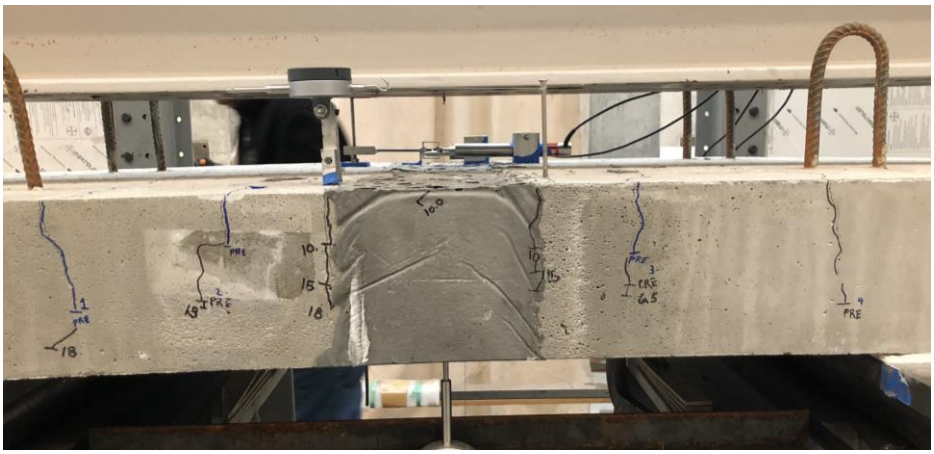

Figure 136. Photo. Closeup of crack locations between supports.

The approximate measured crack widths and locations on the specimen are shown more clearly in Figure 137 and Figure 138. Note that the figures do not represent actual propagation paths or depths of cracks.

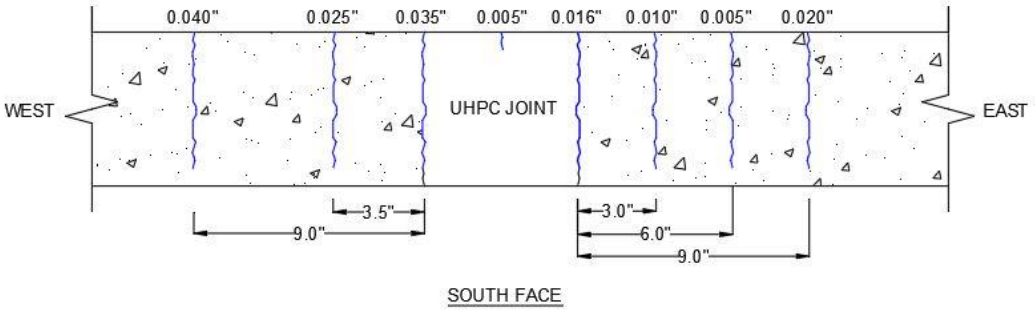

Figure 137. Photo. Locations and widths of cracks on south face of specimen at 18 kips.

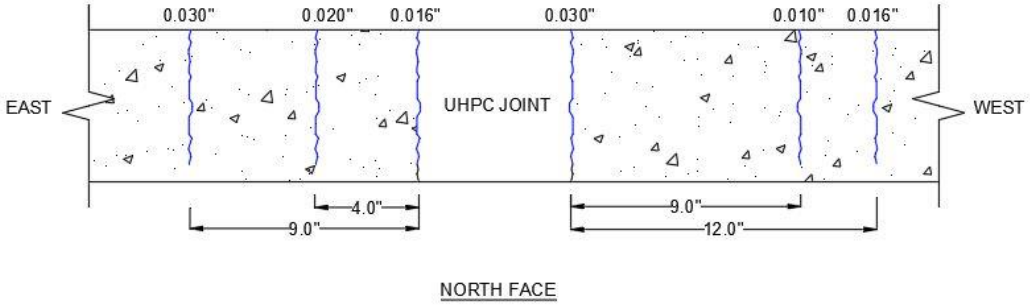

Figure 138. Photo. Locations and widths of cracks on north face of specimen at 18 kips.

After the load of 18 kips was reached, the specimen began deflecting more substantially due to yielding, causing the applied load to decrease from 17.25 kips to approximately 17 kips when the loading was paused at a string potentiometer reading of 0.17 in.

- P = 17 -20 kips:

Since the load applied began increasing at a slower rate relative to the rate of increasing midspan deflection measured by the string potentiometer, the points at which to pause

loading were determined from the string potentiometer readings from this point forward. Loading was paused when the string potentiometer reached readings of 0.20, 0.25, 0.35, and 0.45 in., corresponding to loads of 17.3, 17.6, 18.5, and 19.7 kips respectively. Cracks widths in the precast concrete panels were measured at each point the loading was paused. Notably, the crack widths in the panels and at the UHPC/concrete interface grew substantially during this load phase, while the tension crack width within the UHPC remained steady. At the load of 17.6 kips for instance, the largest crack in the precast concrete panels was measured to be 0.060 in. in width (an increase from the 0.40 in. crack appearing 9 in. to the west of the interface. The width of the crack in the UHPC region did not exceed 0.005 in. at this loading (Figure 139).

Figure 139. Photo. Close-up of tension crack in UHPC at a load of 17.6 kips.

It is interesting to note that as loading increased, cracks near the west support began propagating diagonally towards the center of the support as shown in Figure 140 indicating shear stresses above the support and foreshadowing a strut failure near the supports.

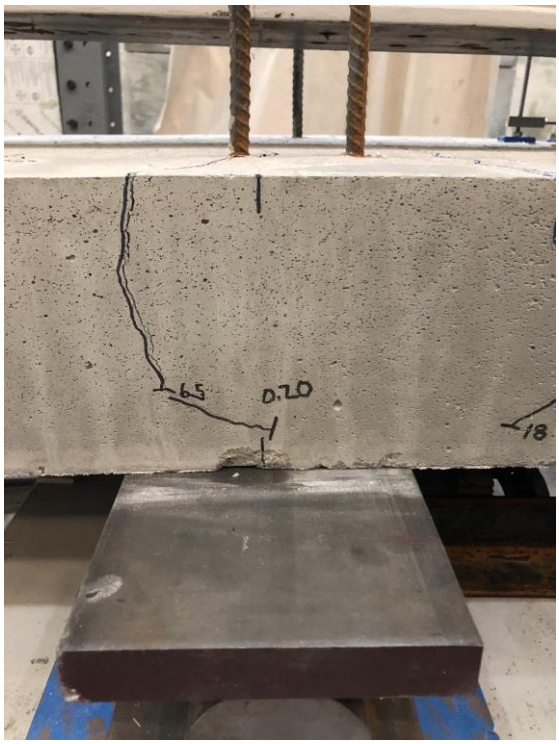

Figure 140. Photo. Diagonal shear crack near west support at a load of 17.3 kips.

- P = 21 kips:

After crack widths and readings from the dial gauges were recorded for each point noted above, loading was resumed from 19.7 kips and continued until failure of the specimen by crushing of the concrete near the supports. Crushing occurred at a maximum applied load of approximately 21 kips. This is short of the 23 kips that was expected, possibly due to damage to the specimen from the forklift. It should be noted that while the concrete experienced crushing near the supports, it was also observed to have crushed

against the UHPC joint, as shown in Figure 141. This provides a side-by-side indication of the high compressive strength of the UHPC relative to the concrete.

Figure 141. Photo. Concrete from precast concrete crushing under supports and against UHPC joint.

When observed at failure, the specimen showed relatively wider cracks at the concrete and UHPC interface and within the concrete panels than within the UHPC joint as shown in Figure 142.

Figure 142. Photo. Specimen cracking at failure.

In contrast, Figure 143 shows and thinner cracks of widths <0.005in. within the UHPC region at failure. These cracks were not observed to have propagated into the depth of the specimen – they only appeared on the tension surface of the UHPC joint. The final widths and locations of the prominent cracks in the specimen were measured and recorded at failure. The results from these measurements are depicted in Figure 144 and Figure 145.

Figure 143. Photo. Cracking in UHPC region at failure.

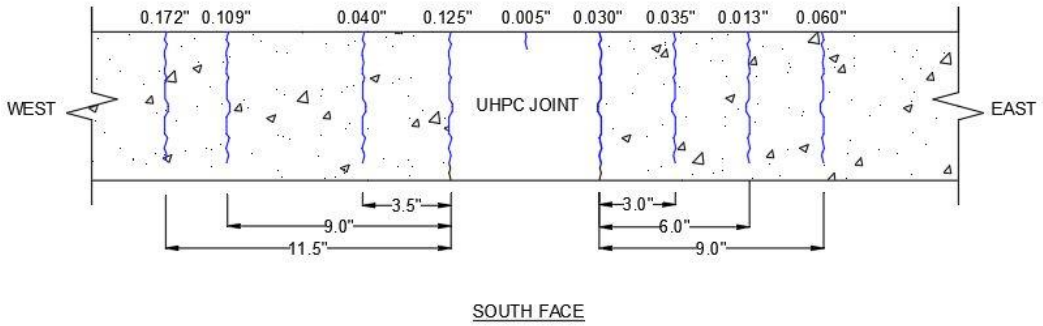

Figure 144. Schematic. Locations and widths of cracks on south face of specimen at 21 kips.

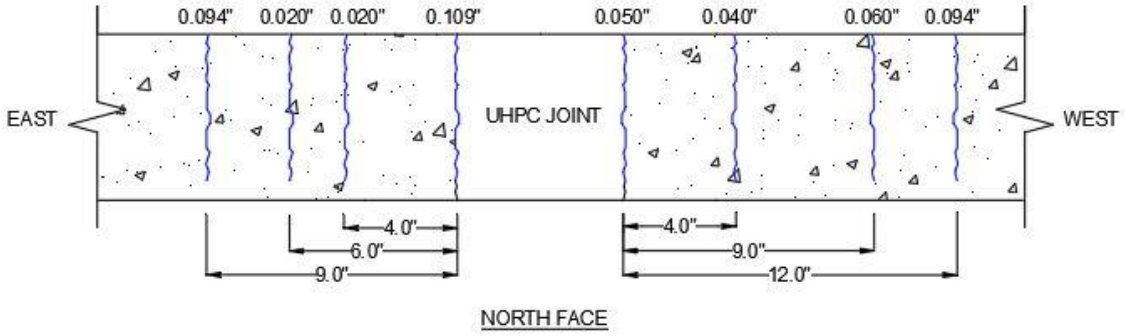

Figure 145. Schematic. Locations and widths of cracks on north face of specimen at 21 kips.

Results

Table 41 shows the results from the displacement measurements that were taken during the testing of N-6-5.75-B when loading was paused to observe cracking. Similar to N-6-5.0-B, most of the midspan deflection and the linear joint deflection occurs after the specimen was first subjected to a load of 18 kips, indicating this load as the specimen's approximate yield point.

Table 41. Load vs displacement readings for specimen N-6-5.75-B.

Load (kip)	Midspan Dial Gage Reading (in)	Midspan Vertical Deflection (in)	Linear Joint Deflection (in)
1.0	3.362	0.000	0.000
6.5	3.342	0.020	0.000
9.9	3.320	0.043	0.001
14.9	3.286	0.076	0.012
18.0	3.242	0.120	0.031
17.0	3.209	0.153	0.049
17.3	3.179	0.183	0.063
17.6	3.127	0.235	0.092
18.5	3.040	0.322	0.142
19.7	2.936	0.426	0.197
21.0	2.833	0.529	0.226

Using the recordings of the applied loads from the load cell and the midspan deflection readings from the string potentiometer, force-displacement curves were plotted for the specimen. By observation of the experimental data, the values of P_{cr}, P_y, and P_n were determined and are labeled, shown in Figure 146. The force-displacement curves show that the predicted load at cracking of P_{cr} = 6.4 kips and was accurately represented by the data. The loads for P_y were lower than the predicted value of P_y = 21.99 kips. This lower-than-expected yield load results in a reduced amount of work done by the specimen during testing than predicted and possibly due to damage to the specimen caused before testing. The nominal load of P_n = 22.98 kips was higher than specimen NA-6-5.7-B by about 8.2%. The nominal load of N-6-5.75-B was reached at a midspan displacement of 0.54 in.

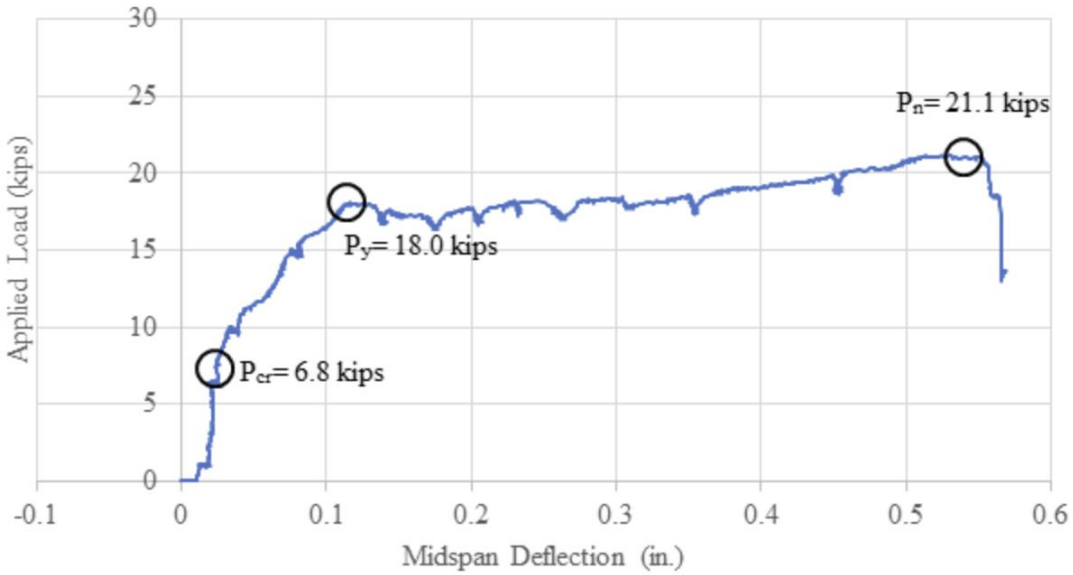

Figure 146. Force-displacement curve of N-6-5.75-B.

TEST G-9-5.0-A

The fifth structural experiment was conducted on a 9-in. deep specimen with a 5.0-in. embedment length and no key geometry. This was the second test of this specimen type, as G-6-5.0-A was used as a proof-of-concept to verify the experimental setup.

Setup

For testing the 9-in. deep. specimens, the same test setup, instrumentation, and loading procedure was used as in the previous experiment. Table 42 and Table 43 shows the predicted applied moments and experimental loads for cracking, yield, and nominal capacity of the 9 in. deep specimens. Calculations for the values are given in Appendix D.

Table 42. Predicted moments for test specimen sections.

Dimension *b* by *h* by *l* (in.)	Cracking Moment, M_{cr} (kip-ft)	Yield Moment, M_y (kip-ft)	Nominal Moment, M_n (kip-ft)
28 by 9 by 102	18.93	39.36	49.92

Table 43. Predicted applied loads for test specimen sections.

Dimension *b* by *h* by *l* (in.)	Load at Cracking, P_{cr} (kip)	Load at Yield, P_y (kip)	Load at Capacity, P_n (kip)
28 by 9 by 102	15.11	33.27	42.66

The key of one of the panels used to construct specimen G-9-5.0-A was damaged during shipment. The UHPC joint was cast as usual following procedures previously defined. Figure 147 and Figure 148 show the damage to the shear key, and the result of the UHPC consolidating into the joint in place of the damaged shear key.

Figure 147. Photo. Damage caused to shear key during shipping of panels.

Figure 148. Photo. UHPC cast around damaged shear key.

Observations

The following observations were made at the pausing of the loads noted:

- P = 10 - 15 kips:

The loading for specimen G-9-5.0-A was first paused at 10 kips. At 10 kips the specimen exhibited a small crack along the shear key of the damaged panel. This crack did not propagate into the UHPC that had filled the joint in place of the damaged shear key. Refer to Figure 149 for the location of this initial crack.

Figure 149. Photo. Crack near damaged shear key occurring at 10 kips of applied load.

The loading continued to the predicted cracking load of the specimen of 15 kips. At 15 kips, more cracks were exhibited between the supports, all equal to approximately 0.010 in. in width. Most of these cracks occurred within 6 in. of the supports, except for one crack occurring 9 in. away from the center of the UHPC joint. No cracks were observed within the UHPC joint at his loading.

- P = 20 kips:

At an approximate loading of 20 kips, cracks continued to deepen into the precast concrete panels near the supports (Figure 150). At this loading, the first crack appeared within the UHPC region itself. A tension crack 0.010 in. in width had formed near the

damaged shear key as shown in Figure 151.This crack was no more than 2 in. in length at the time of initial observation.

Figure 150. Photo. Researcher marking deepening cracks in the precast concrete panels at 20 kip load.

Figure 151. Photo. Crack within UHPC joint occurring at 20 kips of applied load.

It was also observed at this loading that a possible cold joint had formed between the non-sand blasted surfaces of the shear key and the UHPC. Small gaps had formed at the interface of the UHPC and the concrete panels along the shear key. This gap formation was closely monitored throughout the remainder of the test.

- P = 28 kips:

At a load of approximately 28 kips, the crack within the UHPC joint was observed to have widened slightly but had not increased in length. This observation contrasts with the adjacent cracks within the precast concrete panels, which had propagated across the top of the specimen by the time this loading was reached. The widest crack shown in Figure 152 was measured to approximately 0.040 in.

Figure 152. Photo. Cracks near UHPC joint propagating across the top of the specimen.

Note that one of the cracks shown in Figure 153 propagates under the mounting of the short gage LVDT. For this reason, the data collected from short gage LVDT on the tension side of the specimen was considered erroneous due to possible unsettlement of the mounting from the crack expansion.

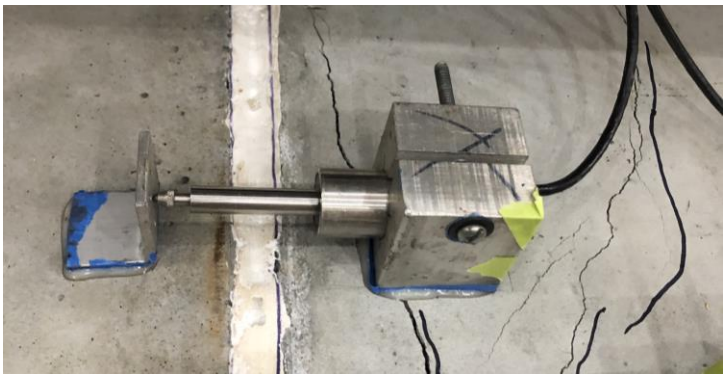

Figure 153. Photo. Crack forming under LVDT leading to erroneous data.

- P = 33 kips:

The loading was paused at the theoretical yield moment of the specimen. At this load, the widest crack in the specimen was observed to be along the damaged shear key. This crack shown was measured to be approximately 0.050 in. in width at this load. It should be noted that the wide cracks within the precast concrete do not propagate into the UHPC region, but rather propagate through the interface between the UHPC and concrete. The locations and widths of other the major cracks observed on the south-face of the specimen are shown in Figure 154. At this load, the deepest crack in the specimen was measured to have propagated to a depth of 1.5 in. away from the bottom of the specimen near the east support.

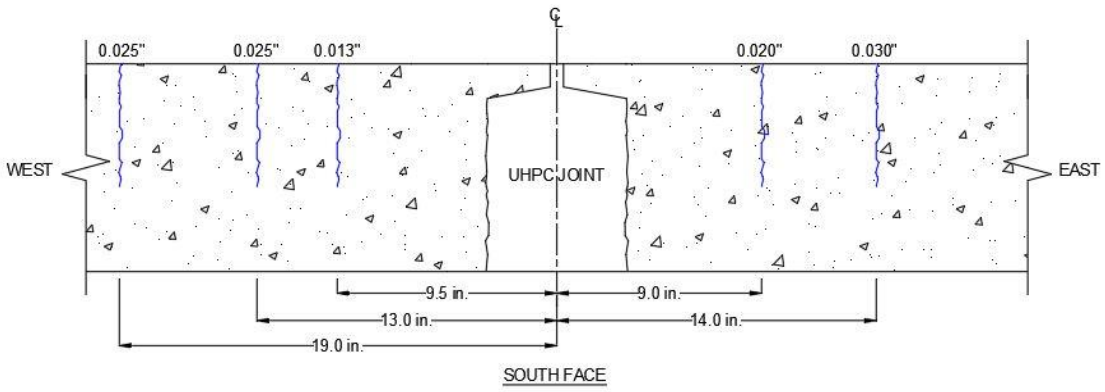

Figure 154. Schematic. Locations and widths of cracks on south face of specimen at 33 kips.

- P = 38 kips:

Interesting observations were made when the loading reached 38 kips. Firstly, the gap between the UHPC joint and shear key had continued to widen up to this loading. A substantial gap was observed on the south-face of the specimen between the shear key of the east panel and the UHPC joint. This may be indicative that there is no shear friction that can be developed between the joint and the unroughened surface of the shear key. The gap at 38 kips is shown in Figure 155.

Figure 155. Photo. Gap formation between precast concrete panel shear key and UHPC joint at 38 kips.

Additionally, horizontal cracks within the precast concrete panels appeared on the north face of the specimen at widths of 0.005 in. at the time of initial observation. These cracks were observed to have formed near the “compression” bars of the specimen. It should be noted that while calculating the nominal capacity of the specimen, the depth of the neutral axis was determined to be approximately 1.2 in. from the extreme compression fiber of the concrete, which would indicate that the “compression” bars would yield in tension near the nominal capacity of the specimen. Calculations for this conclusion are shown in Appendix D. Following this finding, a possible explanation for this observation could be that the “compression” bars experienced bond failure within the precast concrete causing the horizontal cracks that are shown in Figure 156. Another explanation is that the cracks formed due to transverse tension forces in the concrete cause by a compression strut formed between the supports and a point higher in the specimen at the

UHPC/concrete interface. Note that horizontal cracks occur above the theoretical neutral axis of 1.2 in. at failure, and above the measured neutral axis of 1.5 in. based on crack depth above the supports. It is possible that the cold joint formation between the UHPC and shear key caused a hinge effect at the interface, leading to a compression force concentration that is further above the extreme compression fiber than is the case above the supports. In either case, these horizontal cracks did not propagate through the UHPC. This is indicative of the high compression strength of the UHPC in comparison to the concrete, or in the former case, the ability of the UHPC to develop the rebars such that debonding failure occurs within the precast concrete panels before it occurs within the UHPC joint.

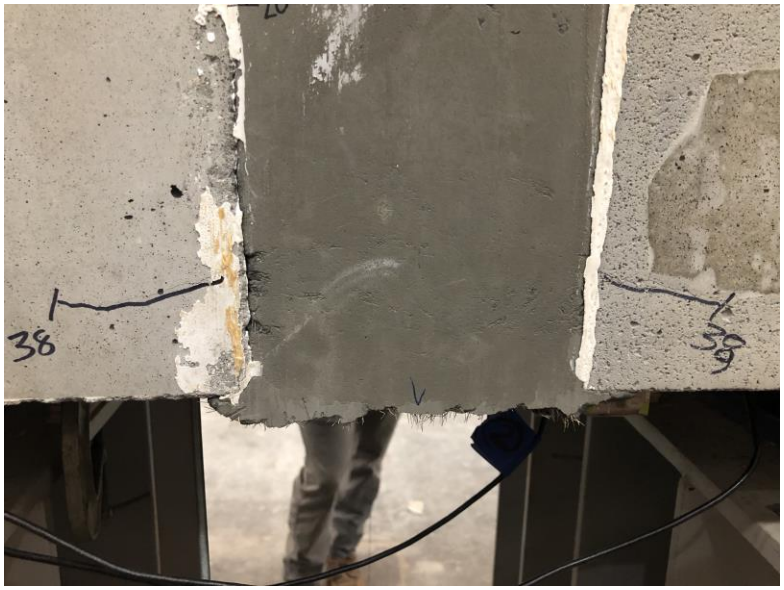

Figure 156. Photo. Horizontal cracking in precast concrete panels unmatched by the UHPC joint at 38 kips of applied load.

At 38 kips, the crack along the shear key of the damaged panel had widened to approximately 0.070 in. with no signs of the cracks propagating into the UHPC region. This crack at this loading is shown below in Figure 157.

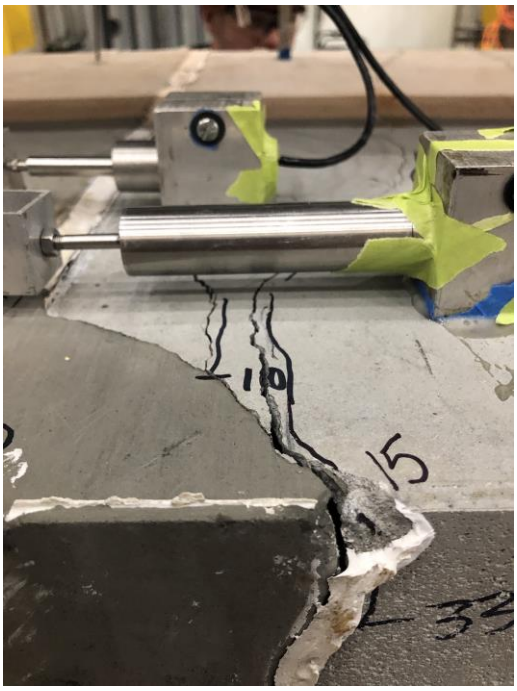

Figure 157. Photo. Large cracks along damaged shear key at 38 kips of applied load.

- P = 42 kips:

Specimen G-9-5.0-A was able to reach its predicted nominal capacity of 42.6 kips of applied load. Loading was paused at slightly above 42 kips to observe the specimen near its nominal capacity. The notable crack locations and widths on the south side of the specimen are shown in Figure 158.

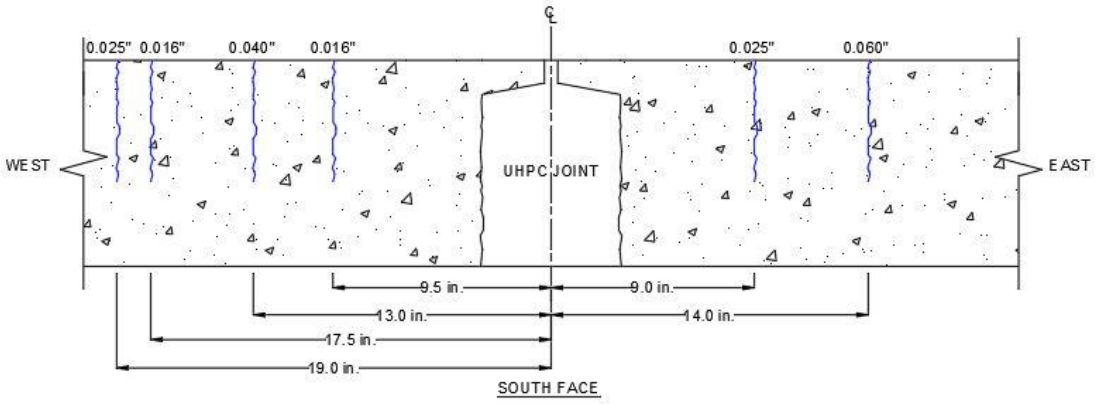

Figure 158. Locations and widths of cracks on south face of specimen at 42 kips.

Additionally, the crack along the damaged shear key was measured to be about nearly 0.125 in. In width at its widest point. The crack that had formed within the UHPC joint had widened to about 0.050 in. and had not been observed to have lengthened a significant amount.

- P = 52.5 kips:

At an approximate load of 52.5 kips, there were observed to be no changes in crack lengths from previous loadings. The width of the crack along the damaged shear key had widened to be approximately 5/32 in., and locations and widths of cracks on the south face of the specimen were recorded and are presented in Figure 159

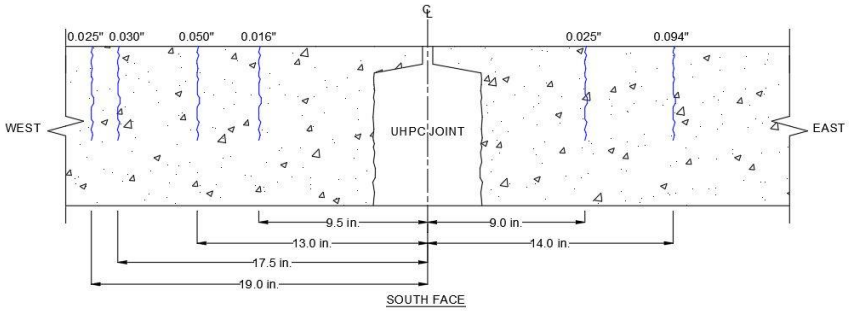

Figure 159. Schematic. Locations and widths of cracks on south face of specimen at 52.5 kips.

At this load, researchers decided to rely on midspan deflection readings rather than applied load to decide on when to pause loading since the specimen had already far exceeded its predicted nominal capacity. From this point, the loading was paused at midspan deflection readings of 0.267 in., 0.317 in., and 0.40 in., corresponding to approximate loadings of 54 kips, 58 kips, and 53 kips following a maximum applied load of 59.6 kips, respectively.

- P = 59.6 kips:

Specimen G-9-5.0-A experience failure by crushing of the precast concrete panels at a maximum applied load of approximately 59.6 kips. Crushing was not observed in the UHPC joint (Figure 160). This load is beyond the predicted nominal capacity of 42.66 kips by 39.7%. The final locations and widths of crack on the south face of the specimen at failure is shown in Figure 161.

Figure 160. Photo. Crushing of precast concrete panel against UHPC.

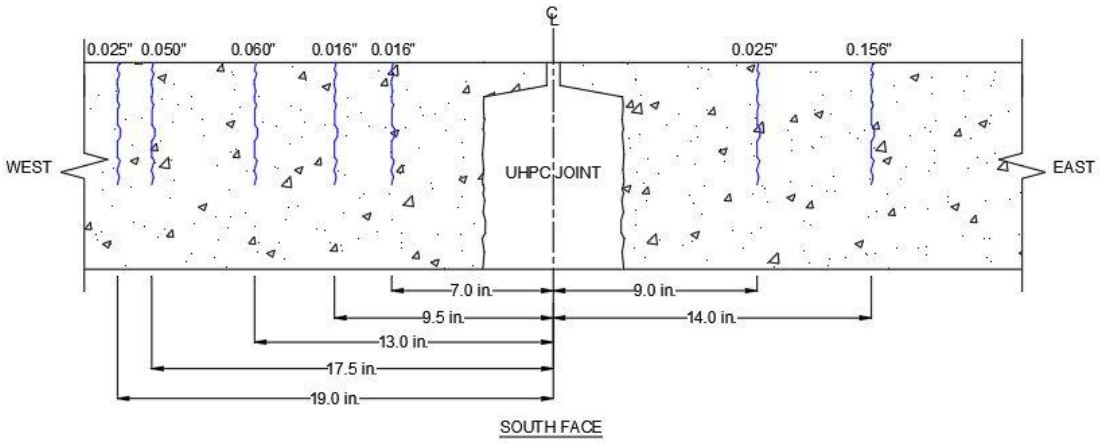

Figure 161. Schematic. Locations and widths of cracks on south face of specimen at 59.6 kips.

In addition to the cracks, the gap between the shear key and UHPC joint on the south face of the specimen was observed to have widened in the final stages of loading. This gap is shown in Figure 162 at 58 kips, where the gap was large enough for researchers to slide a crack card into. This gap caused a measured vertical displacement of 3/16 in. in the concrete panel from the UHPC.

Figure 162. Photo. Close-ups of large gap between shear key and UHPC joint caused by cold joint.

Figure 163 shows that on the north face of the specimen, the large cracks along the damaged shear key of the panel had widened to almost 3/8 in. In comparison, the crack within the UHPC region had widened to a width of 3/32 in. but had not been observed to have extended in length.

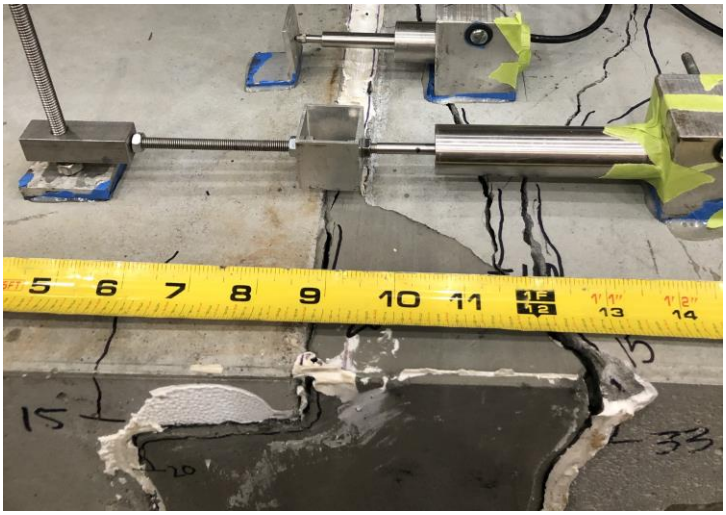

Figure 163. Photo. Large cracks along damaged shear key of precast concrete panel at failure.

Additional signs of debonding failure were also observed during this loading stage to failure. At 58 kips, horizontal cracks over the tension rebars were observed to have formed atop the precast concrete panels. These cracks were measured to be approximately 0.007 in. in width. Figure 164 and Figure 165 show closeups of these cracks that were observed on both the north and south sides of the specimen. No such cracks were observed to be in the UHPC region.

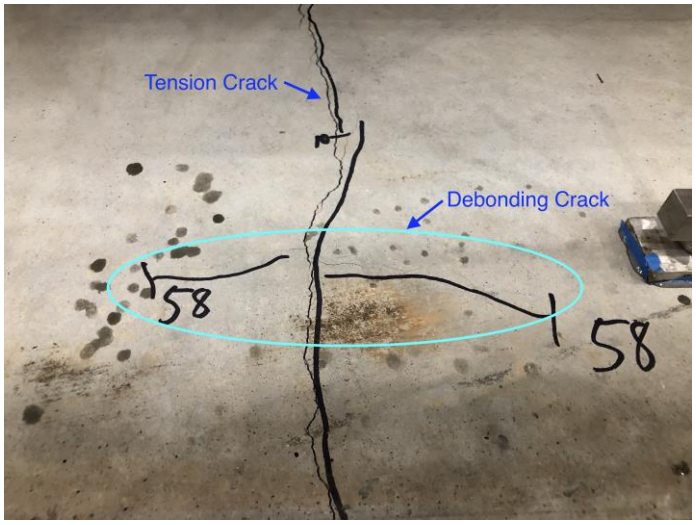

Figure 164. Photo. Debonding cracks on the north side of the specimen.

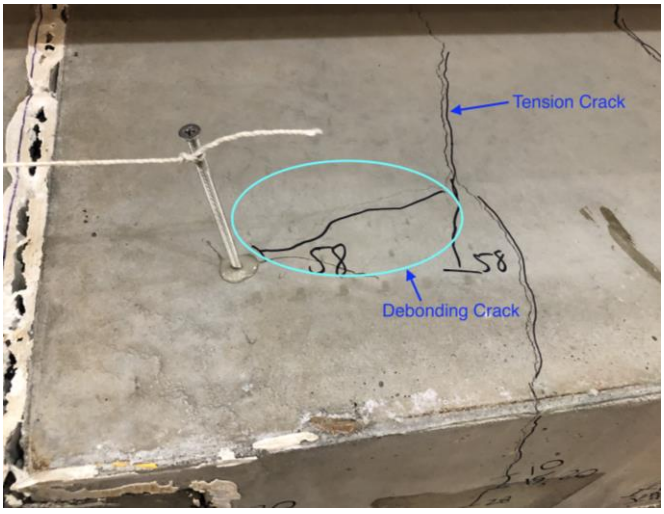

Figure 165. Photo. Debonding cracks on the south side of the specimen.

The horizontal cracks present were re-measured at failure. The horizontal crack on the left of the UHPC joint in Figure 166 was measured to be 0.025 in. wide, and the horizontal crack on the right of the UHPC joint was measured to be 0.030 in. Still, these cracks were not observed to have propagated through the UHPC joint.

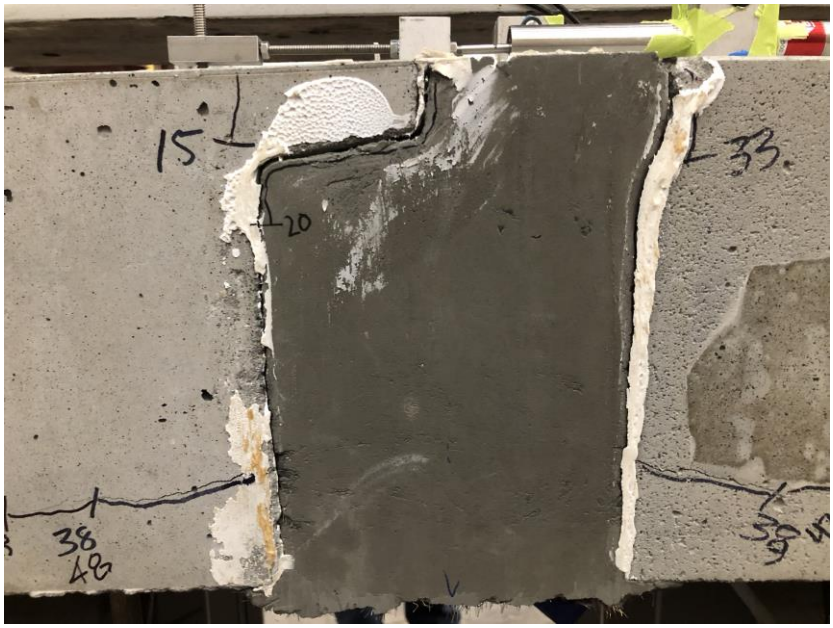

Figure 166. Photo. Horizontal cracking in precast concrete panels unmatched by the UHPC joint at 58 kips of applied load.

Results

Table 44 shows the results from the displacement measurements that were taken during the testing of G-9-5.0-A when loading was paused to observe cracking.

Table 44. Load vs displacement readings for specimen G-9-5.0-A.

Load (kip)	Midspan Dial Gage Reading	Midspan Vertical Deflection	Linear Joint Deflection
0.0	3.274	0.000	0.000
5.0	3.274	0.000	0.000
10.0	3.252	0.022	0.001
15.0	3.232	0.042	0.012
20.3	3.232	0.042	0.017
23.5	3.208	0.068	0.017
28.2	3.190	0.084	0.027
30.0	3.185	0.089	0.026
33.0	3.164	0.110	0.040
38.0	3.136	0.138	0.054
42.0	3.113	0.162	0.062
45.0	3.094	0.180	0.069
48.0	3.073	0.201	0.074
52.2	3.041	0.233	0.088
54.0	3.027	0.247	0.092
58.0	2.969	0.306	0.144
53.0	2.889	0.386	0.216

Figure 167 shows the force-displacement curves for the specimen G-9-5.0-A. As shown by the experimental data, the load at cracking for the 9 in. specimen can be more closely approximated as 10 kips rather than the predicted value of P_{cr} = 15.11 kips. Like the 6 in. specimens, both 9 in. specimens can be observed to yield at a load lower than the predicted P_y = 33.27 kips. P_n greatly exceeded the predicted values.

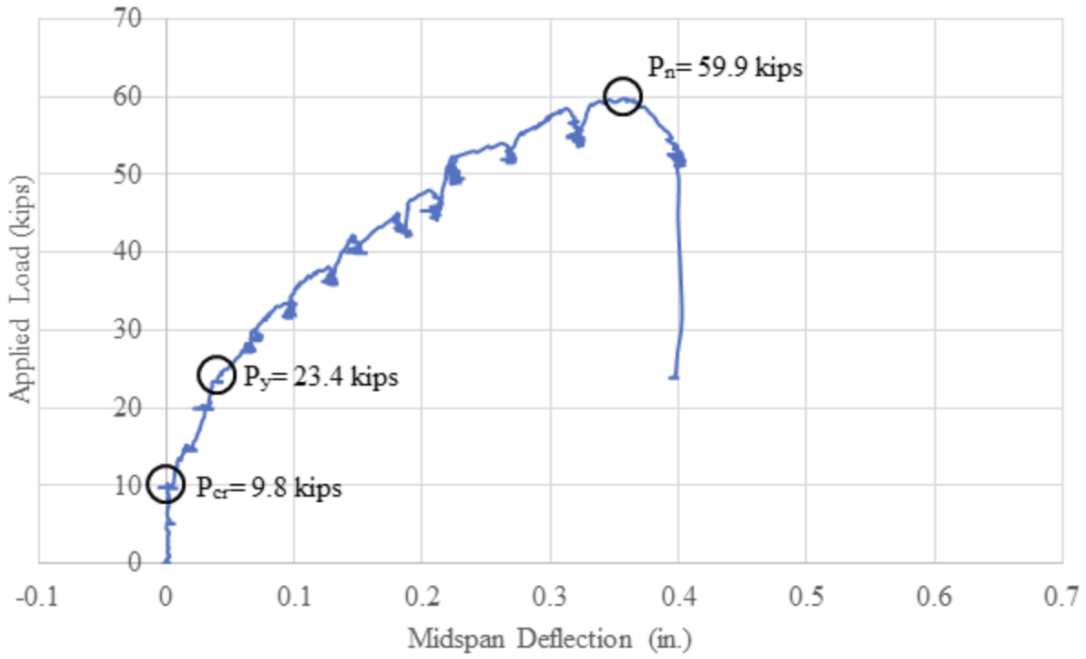

Figure 167. Force-displacement curve for specimen G-9-5.0-A.

TEST G-9-5.0-B

The final structural experiment was conducted on a second 9-in. deep specimen with a 5.0-in. embedment length and no key geometry.

Setup

For testing the 9-in. deep. specimens, the same test setup, instrumentation, and loading procedure was used as in the previous experiment.

It should be noted the UHPC closure pour was not immediately covered directly after casting to prevent moisture loss. This resulted in a shrinkage crack being formed along the precast concrete and UHPC interface within the UHPC region along the entire width of specimen G-9-5.0-B. This crack was measured to be approximately 0.010 in. in width and occurred on the compression side of the specimen. The approximate location of the crack is shown in Figure 168.

Figure 168. Photo. Location of shrinkage crack in specimen G-9-5.0-B.

Table 45 and Table 46 show the predicted applied moments and experimental loads for uncracked 9 in. deep specimens. Detailed calculations are shown in Appendix D.

Table 45. Predicted moments for test specimen sections.

Dimension *b* by *h* by *l* (in.)	Cracking Moment, M_{cr} (kip-ft)	Yield Moment, M_y (kip-ft)	Nominal Moment, M_n (kip-ft)
28 by 9 by 102	18.93	39.36	49.92

Table 46. Predicted applied loads for test specimen sections.

Dimension *b* by *h* by *l* (in.)	Load at Cracking, P_{cr} (kip)	Load at Yield, P_y (kip)	Load at Capacity, P_n (kip)
28 by 9 by 102	15.11	33.27	42.66

Observations

During testing, loads were initially applied in smaller increments than in previous tests due to uncertainty of the effect of the shrinkage crack.

- P = 5 – 15 kips:

Small cracks in the specimen were initially observed over the supports at a load of 7.5 kips. At 10 kips, these cracks had widened slightly, to a maximum width of 0.005 in. At the predicted cracking moment of 15 kips of applied load these cracks were approximately 0.010 in. in width. It was also observed that a crack had formed approximately 4.5 in. away from the center of the specimen on its south side. With increased load, this crack was diagonally propagating towards the UHPC and concrete interface and had reached the interface at 15 kips. There were no cracks in the UHPC at this loading.

- P = 24.5 kips:

From 15 kips, the load was increased by roughly 10 kips to a load of 24.5 kips. From 15 kips to 24.5 kips, the diagonally propagating crack on the south side of the specimen had begun propagating downwards along the UHPC and concrete interface, rather than continuing its diagonal path into the UHPC joint. At this load, the crack's maximum width was measured to be 0.060 in. On the north side of the specimen, a crack had likewise propagated from the shear key to along the UHPC and concrete interface. There were no signs of cracking within the UHPC joint at this load. Figure 169 and Figure 170 are photographs taken at larger loadings than 24.5 kips but provide the reader with information regarding the location and propagation paths of the cracks mentioned, of the south and north side, respectively.

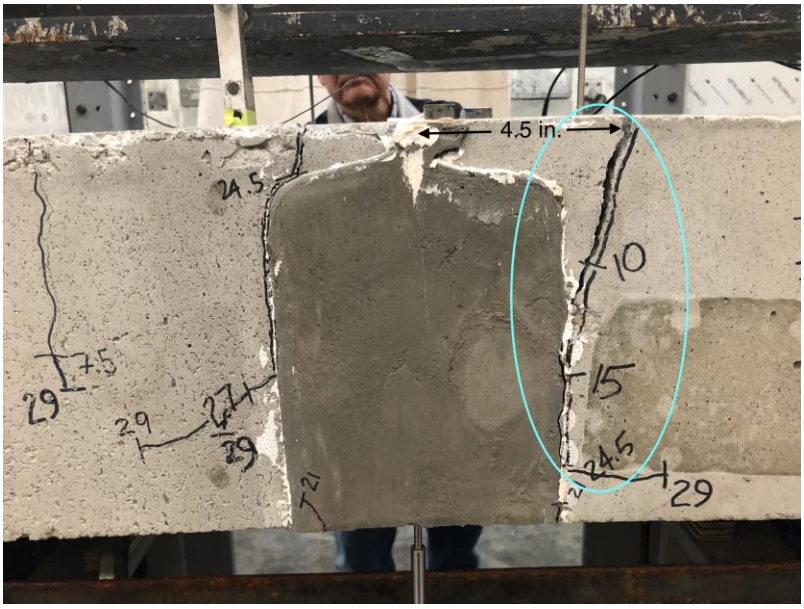

Figure 169. Photo. Cracking noted on south side of specimen.

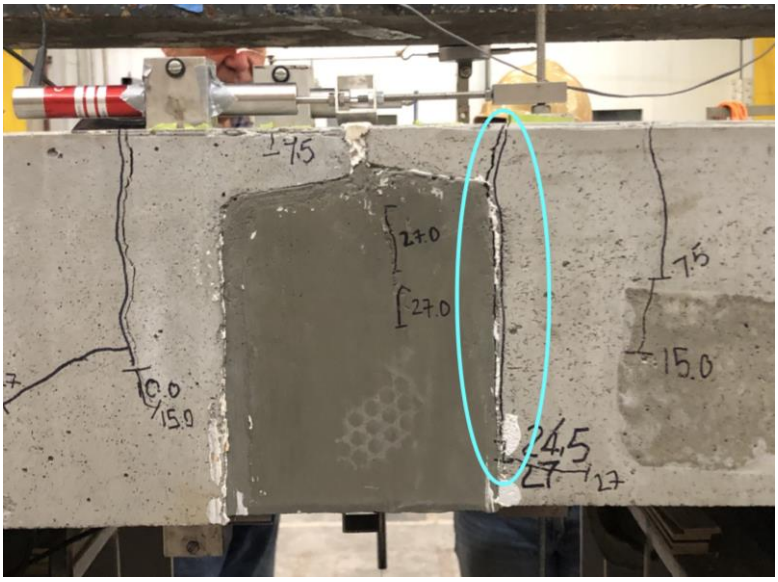

Figure 170. Photo. Cracking noted on north side of specimen.

- P = 27 kips:

At a load of 27 kips, the diagonal crack on the south side of the specimen shown in Figure 171 had widened to be 3/32 in. This crack continued propagating along the UHPC and concrete interface and not into the UHPC. Horizontal cracks were also observed on

the north side of the specimen. As shown in Figure 171 cracks had propagated from the tension cracks laterally towards the supports. Both cracks were measured to be <0.005 in. in width at the time of initial observation. It is interesting to note the difference in location of the cracks along the height of the specimen. The horizontal crack to the right of the UHPC joint is most likely a compression crack caused by transverse tension forces near the extreme compression fiber of the specimen. The horizontal crack to the left of the UHPC joint could be due to forces in the "compression" bars of the specimen, possibly leading to this sign of debonding failure within the precast concrete panel.

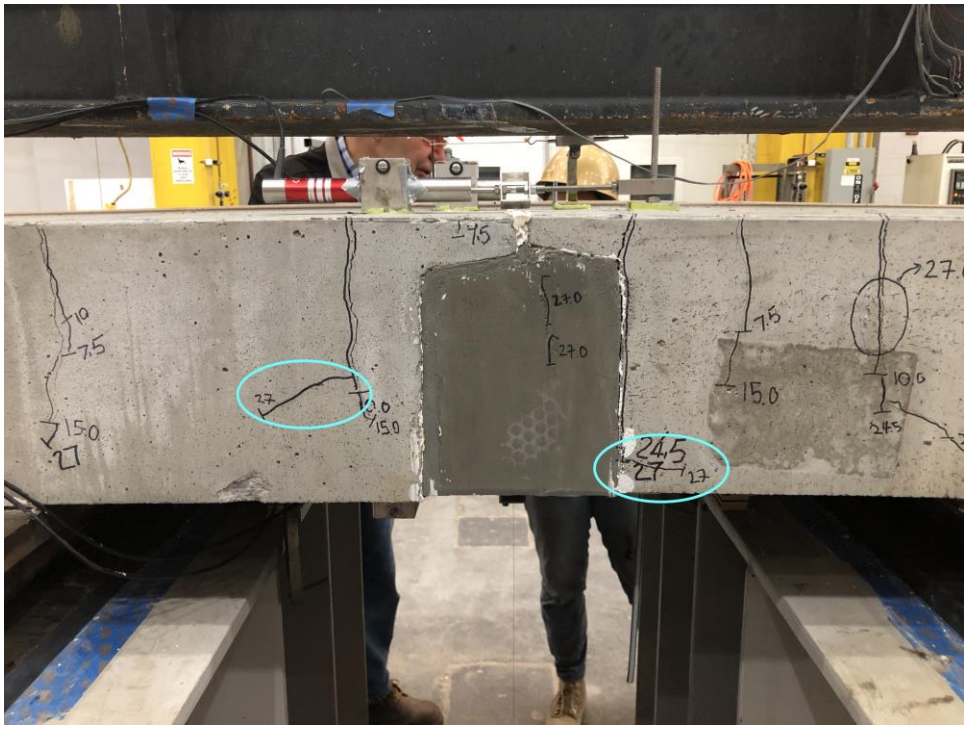

Figure 171. Photo. Horizontal cracks on north side at 27 kip load.

- P = 28.8 kips:

Loading was paused at more frequent intervals after 24.5 kips due to increased values of midspan deflection for corresponding loads as compared to specimen G-9-5.0-A. Loading was paused next at 28.8 kips, corresponding to an increase in midspan deflection of

approximately 0.05 in. from the previous load of 27 kips. At 28.8 kips (marked as 29 in the figures), the width of the large diagonal crack on the south side of the specimen was measured to have increased to 1/8 in. On the north side, the crack along the shear key of the panel was measured to be 3/32 in. in width, while the tension crack to the left of the UHPC joint had widened to 2/32 in. at its widest. Figure 172 is annotated with these measured widths in blue text to the right of the cracks they refer to for clarity.

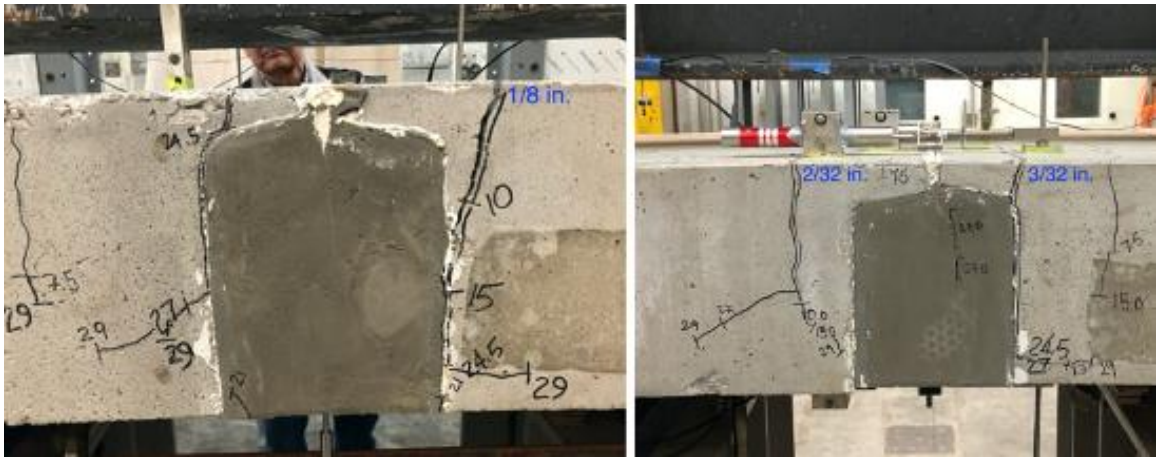

Figure 172. Photo. North (left) and south (right) side diagonal cracking at 28.8 kips.

Horizontal cracks were additionally observed to have formed on the south side of the specimen at this loading. A horizontal crack formed to the right of the UHPC joint neat the extreme compression fiber. To the left of the joint, a horizontal crack had propagated off the UHPC and concrete interface higher in the concrete panel. The horizontal cracks nearest to the extreme compression fiber on both the south and north sides were measured to be approximately 7/8 in. away from the bottom of the precast concrete panel.

- P = 30 kips:

Loading was paused from 28.8 kips until the midspan deflection had increased by an additional approximate 0.05 in. at a load of about 30 kips. The updated notable crack widths updated is given in Figure 173. At this load, there were also horizontal cracks observed on top of the precast concrete panels (Figure 174) similar to those observed in specimen G-9-5.0-A at 58 kips. These cracks may be indicative of bond failure with the tension reinforcement.

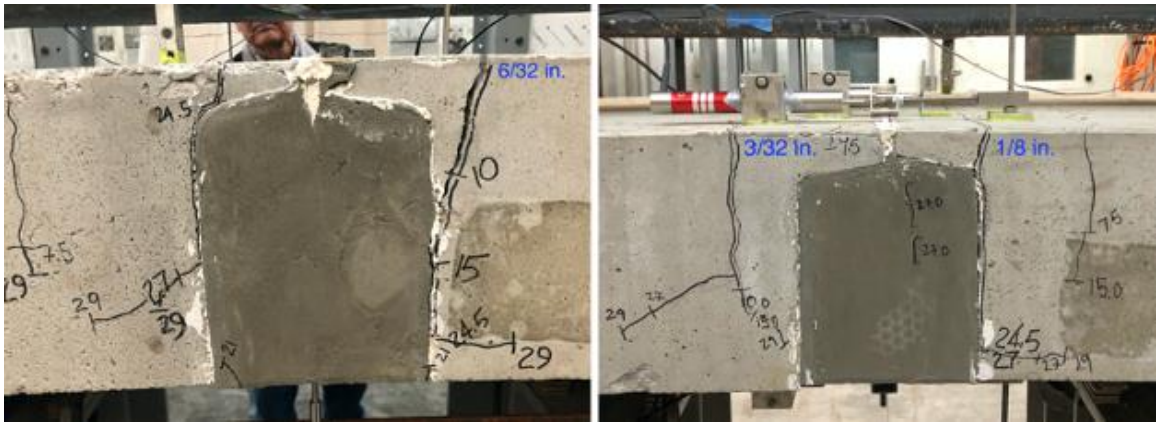

Figure 173. Photo. South (left) and north (right) side diagonal cracking at 30 kips.

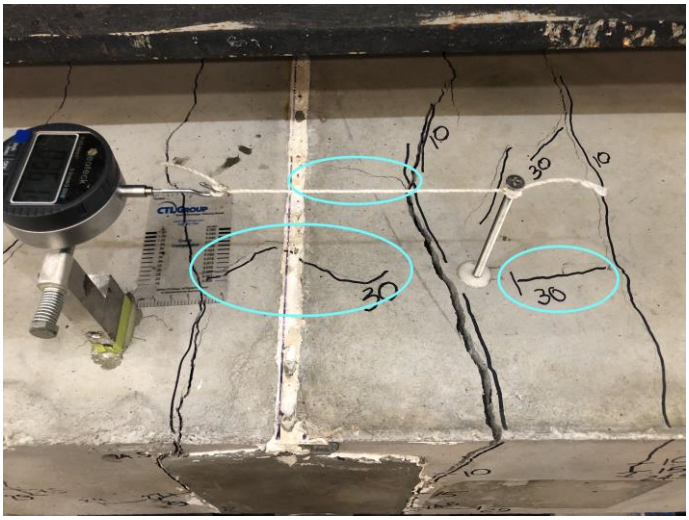

Figure 174. Photo. Horizontal cracking at 30 kips.

- P = 31.9 kips:

The specimen failed at a maximum applied load of 31.86 kips by means of crushing of the precast concrete panels against the UHPC joint as shown in Figure 175. The crushing was observed to have occurred mostly throughout the width of the specimen, indicating an even distribution of compression forces in the specimen due to the test setup. It can additionally be observed that the UHPC adjacent to the crushing precast concrete did not show any clear signs of crushing. The final crack widths that were tracked were once again measured and are reported in Figure 176 and Figure 177, for the north and south side, respectively.

Figure 175. Photo. Crushing on precast panel at failure.

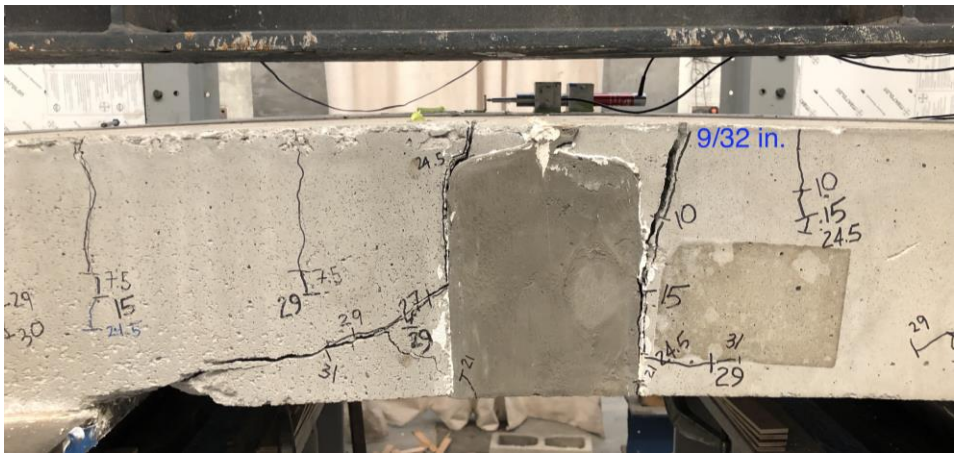

Figure 176. Photo. Cracking on south side at failure.

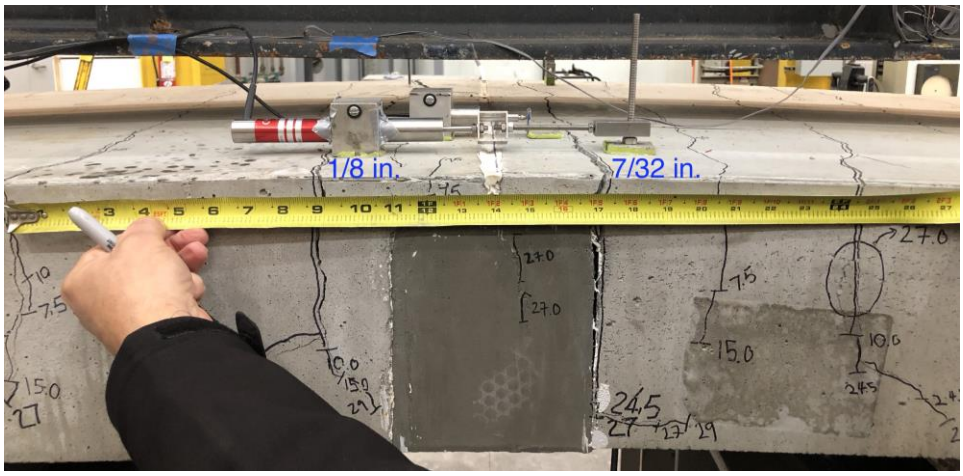

Figure 177. Photo. Cracking on north side at failure.

Figure 176 also shows that the diagonal crack to the left of the UHPC joint on the south face of the specimen had propagated all the way to the support, contributing to the crushing damage underneath the specimen. It is also important to note that while observing the crushing of the concrete underneath the specimen, researchers also noticed thin cracks along the “compression” bar markings of the specimen. These thin cracks propagated from the precast concrete and through the UHPC joint as shown in Figure 178 with red markings. These cracks are likely splitting cracks caused by forces within the rebars, indicating a bond failure between the concrete or UHPC with the “compression”

bars. As will be discussed below, this bond failure may be due to excessive compressive forces in the rebars caused by a lack of engagement of the concrete in compression following the shrinkage crack introduced.

Figure 178. Photo. Thin cracking in UHPC joints propagation from precast panels.

Results

Table 47 shows the results from the displacement measurements that were taken during the testing of G-9-5.0-B when loading was paused to observe cracking.

Table 47. Load vs displacement readings for specimen G-9-5.0-BA.

Load (kip)	Midspan Dial Gage Reading	Midspan Vertical Deflection	Linear Joint Deflection
0.0	3.274	0.000	0.000
5.0	3.274	0.000	0.000
10.0	3.252	0.022	0.001
15.0	3.232	0.042	0.012
20.3	3.232	0.042	0.017
23.5	3.208	0.068	0.017
28.2	3.190	0.084	0.027
30.0	3.185	0.089	0.026
33.0	3.164	0.110	0.040
38.0	3.136	0.138	0.054
42.0	3.113	0.162	0.062
45.0	3.094	0.180	0.069
48.0	3.073	0.201	0.074
52.2	3.041	0.233	0.088
54.0	3.027	0.247	0.092
58.0	2.969	0.306	0.144
53.0	2.889	0.386	0.216

Figure 179 and Figure 167 shows the force-displacement curves for the specimen G-9-5.0-B. As shown by the experimental data, the load at cracking for the 9 in. specimen can be more closely approximated as 10 kips rather than the predicted value of P_{cr} = 15.11 kips. Like the 6 in. specimens, both 9 in. specimens can be observed to yield at a load lower than the predicted P_y = 33.27 kips. Specimen G-9-5.0-B failed to reach the predicted nominal capacity of the 9 in. specimens. This lower-than-expected capacity is likely due to limited contributions of the concrete in compression due to a shrinkage crack along the concrete and UHPC interface.

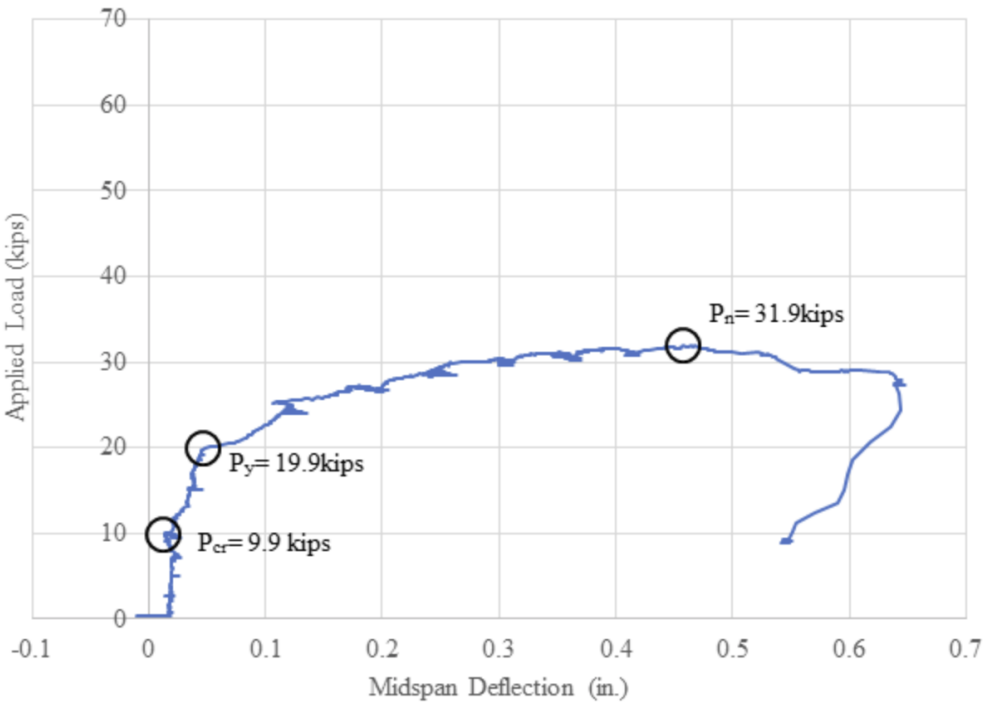

Figure 179. Force-displacement curve for G-9-5.0-B.

Discussion

The failure of the specimen occurred approximately 25.3% short of the expected applied load of 42.66 kips. The reduced capacity of this specimen is likely attributed to the large shrinkage crack in the specimen before it was loaded. While the depth of this shrinkage crack unknown, it is possible that the compression of the precast concrete near the crack in the joint was reduced or negligible in terms of its contribution to the specimen's flexural capacity. Before testing, it was assumed that the compressive forces in the concrete due to flexure would close the shrinkage crack at the UHPC and concrete interface during loading. This assumption contrasts with Figure 180 which shows that at failure the shrinkage crack had not reduced in width due to compression of the precast concrete against the UHPC of the specimen.

Figure 180. Photo. Shrinkage crack during loading.

Indeed, the majority of the crushing of the precast concrete occurred on the side of the UHPC joint opposite the side of the shrinkage crack, as shown in Figure 181. If the case is such that there were negligible compressive forces in the precast concrete panel near the shrinkage crack, then the compressive forces due to flexure would be taken entirely by the "compression" bars of the specimen. This may explain the slight damage to the precast concrete panel near top right most bar marking on the compression side of the specimen. If the section is reanalyzed completely neglecting contributions from the concrete in compression, then the nominal capacity of the specimen is calculated to be 27.9 kip-ft if assuming grade 80 bars. This moment corresponds to 23.1 kips applied load respectively, which is lower than the experimental capacity of 31.9 kips. However, if it is assumed that the shrinkage crack propagates 1.5 in. deep in the specimen, rendering

1.5 in. of precast concrete negligible in terms of the specimen's flexural capacity, then the predicted nominal moment of the specimen is 37.57 kip-ft, corresponding to an applied load of roughly 31.7 kips. A reduced contribution of the precast concrete in compression due to the shrinkage crack is thus a likely culprit for the reduced capacity of the specimen. The likely impact of this shrinkage crack highlights the importance of paying special attention to allow the UHPC joint to cure properly following casting to prevent as much moisture loss as possible.

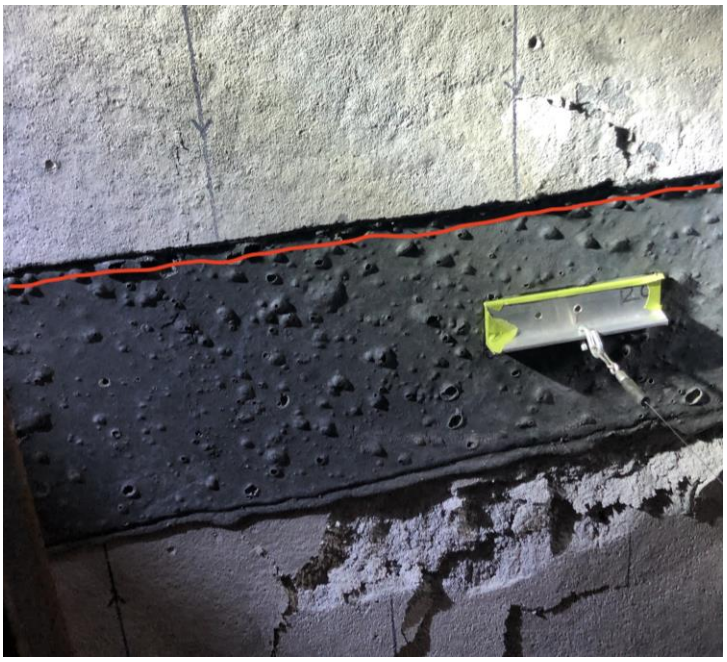

Figure 181. Photo. Concrete crushing on side opposite shrinkage crack.

CHAPTER 8. COST ESTIMATE

MATERIAL COST

To gauge the cost-effectiveness of the mix that was developed, the commercial price of each mix ingredient of the UHPC developed was acquired from the producers. These component prices are shown in Table 48. Based on these cost estimates, we can determine the cost estimate for the mix based per cubic yard of the material, as shown given in Table 49. This mix is estimated to cost $694.67.

Table 48. Component prices for estimating

Material	Price
Type I Portland Cement	$130 per ton
Fly Ash (both F and C)	$50 per ton
Metakaolin	$600 per ton
Masonry Sand	$15 per ton
HRWR	$13 per gallon
Steel Fibers	$4,000 per ton

Table 49. Material price estimates for GDOT UHPC per cubic yard

Material	Weight per yd^3 (lb)	Price per yd^3
Type I Portland Cement	1,248	$81.12
Class F Fly Ash	387	$9.68
Metakaolin	100	$30.00
Masonry Sand	1,997	$15.00
Superplasticizer	45	$29.67
Steel Fibers	264.6	$529.20
Total		$694.67

COMPARISONS TO PROPRIETARY UHPC

As of 2019, pre-bagged UHPC was selling for over $2,000 per cubic yard. Also, fibers cost between $250 and $500 per cubic yard. The cost of the developed GDOT UHPC is estimated to be approximately $700 per cubic yard. This corresponds to a material cost savings of nearly 70%.

CHAPTER 9. CONCLUSIONS AND RECOMMENDATIONS

This research developed a GDOT UHPC for use in bridge deck closure pours. The conclusions from the research are given below.

Material-scale study conclusions:

1. Some portion of fly ash remains unreacted in the mix. The replacement of fly ash with additional metakaolin should be avoided, however, due to issues with expansion that occur at higher metakaolin replacement levels.

2. The addition of accelerating admixtures can provide strengths above 21,000 psi, but higher dosages of accelerator reduce the late-age strength of the mix.

3. In order to ensure that the 18,000 psi compressive strength limit is reached, cement with a high C3S content should be used. While 52% C3S cement (Argos type I/II) was found to provide adequate strengths, a C3S content of 58% or above is recommended.

4. Particle packing optimization led to a sharp decrease in workability, to the mix's ultimate detriment. Packing is an important consideration, but it alone does not determine the suitability of a mix for use as UHPC for accelerated bridge construction.

Production-scale material study conclusions:

5. To generate a workable mixture that meets strength targets and can be produced in a reasonable amount of time, the dry ingredient stages of the mix should be completed at high speeds to aid in dispersion of the binder particles.

6. Metakaolin is superior to silica fume for use at the dosage levels required in the GDOT UHPC mix as it provides higher strengths and requires a shorter mixing duration.

7. Coarser sands such as the South Georgia river sand may be used in GDOT UHPC to great success. It is confirmed that both the masonry sand and the river sand from the South Georgia sand supplier can be used to mix UHPC.

8. The mix design for GDOT UHPC is as follows:

Table 50. Mix Design for GDOT UHPC.

Materials	Weight (pcy)	Ratio per Cement Weight
Type I Portland Cement	1248.0	1.00
Class F Fly ash	0387.0	0.31
Metakaolin	0100.0	0.08
Masonry sand	1997.0	1.60
HRWR	0025.7	0.02
Water	0303.0	0.24
Steel fibers	0264.6	0.21

Mechanical testing protocol conclusions:

9. Cubic specimen or cylinder specimen can be used to determine the compressive strength of the material. While the cubic specimen yields a slightly lower compressive strength, they may be more desirable due to their ease of testing (i.e., no grinding of ends). The specimen should have a 28-day compressive strength greater than 18,000 psi.

10. Small beam specimen flexural tests can be used in place of tensile tests. Both 2 in and 3 in square cross-sections are adequate for use. The 2 in specimens in this research effort had an average flexural strength of 2,895 psi. The 3 in specimens had and average flexural strength of 2,860 and 3,250 psi, dependent on curing conditions.

Structural evaluation conclusions:

11. The GDOT UHPC closure pour preformed as desired. The development length and lap length of the #5 bars in the UHPC joint in the slabs showed that those development lengths did develop the full, nominal moment capacity of the slabs. The failure of the specimen, in most cases, was due to crushing of the 6000-psi concrete; the top bars were at strains beyond their yield strain.

12. The cases where cracks were observed in the slab parallel to the tension bars indicate that the development of the tensile bars was beginning to fail in the 6,000 psi. Once again, the ultimate, “failure” of the specimen was due to the strength of the concrete deck and not due to the UHPC joint.

13. The experiment that was conducted on the specimen with the large shrinkage crack highlights the necessity for proper curing conditions, as this specimen saw a dramatic reduction in capacity.

APPENDIX A. MASONRY SAND SIEVE ANALYSIS

Table 51. Masonry sand sieve analysis data.

Sieve #	Aggregate Retained (g)	Aggregate Retained (%)	% Retained (cumulative)	Aggregate Passing (g)	Aggregate Passing (%)
4	0.00	0.00	0.00	326.29	100.00
8	0.07	0.02	0.02	326.22	99.98
16	3.43	1.05	1.07	322.79	98.93
30	33.49	10.26	11.34	289.30	88.66
50	141.65	43.41	54.75	147.65	45.25
100	122.51	37.55	92.30	25.14	7.70
200	24.02	7.36	99.66	1.12	0.34
Tray	1.12	0.34	100.00	0.00	0.00

APPENDIX B. COMPRESSIVE STRENGTH DATA

COMPRESSIVE STRENGTH TEST DATA OF 1F31K8

Table 52. Compressive strength test data for Batches 2 to 4.

Mix Name	**Batch 2**	**Batch 3**	**Batch 4**
Mix Date	7/20/20	8/10/20	8/17/20
3 Day Test Date	**7/23/20**	**8/13/20**	**8/20/20**
Results (ksi)	15.65 14.50 15.16	13.57 14.32 13.98	14.19 13.82 15.63
Mean (ksi)	15.10	13.95	14.55
Standard Deviation (ksi)	0.57	0.38	0.96
COV (%)	3.80	2.70	6.58

7 Day Test Date	**7/27/20**	**8/17/20**	**8/24/20**
Results (ksi)	15.71 17.16 16.63	14.76 16.80 16.08	15.91 16.94 17.22
Mean (ksi)	16.50	15.88	16.69
Standard Deviation (ksi)	0.73	1.03	0.69
COV (%)	4.44	6.50	4.12

28 Day Test Date	**8/17/20**	**9/7/20**	**9/14/20**
Results (ksi)	16.08 18.18 17.99	18.23 17.11 19.07	18.61 17.27 16.57
Mean (ksi)	17.42	18.14	17.48
Standard Deviation (ksi)	1.16	0.98	1.03
COV (%)	6.66	5.43	5.92

Table 53. Compressive strength test data for Batches 5, 6, and 8.

Mix Name	Batch 5	Batch 6	Batch 8
Mix Date	11/16/20	11/23/20	12/15/20
3 Day Test Date	**11/19/20**	**11/26/20**	**12/18/20**
Results (ksi)	14.58 12.36 14.87	13.67 14.11 14.61	13.83 13.69 13.32
Mean (ksi)	13.94	14.13	13.61
Standard Deviation (ksi)	1.38	0.47	0.26
COV (%)	9.88	3.31	1.91

7 Day Test Date	**11/23/20**	**11/30/20**	**12/22/20**
Results (ksi)	16.02 16.90 16.10	16.11 15.95 15.84	14.57 15.57 15.96
Mean (ksi)	16.34	15.97	15.37
Standard Deviation (ksi)	0.49	0.14	0.72
COV (%)	2.99	0.88	4.68

28 Day Test Date	**12/14/20**	**12/21/20**	**1/12/21**
Results (ksi)	18.64 19.27 18.56	19.71 19.29 18.87	16.93 17.66 17.35
Mean (ksi)	18.82	19.29	17.31
Standard Deviation (ksi)	0.39	0.42	0.37
COV (%)	2.08	2.19	2.13

Table 54. Compressive strength test data for Batches 9 to 11.

Mix Name	Batch 9	Batch 10	Batch 11
Mix Date	2/8/21	2/15/21	2/22/21
3 Day Test Date	**2/11/21**	**2/18/21**	**2/25/21**
Results (ksi)	14.19 14.10 13.75	14.51 15.01 13.81	15.33 15.43 15.37
Mean (ksi)	14.01	14.44	15.38
Standard Deviation (ksi)	0.23	0.60	0.05
COV (%)	1.65	4.17	0.35

7 Day Test Date	**2/15/21**	**2/22/21**	**3/1/21**
Results (ksi)	16.50 15.22 16.26	15.70 16.27 15.50	16.73 16.30 17.14
Mean (ksi)	16.00	15.82	16.73
Standard Deviation (ksi)	0.68	0.40	0.42
COV (%)	4.25	2.53	2.51

28 Day Test Date	**3/8/21**	**3/15/21**	**3/22/21**
Results (ksi)	19.71 19.09 19.39	18.94 19.40 19.00	19.85 20.45 19.59
Mean (ksi)	19.40	19.12	19.97
Standard Deviation (ksi)	0.31	0.25	0.44
COV (%)	1.58	1.29	2.19

COMPRESSIVE STRENGTH TEST DATA OF 1F24SF25

Table 55. Compressive strength test data for Batches 1 and 7.

Mix Name	**Batch 1**	**Batch 7**
Mix Date	7/13/20	12/11/20
3 Day Test Date	**7/16/20**	**12/14/20**
Results (ksi)	13.02 12.84 13.05	12.85 12.88 12.51
Mean (ksi)	12.97	12.75
Standard Deviation (ksi)	0.12	0.21
COV (%)	0.90	1.62
7 Day Test Date	**7/20/20**	**12/18/20**
Results (ksi)	12.62 14.59 13.89	14.92 14.23 14.35
Mean (ksi)	13.70	14.50
Standard Deviation (ksi)	1.00	0.37
COV (%)	7.32	2.55
28 Day Test Date	**8/10/20**	**1/8/21**
Results (ksi)	16.84 16.24 18.47	15.95 16.05 16.87
Mean (ksi)	17.18	16.29
Standard Deviation (ksi)	1.16	0.50
COV (%)	6.73	3.09

APPENDIX C. 6 IN DEEP PRECAST PANEL CALCULATIONS

Table 56. Panel Calculations for 6 in Deep Specimens.

Calculations for 6" thick specimens (28"x102"x6")

Material Properties

$f_y := 60ksi$ $E_s := 29000ksi$

$K_1 := 1.0$ $w_c := 0.15\frac{kip}{ft^3}$

$f'_c := 6ksi$ $E_c := 120000 \cdot K_1 \cdot \left(\frac{w_c}{\frac{kip}{ft^3}}\right)^2 \cdot \left(\frac{f'_c}{ksi}\right)^{0.33} \cdot ksi = 4.877 \times 10^6 psi$

$\lambda := 1$

Initial length, width, and thickness values

$b := 28in$ $l := 48in$ $h := 6in$ Dimension of one precast deck

$h \geq \frac{b}{20} = 1$ Minimum thickness satisfied ACI 7.3.1.1

$A_g := b \cdot h = 168\,in^2$ Gross area of precast concrete section

Volume of UHPC required (no lips, flat joint)

$A_{UHPC} := (h + 0.25in) \cdot 6in = 37.5\,in^2$

$V_{UHPC} := A_{UHPC} \cdot b = 1.05 \times 10^3\,in^3$ $\frac{V_{UHPC}}{1728in^3} = 0.608\,ft^3$

Use #5 bars top and bottom

$A_{bar} := 0.31in^2$ $d_{bar} := \frac{5}{8}in$ Area and diameter of #5 bar

$n_{top} := 4$ $n_{bot} := 4$ Number of top and bottom rebars

$A'_s := n_{top} \cdot A_{bar} = 1.24\,in^2$ Total area of top rebar

$A_s := n_{bot} \cdot A_{bar} = 1.24\,in^2$ Total area of bottom rebar

$A_{s.min} := \max(0.0018 \cdot A_g, 0.0014 \cdot A_g) = 0.302\,in^2$ Minimum area of flexural reinf. ACI Table 7.6.1.1

$A_{s.min} \leq A_s = 1$ Minimum area satisfied

$d_{cover} := 1in$ Cover of 1-inch from Haber & Graybeal

$d' := d_{cover} + \frac{d_{bar}}{2} = 1.313\,in$ Depth to top steel from compression fiber

$d := h - d_{cover} - \frac{d_{bar}}{2} = 4.687\,in$ Depth to bottom steel from compression fiber

$\varepsilon_{t.min} := 0.004$ Minimum tensile strain

$\varepsilon_{cu} := 0.003$ Ultimate concrete strain

$\rho := \frac{A_s}{b \cdot h} = 7.381 \times 10^{-3}$ Reinforcement ratio

Cracking strength

$f_r := 0.24 \cdot \lambda \cdot \sqrt{\frac{f'_c}{ksi}} \cdot ksi = 587.878\,psi$ Modulus of rupture (AASHTO 5.4.2.6)

$\varepsilon_{cr} := \frac{f_r}{E_c} = 1.205 \times 10^{-4}$ Concrete strain at rupture

$n := \frac{E_s}{E_c} = 5.946$

$c := \frac{(n-1) \cdot A'_s \cdot d' + (n-1) \cdot A_s \cdot d + A_g \cdot \frac{h}{2}}{A_g + (n-1) \cdot A'_s + (n-1) \cdot A_s} = 3\,in$ Centroid of section from the top

$I_g := \frac{1}{12} \cdot b \cdot h^3 + A_g \cdot \left(\frac{h}{2} - c\right)^2 \ldots = 538.931\,in^4$ Moment of inertia using transformed section

$+ (n-1) \cdot A'_s \cdot (d' - c)^2 \ldots$

$+ (n-1) \cdot A_s \cdot (d - c)^2$

$M_{cr} := \frac{f_r \cdot I_g}{h - c} = 8.801\,ft \cdot kip$ Cracking strength using transformed section

Yield Strength

$\varepsilon_y := 0.002$ Assume tensile steel yields and "compression" steel is in compression

$$f(c) := f_y \cdot A_s - \frac{\varepsilon_y}{d - c} \cdot (c - d') \cdot E_s \cdot A'_s - \frac{1}{2} \cdot \frac{\varepsilon_y \cdot c}{d - c} \cdot E_c \cdot c \cdot b$$ Force equilibrium

$c := 2\text{in}$

$c := \text{root}(f(c), c) = 1.344\,\text{in}$ Centroid of section at yielding

$$\varepsilon'_s := \begin{cases} \dfrac{\varepsilon_y}{d - c} \cdot (d' - c) & \text{if } c < d' \\ \left[\dfrac{\varepsilon_y}{d - c} \cdot (c - d')\right] & \text{if } c \geq d' \end{cases} = 1.864 \times 10^{-5}$$ Compression steel strain

$$M_y := f_y \cdot A_s \cdot \left(d - \frac{c}{3}\right) + \varepsilon'_s \cdot E_s \cdot A'_s \cdot \left(d' - \frac{c}{3}\right) = 26.334\,\text{ft} \cdot \text{kip}$$ Yield strength using triangular stress block

Ultimate Strength

Force equilibrium

$c_g := 1.0\text{in}$ Initial guess of c

$f_s := -f_y$ Bottom steel stress

$$\beta_1 := 0.85 - \frac{0.05 \cdot \left(\dfrac{f'_c}{\text{psi}} - 4000\right)}{1000} = 0.75$$ Beta from ACI Table 22.2.2.4.3

$$F(c_g) := E_s \cdot \left[\frac{\varepsilon_{cu}}{c_g} \cdot (c_g - d')\right] \cdot A'_s + f_s \cdot A_s \ldots + 0.85 \cdot f'_c \cdot (\beta_1 \cdot c_g \cdot b)$$ Sum of forces

$c := \text{root}(F(c_g), c_g) = 1.004\,\text{in}$ Centroid of section at ultimate moment, measured from the top surface

$$\varepsilon_t := \frac{\varepsilon_{cu}}{c} \cdot (d - c) = 0.011 \qquad \varepsilon_t \geq \varepsilon_{t.min} = 1$$

$$\varepsilon'_s := \frac{\varepsilon_{cu}}{c}\cdot(c - d') = -9.215 \times 10^{-4}$$

Top steel strain
("Top steel" is used to describe steel on the compression side)

$$TopTensComp := \begin{cases} \text{"Top steel in compression"} & \text{if } \varepsilon'_s > 0 \\ \text{"Top steel in tension"} & \text{if } \varepsilon'_s < 0 \end{cases} = \text{"Top steel in tension"}$$

$$f'_s := \begin{cases} E_s\cdot\varepsilon'_s & \text{if } TopTensComp = \text{"Top steel in compression"} \\ 0 & \text{otherwise} \end{cases}$$

$$f'_s = 0\,\text{psi}$$

Top steel stress - ignore if in tension

$$F(c_g) := f'_s\cdot A'_s + f_s\cdot A_s + 0.85\cdot f'_c\cdot(\beta_1\cdot c_g\cdot b)$$

Reiterate force equilibrium

$$c_g := \text{root}(F(c_g), c_g) = 0.695\,\text{in}$$

Centroid of section

$$\varepsilon_s := \frac{\varepsilon_{cu}}{c}\cdot(d - c) = 0.017$$

Bottom steel strain

$$\varepsilon_s \geq \varepsilon_y = 1$$

Bottom steel yielded

$$CompTransTens := \begin{cases} \text{"Compression-controlled"} & \text{if } \varepsilon_t \leq \varepsilon_y = \text{"Tension-controlled"} \\ \text{"Transition"} & \text{if } \varepsilon_y < \varepsilon_t < 0.005 \\ \text{"Tension-controlled"} & \text{if } \varepsilon_t \geq 0.005 \end{cases}$$

$$M_n := \left| f'_s\cdot A'_s\cdot\left(d' - \frac{\beta_1\cdot c}{2}\right) + f_s\cdot A_s\cdot\left(d - \frac{\beta_1\cdot c}{2}\right)\right| = 27.447\,\text{ft}\cdot\text{kip}$$

Nominal strength using Whitney stress block

Test Configuration - 4 point bending (negative)

$w_{sw} := w_c \cdot b \cdot h = 0.175\,klf$ — Distributed load due to self weight of specimen

$x := 27in$ — Distance between support and load

$L_{concrete} := 2 \cdot l + 6in = 102\,in$ — Total length of concrete panel being tested, including 6-in UHPC joint

$L_{support} := 36in$ — Distance between two supports

$M_{sw} := w_{sw} \cdot \frac{(x + 6in)^2}{2} = 0.662\,ft \cdot kip$ — Maximum moment due to self weight of specimen

$M_{test} := \left[48plf \cdot \left(\frac{9.625ft}{2}\right) + 150lbf + 35lbf\right] \cdot x$

$M_{test} = 0.936\,ft \cdot kip$ — Maximum moment due to test configuration: weight of load plates and spreader beam*

$M_{DC} := M_{sw} + M_{test} = 1.598\,ft \cdot kip$ — Maximum moment due to dead load

*Actuator load to reach cracking, yield, and ultimate flexural capacity***

$P_{cr} := \frac{M_{cr} - M_{DC}}{x} \cdot 2 = 6.403 \times 10^3\,lbf$ — Load to reach cracking strength

$P_{yield} := \frac{M_y - M_{DC}}{x} \cdot 2 = 2.199 \times 10^4\,lbf$ — Load to reach yield of tensile steel

$P_{u.F} := \frac{M_n - M_{DC}}{x} \cdot 2 = 2.298 \times 10^4\,lbf$ — Load to reach ultimate flexural capacity

*: 9.625-ft long W8x48 as spreader beam; steel plates and roller that transfer load from the spreader beam and actuator weigh 35 lbf and 150 lbf, respectively.

**: Actuator loads will be different when more accurate loads from plates and beam are considered

Shear strength calculations (negative bending)

$V_c := 2\lambda \cdot \sqrt{\frac{f_c}{psi}} \cdot psi \cdot b \cdot d = 2.033 \times 10^4 \, lbf$ Concrete shear strength

$V_{sw} := w_{sw} \cdot (x + 6in) = 481.25 \, lbf$ Maximum shear from self-weight

$V_{test} := 28plf \cdot \left(\frac{8ft}{2}\right) + 50lbf + 25lbf = 187 \, lbf$ Maximum shear from test configuration

$V_{DC} := V_{sw} + V_{test} = 668.25 \, lbf$ Maximum shear due to dead load

Actuator load to reach shear capacity

$P_{u.V} := \left(V_c - V_{DC}\right) \cdot 2 = 3.933 \times 10^4 \, lbf$ Load from actuator to cause shear failure

$$FailureMode := \begin{cases} \text{"Flexure"} & \text{if } \frac{P_{u.V}}{P_{u.F}} > 1 \\ \text{"Shear"} & \text{otherwise} \end{cases}$$

$FailureMode = \text{"Flexure"} \qquad \frac{P_{u.V}}{P_{u.F}} = 1.712$

APPENDIX D. 9 IN DEEP PRECAST PANEL CALCULATIONS

Table 57. Panel Calculations for 9 in Deep Specimens.

Material Properties

$f_y := 60ksi$ $E_s := 29000ksi$

$K_1 := 1.0$ $w_c := 0.15\frac{kip}{ft^3}$

$f'_c := 6ksi$ $E_c := 120000 \cdot K_1 \left(\frac{w_c}{\frac{kip}{ft^3}}\right)^2 \cdot \left(\frac{f'_c}{ksi}\right)^{0.33} ksi = 4.877 \times 10^6 \cdot psi$

$\lambda := 1.0$

Initial length, width, and thickness values

$b := 28in$ $l := 48in$ $h := 9in$ Dimension of one precast deck

$h \geq \frac{b}{20} = 1$ Minimum thickness satisfied ACI 7.3.1.1

$A_g := b \cdot h = 252 \cdot in^2$ Gross area of precast concrete section

Cracking Strength

$A'_s := 1.24in^2$ $d' := 2.9375in$ Area of top steel and depth to top steel from compression fiber

$A_s := 1.24in^2$ $d := 6.3125in$ Area of bottom steel and depth to bottom steel from compression fiber

$Method := "AASHTO"$

$$f_r := \begin{cases} \left(\left(0.24 \cdot \lambda \cdot \sqrt{\frac{f'_c}{ksi}} ksi\right)\right) \text{ if } Method = "AASHTO" = 587.878 \cdot psi \\ 7.5\sqrt{\frac{f'_c}{psi}} psi \text{ if } Method = "ACI" \\ (2000psi) \text{ if } Method = "UHPCtest" \\ (750psi) \text{ if } Method = "UHPCproposal" \end{cases}$$

AASHTO 5.4.2.6

$\varepsilon_{cr} := \frac{f_r}{E_c} = 1.205 \times 10^{-4}$ Concrete strain at rupture

$$n := \frac{E_s}{E_c} = 5.946$$

$$c := \frac{(n-1)A'_s \cdot d' + (n-1)A_s \cdot d + A_g \cdot \frac{h}{2}}{A_g + (n-1)\cdot A'_s + (n-1)\cdot A_s} = 4.506 \cdot in$$ Centroid of section from top

Moment of inertia using transformed section

$$I_g := \left(\frac{b \cdot h^3}{12}\right) + A_g \cdot \left(\frac{h}{2} - c\right)^2 + (n-1)\cdot A'_s \cdot (d'-c)^2 + (n-1)\cdot A_s \cdot (d-c)^2 = 1.736 \times 10^3 \cdot in^4$$

$$M_{cr} := \frac{f_r \cdot I_g}{h - c} = 18.925 \cdot kip \cdot ft$$ Cracking strength using transformed section

$$\phi_{cr} := \frac{M_{cr}}{E_c \cdot I_g} = 2.682 \times 10^{-5} \cdot \frac{rad}{in}$$

Yield Strength

$\varepsilon_y := 0.00207$ Assume tensile steel yields and "compression" steel is in compression

$$f(c) := f_y \cdot A_s - \left(\frac{\varepsilon_y}{d-c}\right)\cdot(c-d')\cdot E_s \cdot A'_s - \left(\frac{1}{2}\right)\cdot\left(\frac{\varepsilon_y \cdot c}{d-c}\right)E_c \cdot c \cdot b$$ Force Equilibrium

$c := root(f(c), c) = 1.742 \cdot in$ Centroid of section at yielding

$$\varepsilon'_s := \begin{cases} \left[\left(\frac{\varepsilon_y}{d-c}\right)(d'-c)\right] & \text{if } c < d' \\ \left[\left(\frac{\varepsilon_y}{d-c}\right)\cdot(c-d')\right] & \text{if } c \geq d' \end{cases} = 5.414 \times 10^{-4}$$ "Compression" steel strain

$$M_y := f_y \cdot A_s \cdot \left(d - \frac{c}{3}\right) + \varepsilon'_s \cdot E_s \cdot A'_s \cdot \left(d' - \frac{c}{3}\right) = 39.36 \cdot kip \cdot ft$$ Yield strength using triangular stress block

$$\phi_y := \frac{\varepsilon_y}{d-c} = 4.529 \times 10^{-4} \cdot \frac{rad}{in}$$

Ultimate Strength

$\varepsilon_{cu} := 0.003$ $c_g := 2in$ Initial guess of c

$f_s := f_y$ $\varepsilon_{t.min} := 0.004$ bottom steel stress

$$\beta_1 := 0.85 - \frac{0.05 \cdot \left(\frac{f'_c}{psi} - 4000 \right)}{1000} = 0.75$$

Beta from ACI Table 22.2.2.4.3

Sum of forces

$$F(c_g) := \left(0.85 f'_c b \cdot \beta_1\right) \cdot c_g^{\,2} - \left(A_s \cdot f_y + 0.85 \cdot A'_s \cdot f'_c - A'_s \cdot E_s \cdot \varepsilon_{cu}\right) \cdot c_g - A'_s \cdot E_s \cdot \varepsilon_{cu} \cdot d'$$

$c := root(F(c_g), c_g) = 1.598 \cdot in$

$$\varepsilon_t := \left(\frac{\varepsilon_{cu}}{c}\right) \cdot (d - c) = 8.851 \times 10^{-3}$$

Centroid of section at ultimate moment, measured from the top surface

$\varepsilon_t \geq \varepsilon_{t.min} = 1$

$$\varepsilon'_s := \left(\frac{\varepsilon_{cu}}{c}\right) \cdot (c - d') = -2.515 \times 10^{-3}$$

Top steel strain

$$TopTensComp := \begin{cases} \text{"Top steel in compression"} & \text{if } \varepsilon'_s > 0 \\ \text{"Top steel in tension"} & \text{if } \varepsilon'_s < 0 \end{cases} = \text{"Top steel in tension"}$$

$$f'_s := \begin{cases} |E_s| \cdot |\varepsilon'_s| & \text{if } |E_s| \cdot |\varepsilon'_s| < 60ksi \\ 60ksi & \text{if } \left(|E_s| \cdot |\varepsilon'_s|\right) > 60ksi \end{cases} = 60 \cdot ksi$$

Top steel stress

$$\varepsilon_s := \left(\frac{\varepsilon_{cu}}{c}\right) \cdot (d - c) = 8.851 \times 10^{-3}$$

bottom steel strain

$\varepsilon_s \geq \varepsilon_y = 1$

$$\text{CompTransTens} := \begin{cases} \text{"Compression-controlled"} & \text{if } \varepsilon_t \le \varepsilon_y \\ \text{"Transition"} & \text{if } \varepsilon_y < \varepsilon_t < 0.005 \\ \text{"Tension-controlled"} & \text{if } \varepsilon_t \ge 0.005 \end{cases} = \text{"Tension-controlled"}$$

$$M_n := \left| f'_s \cdot A'_s \cdot \left(d' - \frac{\beta_1 \cdot c}{2} \right) + f_s \cdot A_s \cdot \left(d - \frac{\beta_1 \cdot c}{2} \right) \right| = 49.919 \cdot \text{kip} \cdot \text{ft}$$

Nominal strength using Whitney stress block

$$\phi_n := \frac{\varepsilon_{cu}}{c} = 1.877 \times 10^{-3} \cdot \frac{\text{rad}}{\text{in}}$$

Test Confiugration - 4 point bending (negative)

$w_{sw} := w_c \cdot b \cdot h = 0.262 \cdot \text{klf}$ Distributed load due to self weight of specimen

$x := 27\text{in}$ Distance between support and load

$L_{concrete} := 2 \cdot l + 6\text{in} = 102 \cdot \text{in}$ Total length of concrete panel, including UHPC joir

$L_{support} := 36\text{in}$ Distance between two supports

$M_{sw} := w_{sw} \cdot \frac{(x + 6\text{in})^2}{2} = 0.993 \cdot \text{ft} \cdot \text{kip}$ Maximum load due to self weight of specimen

$M_{test} := \left[48\text{plf} \cdot \left(\frac{9.625\text{ft}}{2} \right) + 150\text{lbf} + 35\text{lbf} \right] x = 0.936 \cdot \text{ft} \cdot \text{kip}$ Max moment due to test configuration

$M_{DC} := M_{sw} + M_{test} = 1.929 \cdot \text{ft} \cdot \text{kip}$ Maximum moment due to dead load

Actuator load to reach cracking, yield, and ultimate flexural capacity

$P_{cr} := \left(\frac{M_{cr} - M_{DC}}{x} \right) \cdot 2 = 1.511 \times 10^4 \cdot \text{lbf}$ Load to reach cracking strength

$P_{yield} := \left(\frac{M_y - M_{DC}}{x} \right) \cdot 2 = 3.327 \times 10^4 \cdot \text{lbf}$ Load to reach yield of tensile steel

$P_{u.F} := \left(\frac{M_n - M_{DC}}{x} \right) \cdot 2 = 4.266 \times 10^4 \cdot \text{lbf}$ Load to reach ultimate flexural capacity

Shear strength calculations (negatvie bending)

$V_c := 2\lambda \cdot \sqrt{\frac{f'_c}{psi}} \cdot psi \cdot b \cdot d = 2.738 \times 10^4 \cdot lbf$ Concrete shear strength

$V_{sw} := w_{sw} \cdot (x + 6in) = 721.875 \cdot lbf$ Maxmimum shear from self-weight

$V_{test} := 28plf \cdot \left(\frac{8ft}{2}\right) + 50lbf + 25lbf = 187 \cdot lbf$ Maximum shear from test configuration

$V_{DC} := V_{sw} + V_{test} = 908.875 \cdot lbf$ Maximum shear due to dead load

Actuator load to reach shear capacity

$P_{u.V} := \left(V_c - V_{DC}\right) \cdot 2 = 5.295 \times 10^4 \cdot lbf$ Load from actuator to cause shear failure

$$FailureMode := \begin{cases} \text{"Flexure"} & \text{if } \left(\frac{P_{u.V}}{P_{u.F}}\right) > 1 \\ \text{"Shear"} & \text{otherwise} \end{cases}$$

$\frac{P_{u.V}}{P_{u.F}} = 1.241$

FailureMode = "Flexure"

ACKNOWLEDGMENTS

The following individuals at GDOT provided many valuable suggestions throughout this study: Mr. Dexter Whaley, Bridge Design Group Leader; Mr. Jason Waters, Concrete Branch Chief; Mr. Chris Watson, Bridge Engineer; Mr. Peter Wu, Bureau Chief; Mr. Brennan Roney, Research Program Manager; and Ms. Supriya Kamatkar, Assistant Office Head, Office of Performance-based Management and Research. The opinions and conclusions expressed herein are those of the authors and do not represent the opinions, conclusions, policies, standards, or specifications of GDOT or of other cooperating organizations.

The authors would like to thank the Mr. Nan Gao for his assistance in the laboratory, and Mr. Jeremy Mitchell for his assistance in the laboratory experiment.

The authors express their profound gratitude to all these individuals for their assistance and support during the completion of this research project.

REFERENCES

1. Russell, H.G., and Graybeal, B.A., "Ultra-high performance concrete: A state-of-the-art report for the bridge community," United States. Federal Highway Administration. Office of Infrastructure , 2013.

2. Carey, A. S., I. L. Howard, D. A. Scott, R. D. Moser, J. Shannon and A. Knizley (2020). "Impact of Materials, Proportioning, and Curing on Ultra- High-Performance Concrete Properties." ACI Materials Journal 117(1): 213-222.

3. Graybeal, B. A., "Characterization of the ultra-high performance concrete," Doctor of Philosophy Dissertation, University of Maryland, College Park, 2005.

4. Panesar, D.K., "3 - Supplementary cementing materials," in Developments in the Formulation and Reinforcement of Concrete (Second Edition), S. Mindess Ed.: Woodhead Publishing, 2019, pp. 55-85.

5. Graybeal, B. A., "Material property characterization of ultra-high performance concrete," United States. Federal Highway Administration. Office of Infrastructure …, 2006.

6. F. de Larrard, T. Sedran, Optimization of Ultra-High-Performance Concrete by the Use of a Packing Model, Cement and Concrete Research, 24 (1994) 997-1009.

7. S. Rahman, T. Molyneaux, I. Patnaikuni, Ultra-high performance concrete: recent applications and research, Australian Journal of Civil Engineering, 2 (2005) 13-20.

8. F. De Larrard, Concrete mixture proportioning: a scientific approach, CRC Press 2014.

9. J. Van Der Putten, J. Dils, P. Minne, V. Boel, G. De Schutter, Determination of packing profiles for the verification of the compressible packing model in case of UHPC pastes, Materials and Structures, 50 (2017) 118.

10. L.A. Sbia, A. Peyvandi, P. Soroushian, A.M. Balachandra, K. Sobolev, Evaluation of modified-graphite nanomaterials in concrete nanocomposite based on packing density principles, Construction and building materials, 76 (2015) 413-422.

11. Lecomte, The measurement of real and virtual packing density of soft grains, Materials and structures, 39 (2006) 63-80.

12. F. De Larrard, T. Sedran, Mixture-proportioning of high-performance concrete, Cement and concrete research, 32 (2002) 1699-1704.

13. Andreasen, Über die Beziehung zwischen Kornabstufung und Zwischenraum in Produkten aus losen Körnern (mit einigen Experimenten), Kolloid-Zeitschrift, 50 (1930) 217-228.

14. J.E. Funk, D.R. Dinger, Predictive process control of crowded particulate suspensions: applied to ceramic manufacturing, Springer Science & Business Media. 2013.

15. H. Brouwers, Particle-size distribution and packing fraction of geometric random packings, Physical review E, 74 (2006).

16. M. Hunger, An integral design concept for ecological self-compacting concrete, (2010).

17. H. Brouwers, H. Radix, Self-compacting concrete: theoretical and experimental study, Cement and Concrete Research, 35 (2005) 2116-2136.

18. A. Alsalman, C.N. Dang, W.M. Hale, Development of ultra-high performance concrete with locally available materials, Construction and Building Materials, 133 (2017) 135-145.

19. Y.J. Kim, Development of Cost-Effective Ultra-High Performance Concrete (UHPC) for Colorado's Sustainable Infrastructure, 2018.

20. S. El-Tawil, M. Alkaysi, A.E. Naaman, W. Hansen, Z. Liu, Development, Characterization and Applications of a Non Proprietary Ultra-High Performance Concrete for Highway Bridges, Michigan. Dept. of Transportation, 2016.

21. M. Berry, R. Snidarich, C. Wood, Development of Non-Proprietary Ultra-High Performance Concrete, Montana. Dept. of Transportation. Research Programs, 2017.

22. P. Rangaraju, H. Kizhakommudom, Z. Li, S. Schiff, Development of High-Strength/High Performance Concrete/Grout Mixtures for Application in Shear Keys in Precast Bridges, Report FHWA-SC-13-04a. FHWA, US Department of Transportation, 2013.

23. B. Graybeal, Development of non-proprietary ultra-high performance concrete for use in the highway bridge sector, Publication No. FHWA-HRT-13-100 US Department of Transportation, Federal Highway Administration, (2013).

24. Kusumawardaningsih, Y., Fehling, E., and Ismail, M., "UHPC compressive strength test specimens: Cylinder or cube?," Procedia Engineering, vol. 125, pp. 1076-1080, 2015.

25. Graybeal, B. A., "Compressive behavior of ultra-high-performance fiber-reinforced concrete," ACI materials journal, vol. 104, no. 2, pp. 146-152, 2007.

26. Scott, D.A., Long, W. R., Moser, R. D., Green, B. H., O'Daniel, J. L., and Williams, B. A., "Impact of steel fiber size and shape on the mechanical properties of ultra-high performance concrete," ENGINEER RESEARCH AND DEVELOPMENT CENTER, 2015.

27. Kim, H., Hadl, P., and Nguyen, V. T., "A New Mix Design Method for UHPC based on Stepwise Optimization of Particle Packing Density," in International Interactive Symposium on Ultra-High Performance Concrete, 2016, vol. 1, no. 1: Iowa State University Digital Press.

28. Ahlborn, T. M., Peuse, E. J., and Misson, D. L., "Ultra-high performance concrete for Michigan bridges, material performance: phase I," Michigan. Dept. of Transportation, 2008.

29. Berry, M., Snidarich, R., and Wood, C., "Development of non-proprietary ultra-high performance concrete," Montana. Dept. of Transportation. Research Programs, 2017.

30. Ahmad, S, Hakeem, I., and Maslehuddin, M., "Development of an optimum mixture of ultra-high performance concrete," *European Journal of Environmental and Civil Engineering,* vol. 20, no. 9, pp. 1106-1126, 2016.

31. Khaloo A., Karimi H., Asadollahi S., and Dehestani M., "A new mixture design method for ultra-high-strength concrete," *ACI Materials Journal,* vol. 114, no. 2, pp. 215-224, 2017.

32. B. Reichard, B., Stewart, L., Weaver, M., and Morrill, K., "Coupled Hydraulic System for Tensile Testing in Compression-only Machines," *Experimental Mechanics,* vol. 56, no. 7, pp. 1179-1190, 2016.

33. *Standard Test Method for Flexural Performance of Fiber-Reinforced Concrete (Using Beam With Third-Point Loading),* A. International, West Conshohocken, PA, 2019.

34. Graybeal, B. A. and Baby F., "Tension testing of ultra-high performance concrete," Federal Highway Administration, 2019.

35. Roth, M. J., Rushing, T. S., Flores, O. G., Sham, D. K., and Stevens, J. W., "Laboratory investigation of the characterization of Cor-Tuf flexural and splitting tensile properties," 2010.

36. Kizhakommudom, H., Li, Z., and Schiff, S. D., "Research Project No. 682 Development of High-Strength/High Performance Concrete/Grout Mixtures for," 2014.

37. Graybeal, B.A., "Field-cast UHPC connections for modular bridge deck elements," Federal Highway Administration, 2010.

38. Graybeal, B.A., "Design and construction of field-cast UHPC connections," United States. Federal Highway Administration, 2014.

39. Graybeal, B.A., "Behavior of Ultra-High Performance Concrete Connections between Precast Bridge Deck Elements," 2010.

40. Haber, Z. B. and Graybeal, B. A., "Performance of grouted connections for prefabricated bridge deck elements," United States. Federal Highway Administration. Office of Infrastructure …, 2018.

41. G.D.o. Transportation, Project ID: 0007159, in: D.o.E.-O.o.B.a. Structures (Ed.)GDOT Project Search, 2014, pp. 44.

42. P.C. Association, Georgia Cement Industry, Cement Industry by StateWeb, 2016.

43. S.A. Khedr, M.N. Abou-Zeid, Characteristics of silica-fume concrete, Journal of Materials in Civil Engineering, 6 (1994) 357-375.

44. T. Teichmann, M. Schmidt, Influence of the packing density of fine particles on structure, strength and durability of UHPC, International symposium on ultra-high performance concrete, 2004, pp. 313-323.

45. P. Rougeau, B. Borys, Ultra-high performance concrete with ultra-fine particles other than silica fume, Proceedings of the International Symposium on Ultra-High Performance Concrete, 2004, pp. 213-225.

46. J.E. Brantly, A report on the limestones and marls of the Coastal Plain of Georgia, Blosser1916.

47. R. Asmatulu, Removal of the discoloring contaminants of an East Georgia kaolin clay and its dewatering, Turkish Journal of Engineering and Environmental Sciences, 26 (2002) 447-453.

48. A. Tafraoui, G. Escadeillas, S. Lebaili, T. Vidal, Metakaolin in the formulation of UHPC, Construction and Building Materials, 23 (2009) 669-674.

49. Z. Rong, G. Jiang, W. Sun, Effects of metakaolin on mechanical and microstructural properties of ultra-high performance cement-based composites, Journal of Sustainable Cement-Based Materials, 7 (2018) 296-310.

50. E.M. Williams, S.S. Graham, P.A. Reed, T.S. Rushing, Laboratory characterization of Cor-Tuf concrete with and without steel fibers, ENGINEER RESEARCH AND DEVELOPMENT CENTER VICKSBURG MS GEOTECHNICAL AND …, 2009.

51. C.D. Atiş, O. Karahan, Properties of steel fiber reinforced fly ash concrete, Construction and Building Materials, 23 (2009) 392-399.

52. E. Materials, Elkem Materials Mixture Analyser (EMMA) User Guide, 1 1-33.

53. K. Wille, B. Graybeal, Development of Non-Proprietary Ultra-High Performance Concrete for Use in the Highway Bridge Sector, Federal Highway Administration, FHWA, 2013.

54. P. Domone, J. Jin, Properties of mortar for self-compacting concrete, PRO 7: 1st International RILEM Symposium on Self-Compacting Concrete, RILEM Publications, 1999, pp. 107.

55. N.V. Tue, J. Ma, M. Orgass, Influence of addition method of superplasticizer on the properties of fresh UHPC, Proceedings of the 2nd International Symposium on Ultra-High Performance Concrete, Kassel, Germany, 2008, pp. 93-100.

56. C.-S. Poon, L. Lam, S. Kou, Y.-L. Wong, R. Wong, Rate of pozzolanic reaction of metakaolin in high-performance cement pastes, Cement and concrete research, 31 (2001) 1301-1306.

57. D. Lowke, P. Schiessl, Effect of mixing energy on fresh properties of SCC, Proceedings of the 4th international RILEM symposium on self-compacting concrete, Chicago, USA, 2005.

58. H. Brouwers, Particle-size distribution and packing fraction of geometric random packings, Physical review E, 74 (2006).

59. M. Hunger, An integral design concept for ecological self-compacting concrete, (2010).

60. D. Lowke, P. Schiessl, Effect of mixing energy on fresh properties of SCC, Proceedings of the 4th international RILEM symposium on self-compacting concrete, Chicago, USA, 2005.

61. J. Dils, G. De Schutter, V. Boel, Influence of mixing procedure and mixer type on fresh and hardened properties of concrete: a review, Materials and structures, 45 (2012) 1673-1683.

62. I. Schachinger, J. Schubert, O. Mazanec, Effect of mixing and placement methods on fresh and hardened ultra-high performance concrete (UHPC), International Symposium on Ultra-High Performance Concrete, 2004, pp. 575-586.

63. G. Yanni, V. Youssef, Multi-scale investigation of tensile creep of ultra-high performance concrete for bridge applications, Georgia Institute of Technology, 2009.

64. M.J. Roth, T.S. Rushing, O.G. Flores, D.K. Sham, J.W. Stevens, Laboratory investigation of the characterization of Cor-Tuf flexural and splitting tensile properties, ENGINEER RESEARCH AND DEVELOPMENT CENTER VICKSBURG MS GEOTECHNICAL AND …, 2010.

65. I. Schachinger, J. Schubert, O. Mazanec, Effect of mixing and placement methods on fresh and hardened ultra-high performance concrete (UHPC), International Symposium on Ultra-High Performance Concrete, 2004, pp. 575-586.

66. E. Camacho, J.Á. López, P.S. Ros, Definition of three levels of performance for UHPFRC-VHPFRC with available materials, Ultra-High Performance Concrete and Nanotechnology in Construction. Proceedings of Hipermat 2012. 3rd International Symposium on UHPC and Nanotechnology for High Performance Construction Materials, kassel university press GmbH, 2012, pp. 249

67. J. Justs, M. Wyrzykowski, D. Bajare, P. Lura, Internal curing by superabsorbent polymers in ultra-high performance concrete, Cement and Concrete Research, 76 (2015) 82-90.

68. A.D.d. Figueiredo, M.R. Ceccato, Workability analysis of steel fiber reinforced concrete using slump and Ve-Be test, Materials Research, 18 (2015) 1284-1290.

69. S.W. Kim, S.T. Kang, J.J. Park, G.S. Ryu, Effect of filling method on fibre orientation and dispersion and mechanical properties of UHPC, Proceedings of the 2nd International Symposium on Ultra-High Performance Concrete, Kassel, Germany, 2008, pp. 185-192.

70. R. Wang, X. Gao, H. Huang, G. Han, Influence of rheological properties of cement mortar on steel fiber distribution in UHPC, Construction and Building Materials, 144 (2017) 65-73.

71. Bekaert, Dramix OL Data Sheet, Web, 2019.

72. V. Garas, K. Kurtis, L. Kahn, Creep of UHPC in tension and compression: effect of thermal treatment, Cement and Concrete Composites, 34 (2012) 493-502.

73. P. Acker, M. Behloul, Ductal® technology: A large spectrum of properties, a wide range of applications, Proc. of the Int. Symp. on UHPC Kassel, Germany, 2004, pp. 11- 23.

74. D.A. Scott, W.R. Long, R.D. Moser, B.H. Green, J.L. O'Daniel, B.A. Williams, Impact of steel fiber size and shape on the mechanical properties of ultra-high performance concrete, ENGINEER RESEARCH AND DEVELOPMENT CENTER VICKSBURG MS GEOTECHNICAL AND …, 2015.

75. C. Perlot, P. Rougeau, S. Dehaudt, Slurry of metakaolin combined with limestone addition for self-compacted concrete. Application for precast industry, Cement and concrete composites, 44 (2013) 50-57.

76. *EIRICH Intensive Mixer*, 2018, pp. 1-16.

77. Schachinger, I., Schubert, J., and Mazanec, O., "Effect of mixing and placement methods on fresh and hardened ultra-high performance concrete (UHPC)," in *International Symposium on Ultra-High Performance Concrete*, 2004, pp. 575-586.

78. *Testing Hardened Concrete - Part 3: Compressive Strength of Test Specimens*, EN-12390-3, E. Standard, 2019.

79. Graybeal, B. A. (2013). Development of Non-Proprietary Ultra-High Performance Concrete for Use in the Highway Bridge Sector: TechBrief, United States. Federal Highway Administration.

80. Rougeau, P., and Borys, B., "Ultra-high performance concrete with ultra-fine particles other than silica fume," in *Proceedings of the International Symposium on Ultra-High Performance Concrete*, 2004, vol. 32, pp. 213-225.